Nanomechanics of Cartilage Extracellular Matrix Macromolecules

by

Lin Han

Submitted to the Department of Materials Science and Engineering
in partial fulfillment of the requirements for the degree of

Doctor of Philosophy

at the

MASSACHUSETTS INSTITUTE OF TECHNOLOGY

September 2007

Author .....
Department of Materials Science and Engineering
August 28th, 2007

Certified by .....
Alan J. Grodzinsky
Professor of Electrical, Mechanical and Biological Engineering
Thesis Supervisor

Certified by .....
Christine Ortiz
Associate Professor of Materials Science and Engineering
Thesis Supervisor

Accepted by .....
Samuel M. Allen, POSCO Professor of Physical Metallurgy
Chair, Departmental Committee on Graduate Students

Nanomechanics of Cartilage Extracellular Matrix Macromolecules

by

Lin Han

Submitted to the Department of Materials Science and Engineering
on August 28th, 2007, in partial fulfillment of the
requirements for the degree of
Doctor of Philosophy

Abstract

In this thesis, the shear and self-adhesion nanomechanical properties between opposing cartilage aggrecan macromolecules were probed. In addition, nanoscale dynamic oscillatory mechanical properties of cartilage and its type II collagen network was measured.

Aggrecan shear nanomechanics was assessed via microcontact printing and lateral force microscopy. Lateral force between aggrecan and the probe tip, and compression of aggrecan was simultaneously measured in $0.001 - 1.0$ M NaCl aqueous solutions. Using the microsized tip ($R_{tip} \sim 2.5$ μm) enabled a large assembly of $\sim 10^3$ aggrecan molecules to interact simultaneously, closely mimicking the *in vivo* conditions. Both electrostatic and nonelectrostatic components were identified to importantly contribute to aggrecan shear. At near physiological IS (0.1 M), significant rate dependence was observed, suggestive of visco/poroelastic interactions within the aggrecan layer.

By using an aggrecan end-functionalized colloidal tip, shear of two opposing aggrecan layers was assessed in a similar fashion. Lower lateral force and a more marked rate dependence were measured compared to the shear of a single layer, due to the aggrecan inter-layer molecular interpenetration and the different local z-dependent charge density distribution. The addition of Ca^{2+}, at physiological-like 2 mM concentration, significantly affects cartilage shear by its electrostatic screening and binding effects.

Marked aggrecan self-adhesion upon separation was discovered after static compression in the presence of electrostatic repulsion in physiological-like conditions. Aggrecan self-adhesion increases as increasing equilibration time and bath IS. Molecular origins of the adhesion, also present *in vivo*, include van der Waals, hydrogen bonding, Ca^{2+}-mediated bridging, and molecular entanglements between the glycosaminoglycan branches of aggrecan. This self-adhesion could be an important factor in protecting cartilage matrix structural integrity and function via these energy-dissipative mechanisms.

The nanoscale oscillatory dynamic deformation properties of both nontreated and

proteoglycan(PG)-depleted (left mostly type II collagen) calf knee cartilage disks ($\sim$ 0.5 mm thick) was measured by connecting an external electronic wave generator to the AFM. A significant increase in effective stiffness E and phase lag Δ (deformation with respect to force) as increasing frequency for both disks suggests poro/viscoelasticity are more critical at higher frequency. The PG-depleted disk shows a more marked dependence of E and Δ on deformation amplitude $\sim 2 - 100$ nm, as the nanostructure and nanomechanical properties of porous collagen network are more heterogeneous without the entrapment of aggrecan motif. A unique $\sim$ 23 nm banding pattern along the type II collagen fibrils was observed, which may be relative to the cartilage swelling properties and the molecular interaction between aggrecan and the collagen network.

Taken together, this study provides insights into molecular-level deformation of cartilage extracellular matrix (ECM) macromolecules (e.g., aggrecan, type II collagen) that are important to the understanding of cartilage biomechanical function. Ongoing studies are probing the age, disease (osteoarthritis), source and species related variations of cartilage ECM properties at the molecular level.

Thesis Supervisor: Alan J. Grodzinsky
Title: Professor of Electrical, Mechanical and Biological Engineering

Thesis Supervisor: Christine Ortiz
Title: Associate Professor of Materials Science and Engineering

Acknowledgments

Time flies! Cannot believe my Ph.D. life is ending so quick! Here I would like to thank a lot of people who helped me through the 5 years at MIT.

Firstly, I would like to thank my thesis advisors, Professor Alan J. Grodzinsky and Professor Christine Ortiz. They guided me through the fun world of "cartilage nanomechanics", an interdisciplinary topic that requires a good grasp on a variety of fields. Christine is a great advisor and always gets me motivated and encouraged, and provides me smart and tricky ways to solve hard problems. I can not believe how AFM can be one of my best friends without her instructions. I feel so honored and appreciated to become one of Al's graduate students. His sparkling ideas have lead me to the accomplishment of all these interesting research projects and he is always being considerate and supportive. He taught me there is actually no difference between a Ph.D. and a Sc.D.:) I would also like to thank Professor Paula Hammond and Professor Michael Rubner to agree being in my thesis committee and give me a lot of precious suggestions without giving me a hard time.:)

It was a great experience being in the nanocartilage group! Professor Delphine Dean figured out how to end-attach aggrecan on a planar substrate and that was when my Ph.D. projects really started progressing. We have been sitting in the nanosized AFM room scanning and poking aggrecan for a long long time. Laurel Ng was such a great artist to be the first person on the planet who can see the fine fine structure of aggrecan with a tiny AFM tip. And how I miss the yummy cakes Delphine and Laurel made! Laurel's husband, Alex, motivated me to use LaTex to write my thesis, and it turned out I love this idea. Bo Bae has become the master of chondrocytes by poking them for a million times. Hsu-Yi is continuing the honor of our group and becoming on top of both imaging and force measurement! I also enjoyed a lot working with my UROPs, Laura, Jacqueline and Ryan. I wish our "nanosized" group members will have fun in the future too.

I got lots of help from labmates in both Al and Christine's groups. Han-Hwa is our "Chinese Mother" of the whole lab. She trained me the DMMB dye assay and helped me to cut the bloody mouse joints! She also gave me a lot of homemade delicious food whenever I am hungry. I remember I got to know Shuodan in Al's FFF class and we always worked together up to 3am to finish the homework. Finally, we ended up in the same lab and enjoyed the same cartilage.:) And thank Shuodan, Yi, Diana, Cameron and Sangwon for the cow joints so I do not have to cut the beef by myself! Monica is my first trainer in Ortiz lab and she made me have a good hand on both the AFM and MFP. Kuangshin is a very good friend to share every piece of experience in our lab. Ben let me use his name to get the access to the ISN AFM, and discussion with Miao has always been fun and helpful to my research. Linda, Tim and Jeremy have helped me with lots of important works that always confused me. Taken together, I would like to thank everyone in Ortiz and Grodzinsky lab, they have given me a great experience here. Sorry if I missed anyone! I would also like to thank MIT Institute for Soldier Nanotechnologies (ISN), since I have been using their AFM machine for many years without paying a penny.

My sweet friends have been the ultimate support for me these years. Andy is my best buddy, offering me ride everytime, bringing me to all the delicious restaurants and always being there for me. He has persuaded me to take part in the half-marathon race together with him, Miao and Song, what an achievement I will be proud of for my whole life! Song is the only female member of our 3 year jogging team, and gave our trails a lot of fun, and she is going to be Professor Gao next month so good luck to her! Peng is one of the nicest and most beautiful girl I have ever met, and I am glad for her that she is going to get married soon. Hanging out with Xuemin and Dulles has relieved me from the stress a lot. Xiaodong and Feiya are the sweet couple, we shared our life together at MIT for 5 year together, since we got on the same plane in Beijing on August 26th, 2002. Rong was my free gym training two years ago and he dragged me into the whole working-out thingy! Now working out with Fei, Huan and Bo is an important part of my life, I cannot carry on my working out plans without his accompany. Qinyan is my best friend, and having lunch with him together in the last year of my Ph.D. career gave me a lot of good memories. Yu always hosted me when I went to New York, so I never paid the hotel there. It is very nice to live with him in New York after I move there. I also shared a lot of sweet and fun memories with Wenjiang, Xiaofeng, Gao and Haitao in Boston.

I still remember the day MIT Chinese Students and Scholars Association (CSSA) picked me upon my first arrival at US so I did not get lost. Later, I got to know a lot of friends in CSSA. Working in the Career and Academic Developement (CAD) Department with Andy made me start thinking about my career, and this experience is very beneficial to me. As the Vice President of CSSA from 2005 to 2006, I had a great experience working with Huan, which I could not have learnt from the textbooks; and, had a lot of fun so my life is never boring.

Finally, I would like to thank my family, my grandparents, parents, aunts and my cousins, backing me up unconditionally.

Contents

List of Figures

List of Tables

Chapter 1

Introduction

1.1 Background

Cartilage is the avascular tissue that lines the long ends of bones and sustains a complex combination of compressive, shear, and tensile loads during joint motion. Cartilage is composed of water (w/w $\sim 60 - 80\%$), proteoglycan (PG) aggregates ($\sim 10\%$), collagen fibrils ($\sim 15 - 20\%$), and chondrocyte cells ($\sim 3 - 5\%$) [99]. Both the proteoglycan motif and the type II collagen network in the cartilage extracellular matrix (ECM) are known to directly contribute to cartilage biomechanical properties. The field of nanomechanics (the study of nanoscale forces and displacements), in particular applied to cartilage, has shown great potential to yield new scientific information such as the molecular origins of biomechanical properties, it is hence possible to probe nanomechanics of the cartilage ECM contents and provide molecular-level insights into cartilage tissue mechanics and functions via atomic force microscopy and its related techniques.

1.2 Objectives

The motivation of this research is to determine the molecular contributions of both the aggrecan motif and the type II collagen network to cartilage tissue mechanical properties. Aggrecan, the most abundant proteoglycan in cartilage tissue, has a

"bottle-brush" structure, with highly negatively charged glycosaminoglycan (GAG) chains densely packed along its core protein. Aggrecan is known to play a critical role in cartilage compressive [75] and shear [83] tissue mechanical properties. The solid type II collagen network functions as a scaffold of the cartilage tissue, and sustains a complex of tensile, compressive and shear stress during joint motion as well.

Continuing the Ph.D. thesis work on aggrecan compressive nanomechanics by Delphine Dean [27, 28], the first goal of this thesis is to understand the shear and self-adhesive interactions between aggrecan macromolecules. Secondly, this thesis probes the nanostructure and dynamic deformation of intact cartilage and its solid type II collagen network at nano- and microscale. In combination with the previous studies on aggrecan compressive nanomechanics, this research provides a basic understanding of the molecular-level deformation mechanisms of cartilage ECM constituents, aggrecan and type II collagen, as well as its contribution to the macroscopic cartilage structure and functions.

The development of modern atomic force microscopy techniques enables not only imaging biomacromolecules at nanometer scale, also the quantification of nano-newton scale forces associated with these macromolecules in different directions and time-scales in ambient conditions. Hence, in order to provide a comprehensive understanding of biomechanics of these macromolecules, a variety of AFM-related techniques were applied to achieve these goals, such as contact and tapping mode AFM imaging, lateral force microscopy, high-resolution force spectroscopy, etc. The measured results were analyzed with related scientific theories, e.g. Poisson-Boltzmann electrostatic model, visco/poroelasticity, polymer molecular mechanics, etc., to understand the associated molecular mechanisms to elucidate the molecular origins and their contributions to cartilage tissue-level mechanics.

1.3 Overview

This thesis is structured as follows. Chapter 2 provides a brief overview of cartilage extracellular matrix constituents and cartilage aggrecan compressive nanomechanics.

Chapter 3 describes the lateral(shear) nanomechanics of a single end-attached aggrecan layer via lateral force microscopy, the calibration details of LFM for the specific spherical colloidal probe tips used in this study was described in Appendix B. This chapter was published as a regular article in Biophysical Journal in 2007 [62]. Chapter 4 extends this study to the nanoscale shear of two opposing aggrecan layers, using an aggrecan end-functionalized colloidal tip, which was published in Biophysical Journal as a biophysical letter in 2007 [63]. Chapter 5 discusses the self-adhesive interactions between opposing aggrecan layers. Chapter 6 describes the nanostructure of the type II collagen fibrils, and dynamic nanoscale deformation of cartilage and its type II collagen network.

Chapter 2

Background

Articular cartilage is the loading bearing tissue at the surfaces of bones in synovial joints. It is subjected to a combination of tensile, compressive and shear loads between joints during motion. Its extracellular components, e.g. aggrecan, type II collagen, etc., are the direct determinants of cartilage tissue mechanical properties and functions.

2.1 Cartilage extracellular matrix (ECM)

Cartilage is a specialized avascular tissue composed of a relatively small number of chondrocyte cells, surrounded by its complex extracellular matrix. Approximately $60 - 80\%$ weight of the whole tissue is composed of water. The remainder of the ECM is mainly consisted of the proteoglycan motif and fibril-forming type II collagen, Figure 2-1a. The term "proteoglycan" refers to the macromolecules of connective tissue constructed of a protein backbone and a large number of covalently bounded glycosaminoglycan side chains, Figure 2-1b [109]. In cartilage, the family of proteoglycan includes a variety of biomacromolecules, e.g. the large aggregating proteoglycan (aggrecan), leucine-rich proteoglycans (decorin, biglycan and fibromodulin), type IX collagen etc. Their functions vary from the mechanical support (aggrecan), to cell-binding receptors (CD44), to matrix-binding and cell-surface receptors (heparan sulfate proteoglycans) etc. [65]. The most abundant proteoglycan, aggrecan, con-

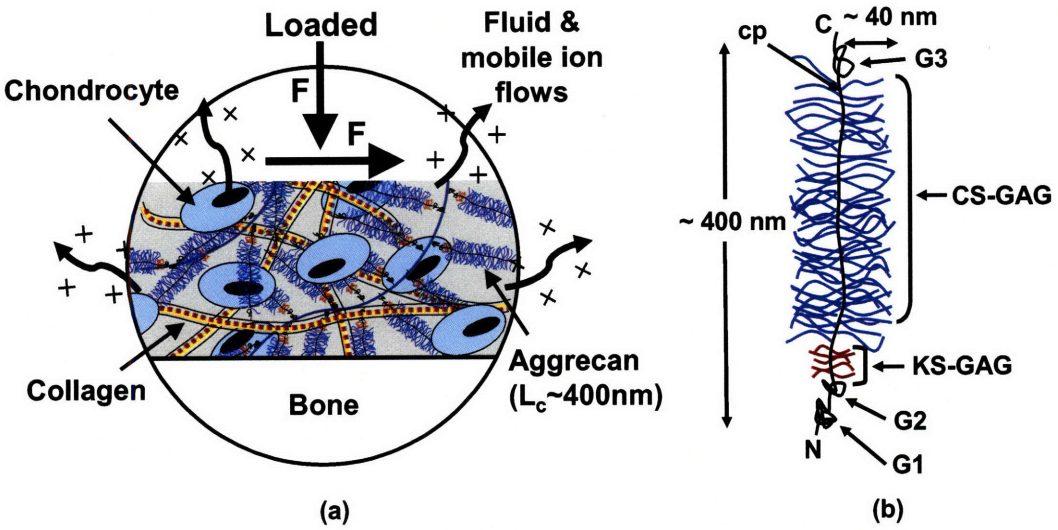

Figure 2-1: (a) Illustration of major cartilage extracellular matrix (ECM) components: collagen, aggrecan and hyaluronan etc. with chondrocyte cells upon mechanical loading induced deformation. (b) Schematic representation of the structure of aggrecan (contour length $\sim$ 400 nm), illustrating the core protein backbone (cp) and its three globular domains (G1, G2, G3), and the grafted chondroitin sulfate (CS) and keratan sulfate (KS) glycosaminoglycan (GAG) side chains. CS-GAG contour length $\sim$ 40 nm, intermolecular spacing $\sim 2-4$ nm; N = N-terminal; C = C-terminal).

tributes significantly to the compressive [75] and shear [83] stiffness of cartilage, as well as the osmotic swelling pressure of the tissue [99, 4]. The fibrous type II collagen network functions as the scaffold of the cartilage tissue, and contributes to cartilage tissue tensile and shear strength [99].

2.2 Aggrecan

Aggrecan, the largest and most abundant proteoglycan in cartilage, comprises $30-35\%$ of cartilage tissue dry weight ($5-10\%$ of wet weight). It is composed of a core protein (MW: $225-250$ kDa [65], contour length $\sim$ 400 nm), and densely packed long glycosaminoglycan (GAG) side chains, Figure 2-1b. *In vivo*, aggrecan is attached to the hyaluronan biomacromolecule via its G1 globular domain near the N-terminal of its core protein, strengthened by the presence of link proteins,

which forms large aggregates of aggrecan. [66, 74] Between the G2 and G3 domains, there are highly negatively charged, densely packed GAG chains, mainly in three different forms: chondroitin-4-sulfate glycosaminoglycan (C4S-GAG), chondroitin-6-sulfate glycosaminoglycan (C6S-GAG) and keratan-sulfate glycosaminoglycan (KS-GAG).

There are ~ 100 CS-GAG chains ($25-30$ dissacharide units, contour length ~ 40 nm) covalently bounded along each aggrecan core protein via Ser-Gly residues [65, 75], spacing $2-4$ nm apart. CS-GAG chains are composed of alternating glucuronic and N-actetyl-6 (or 4)-sulfate galactosamine (Figure 2). The ratio of C6S-GAG and C4S-GAG varies from < 1 in the fetal and newborn infant to > 20 in the adult tissue [122]. The sulfate and carboxyl functional groups in the structural units of CS-GAGs are negatively charged in physiological conditions, and the electrostatic repulsion between them accounts for $\sim 50\%$ of tissue's equilibrium compressive moduli and swelling pressures [14, 37, 98, 114]. The smaller KS-GAG chains are consisting of ~ 10 repeating dissacharide units and play a less important role for directly determining cartilage mechanical properties. Upon the events like osteoarthritis and acute joint injury, aggrecan is the first component that experiences significant loss, which leads to the irreversible deterioration of cartilage biomechanical functions. Also, studies have shown that aggrecan functions degrade with age, as the length of CS and KS chains become shorter with age [146, 110].

In this thesis, we use aggrecan molecules extracted from fetal epiphyseal bovine cartilage. As Ng et al. [110] has reported, the fetal epiphyseal aggrecan has a core protein with contour length 398 ± 57 nm, persistence length ~ 110 nm, with CS-GAG chains (~ 50 dissacharides, contour length 42 ± 7 nm, persistence length ~ 21 nm) packing at 3.2 ± 0.8 nm apart. The nanostructures and compressive nanomechanics of this aggrecan has been explicitly studied by Ng et al. [110] and Dean et al. [27, 28], respectively.

2.3 Type II collagen

Articular cartilage by dry weight is $\sim$ 60% of collagen ($\sim$ 15 – 20% wet weight), which is composed of 75 – 90% of type II collagen fibrils, and other components include type III, VI, IX, X, XI, XII/XIV, XIII etc. The richest type II collagen, a triple helix formed by three α1(II) polypeptide chains, forms the fibrils with collagen IX covalently linked to the surface and collagen XI forms the filamentous template of the fibril as a whole [42]. These type II collagen fibrils (diameter $\sim$ 30 – 80 nm) construct a relatively coarse and electrically neutral framework (gaps between the fibrils $>$ 100 nm) compared to the 2 – 10 nm "pores" within the proteoglycan-water gel [99]. The collagen matrix is essential for the integrity of the whole cartilage tissue, and important for its tensile as well as compressive tissue mechanical properties. As the turnover of the collagen framework is slow, any severe damage appears to be irreversible and a critical step in the process of joint failure [42]. In this study, we probed the nanoscale deformation of the whole cartilage tissue, as well as this collagen network in physiological-like aqueous conditions using calf knee cartilage. Nanostructure of the type II collagen fibrils was also studied in air-dried state.

2.4 Compressive nanomechanics of cartilage aggrecan macromolecules

Previously, Dean et al. have measured the nanoscale compressive interactions between opposing aggrecan macromolecules in near physiological conditions, in order to elucidate the molecular origins of tissue-level cartilage biomechanical behavior. Details of this study were published as an original article in Journal of Biomechanics in 2006 [28]. Aggrecan molecules from fetal bovine epiphyseal cartilage were chemically functionalized with thiol-groups and end-grafted to gold-coated planar substrates, standard nanosized atomic force microscopy (AFM) probe tips ($R_{tip} \sim$ 50 nm), and larger colloidal probe tips ($R_{tip} \sim$ 2.5 μm) via thiol-gold bonds. To assess normal nanomechanical interaction forces between opposing aggrecan layers, substrates with

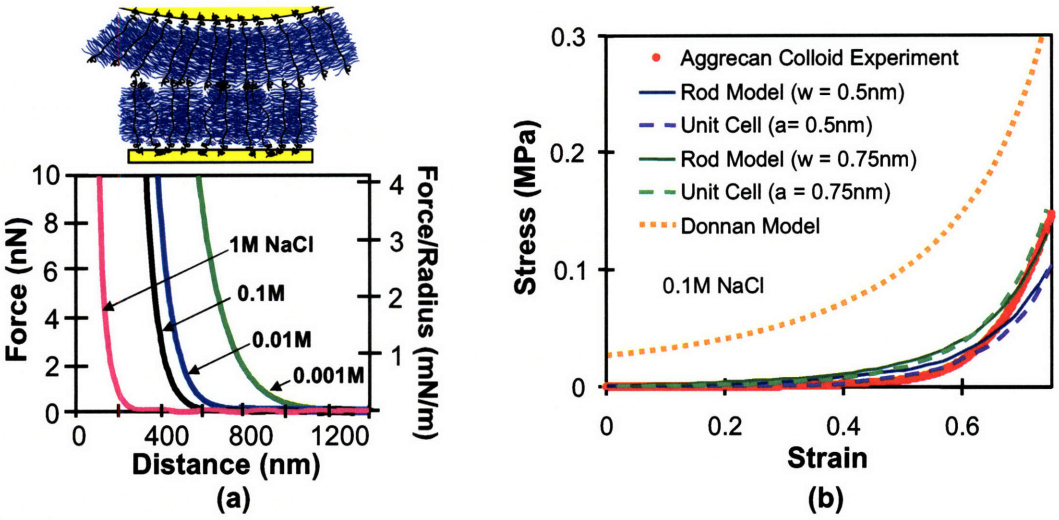

Figure 2-2: (a) Average force between two opposing aggrecan layers using an aggrecan functionalized colloidal probe tip ($R_{tip} \sim 2.5$ μm, $k \sim 0.12$ N/m) versus the aggrecan functionalized planar substrate at different bath ionic strengths ($0.001 - 1.0$ M NaCl, pH ~ 5.6). (b) Aggrecan nanomechanical data at 0.1 M NaCl (near physiological ionic strength) converted to stress-strain (red dots) compared to the Poisson-Boltzmann-based electrostatic models: the rod model (lines), the unit cell model (dashed lines), and the volume charge model (orange dotted line). Adapted from Dean et al. [28].

microcontact printed aggrecan and a neutral hydroxyl self-assembled monolayer (OH-SAM) were imaged using contact mode AFM, and aggrecan layer height (and hence deformation) was measured as a function of solution ionic strength (IS) and applied normal load. Then, using high-resolution force spectroscopy, nanoscale compressive forces between opposing aggrecan on the tip and substrate were measured versus tip-substrate separation distance in $0.001 - 1.0$ M NaCl, Figure 2-2a. Aggrecan height and repulsive force decrease with increasing bath ionic strength due to the screening of electrostatic repulsions. Nanosized tips enabled measurement of the molecular stiffness of $2 - 4$ aggrecan while colloidal tips probed the nanomechanical properties of larger assemblies ($\sim 10^4$ molecules). The compressive stiffness of aggrecan was much higher when using a densely packed colloidal tip than the stiffness measured for using the nanosized tip with a few aggrecan, demonstrating the importance of lateral interactions to the normal nanomechanical properties. The measured stress at 0.1M NaCl (near-physiological ionic strength) increased sharply at aggrecan densities under the tip of ~ 40 mg/mL (physiological densities are $\sim 20 - 80$ mg/mL), corresponding to an average inter-GAG spacing of $4 - 5\times$ Debye lengths ($4 - 5$ nm); this characteristic spacing is consistent with the onset of significant electrostatic interactions between GAG chains of opposing aggrecan molecules. Comparison of nanomechanical data to the predictions of Poisson-Boltzmann-based models further elucidated the regimes over which electrostatic and nonelectrostatic interactions affect aggrecan stiffness in compression, Figure 2-2b. The most important aspects of this study include: the incorporation of experiments at two different length scales, the use of microcontact printing to enable quantification of aggrecan deformation and the corresponding nanoscale compressive stress versus strain curve, the use of tips of differing functionality to provide insights into the molecular mechanisms of deformation, and the comparison of experimental data to the predictions of three increasingly refined Poisson-Boltzmann (P-B)-based theoretical models for the electrostatic double layer component of the interactions. Continuing this study, we probed shear and self-adhesive interactions between opposing fetal bovine epiphyseal aggrecan layers in Chapters $3 - 5$.

Chapter 3

Lateral Nanomechanics of Cartilage Aggrecan Macromolecules

This chapter was published as a regular article in Biophysical Journal in 2007. Further technical details and applications of the experimental system presented here are also provided in Appendix B.

3.1 Introduction

Articular cartilage is a specialized connective tissue found at the surfaces of bones in synovial joints. Cartilage macromolecular composition and structure [12] is optimized to sustain a complex combination of compressive, shear, and tensile loads that exist during joint motion [33, 31]. The major extracellular matrix (ECM) proteoglycan, *aggrecan*, which comprises $30-35\%$ of the tissue dry weight, is thought to play a critical role in proper biomechanical functioning of cartilage in response to compressive [75] and shear [83] loads. Aggrecan is a polyelectrolyte having a "bottle-brush" structure (Figure 3-1), consisting of a core protein (contour length ~ 400 nm) with ~ 100 covalently bound chondroitin sulfate glycosaminoglycan (CS-GAG) chains (contour length ~ 40 nm) that are closely spaced ($2-4$ nm) and negatively charged, along with

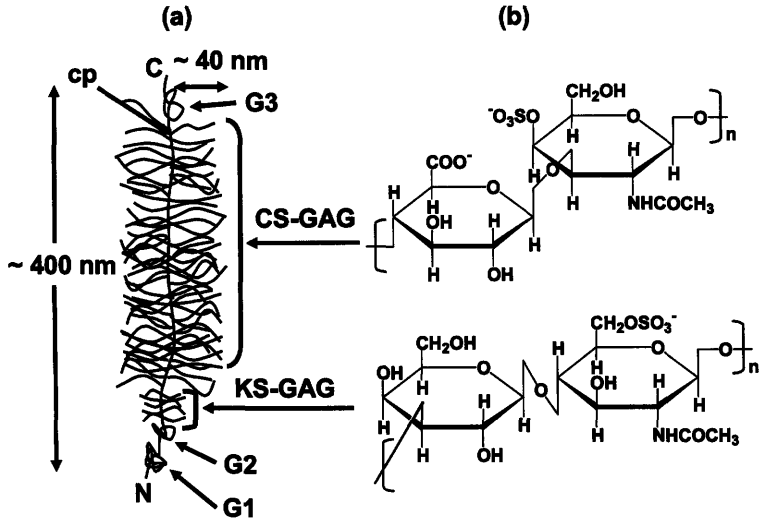

Figure 3-1: (a) Schematic representation of the structure of aggrecan (contour length $\sim$ 400 nm), illustrating the core protein backbone (cp) and its three globular domains (G1, G2, G3), and the grafted chondroitin sulfate (CS) and keratan sulfate (KS) glycosaminoglycan (GAG) side chains. CS-GAG contour length $\sim$ 40 nm, intermolecular spacing $\sim 2-4$ nm; N = N-terminal; C = C-terminal). (b) Disaccharide constituents of chondroitin-4-sulfate GAG and KS-GAG.

smaller keratan sulfate GAGs and oligosaccharides [65, 110]. Within cartilage tissue, aggrecan is bound non-covalently at its G1 globular domain to the higher molecular weight GAG chain, hyaluronan (HA), stabilized by link protein [66].

Nanomechanical studies of cartilage and its extracellular matrix components have shown the potential to link molecular structure and interactions to tissue-level biomechanical properties. Recently, we reported the use of atomic force microscope (AFM)-based instruments to quantify the compressive nanoscale deformation between opposing chemically end-grafted monolayers of CS-GAGs [136, 137] and aggrecan [27, 28]. These biomimetic model systems demonstrated highly nonlinear nanomechanical behavior, with the aggrecan layer stiffness increasing more rapidly with strain than that of CS-GAG layer. The contribution of electrostatic interactions to the compressive stiffness of the CS-GAG [137] and aggrecan [28] layers was well described by a Poisson-Boltzmann-based model representing GAG chains as finite length charged rods [26]. In other related studies, nanoindentation of intact porcine cartilage was performed

using microsized colloidal probe tips to measure the tissue aggregate dynamic compressive modulus ($\sim$ 2.6 MPa), while the use of sharp pyramidal nanosized probe tips gave values $\sim$ 100-fold lower ($\sim$ 0.02 MPa) and were thought to be more indicative of molecular fine structure [143, 32]. Nanoindentation was also used to detect changes in tissue-level properties following enzymatic digestion of collagen and proteoglycan moieties [143], during the process of osteoarthritis degradation [86], and cartilage tissue repair [143, 32]. Single molecule force-extension measurements on HA [51, 70] and CS-GAG [70] have been performed using optical tweezers [51] and AFM [70], respectively, giving estimates of the persistence length in near-physiological aqueous solution conditions. With the goal of providing insights into joint lubrication mechanisms [126], the frictional properties of HA have been quantified using the surface force apparatus (SFA) via covalent attachment of HA to lipid bilayers on mica [6] and electrostatic adsorption of HA on quaternized poly(4-vinylpyridine) [170] or lipid bilayers [147] on mica. AFM using microscale probe tips has also been used to measure the frictional coefficient of the surface of bovine articular cartilage in the presence and absence of the superficial zone [89], and found that it was similar to macroscale results [120, 169].

While the compressive and tensile stiffness of cartilage ECM constituents have been studied at the molecular level, the molecular contributions to cartilage shear properties have received less attention. It is recognized from tissue-level biomechanical studies that aggrecan and GAG intermolecular interactions play an important role in resisting shear deformation of cartilage [83, 169, 13], given the high density of aggrecan within the tissue ($20 - 80$ mg/mL [100]). In addition, the known ionic strength dependence of the torsional shear modulus of cartilage disks was well predicted by a Poisson-Boltzmann-based unit cell model of GAG-GAG electrostatic interactions [83]. Hence, the objective of this study was to quantify the nanoscale lateral deformation behavior of chemically end-grafted aggrecan monolayers to better understand the origins of tissue-level shear behavior (as opposed to surface lubrication).

Toward this end, lateral force microscopy (LFM) was carried out on microcontact printed planar substrates [163] of chemically end-grafted fetal bovine cartilage

aggrecan prepared at high physiological densities with surface molecular separation distances $\sim$ 25 nm [28]. Nanosized (end-radius, $R \sim 50$ nm) and microsized ($R \sim 2.5$ μm) probe tips functionalized with neutral hydroxyl-terminated self-assembled monolayers (OH-SAMs) were employed to study lateral nanomechanics at different length scales where the interactions involved either a few or a large ensemble ($\sim 10^3$) of aggrecan molecules [28]. Lateral force was measured as a function of normal compressive force ($\sim 0-80$ nN), enabling the determination of the lateral proportionality constant, μ, in NaCl solutions of varied ionic strength ($0.001 - 1.0$ M, pH $\sim$ 5.6). The use of microcontact printed surfaces enabled the simultaneous measurement of aggrecan height (and hence, conformation and compressive normal strain) with lateral and normal force. Results using probe tips having differing surface chemistries suggested that the contribution of interfacial adhesion between the aggrecan layer and probe tip to the measured lateral force were very small compared to the effects of aggrecan deformation. To help isolate the effects of electrostatic and nonelectrostatic interactions on the resistance of aggrecan to lateral deformation, lateral forces were measured as a function of aggrecan height at different bath ionic strengths. Height was then converted to effective normal strain, ϵ_n, and the measured lateral force was estimated as a function of the ratio of the average GAG-GAG spacing to the characteristic electrical Debye length at each ionic strength. (Electrostatic interactions become relatively more important as this ratio becomes smaller.) The underlying time independent (elastic-like) and time dependent (e.g., visco/poroelastic) deformation mechanisms were also explored by comparing the lateral forces measured at different probe tip displacement rates.

3.2 Methods

3.2.1 Sample and probe tip preparation and characterization

Purified fetal bovine epiphyseal A1A1D1D1 aggrecan, MW $\sim$ 3 MDa [110] was chemically functionalized with thiol-groups, as described previously [27]. Micro-

contact printed [163] samples were prepared where aggrecan was chemically end-grafted within hexagonal patterns (10 μm side length), and a hydroxyl-terminated self-assembled monolayer (OH-SAM, 11-mercaptoundecanol, $HS(CH_2)_{11}OH$, Aldrich, St. Louis, MO), was functionalized outside the hexagonal patterns, as described previously [27]. The aggrecan packing density was one monomer per $\sim$ 25 nm $\times$ 25 nm square (measured using the dimethylmethylene blue dye binding assay [45]). Samples were characterized using contact mode AFM imaging in NaCl solutions at different ionic strengths to visualize the height differences between the aggrecan-OH-SAM pattern using both the OH-SAM functionalized nanosized and microsized probe tips [27, 28]. Patterned control substrates of carboxyl- and amine-terminated SAMs (COOH-SAM and NH_2-SAM) were prepared in a similar fashion via microcontact printing using 3 mM 11-mercaptoundecanoic acid, $HS(CH_2)_{10}COOH$ (Aldrich), and 2-aminoethanethiol hydrochloride, $HS(CH_2)_2NH_2 \cdot HCl$ (Aldrich, 24 hour incubation), both in ethanol. These control samples were imaged by lateral force microscopy in 0.01 M NaCl at pH $\sim$ 2.4 and 10.3 (pH values were adjusted using HCl and NaOH) to measure the lateral forces between the probe tip and the samples (for reviews of measuring friction forces on SAMs via LFM, see [148, 17, 90, 103]).

Both standard nanosized AFM probe tips ($R \sim 50$ nm as measured by scanning electron microscopy, NP tip D, silicon nitride, V-shaped cantilever, nominal spring constant $k \sim 0.06$ N/m, Veeco, Santa Barbara, CA) and microsized colloidal probe tips ($R \sim 2.5$ μm, silicon nitride, V-shaped cantilever, nominal spring constant $k \sim$ 0.12 N/m, BioForce Nanosciences, Ames, IA) were used. Both were coated with 2 nm of Cr and 50 nm of Au, and then functionalized with neutral OH-SAMs by immersion for 24 hours in 3 mM $HS(CH_2)_{11}OH$ ethanol solution, to minimize the electrostatic and hydrophobic interactions between the tip and aggrecan layer. A hydrophobic methyl-functionalized microsized probe tip was also prepared by immersion for 24 hours in 3 mM ethanethiol, $HSCH_2CH_3$ (Aldrich), ethanol solution. Based on the surface interaction area calculated from the measured probe tip radii and the known aggrecan packing density, the nanosized tips (Figure 3-2a) were estimated to interact directly with $<$ 10 aggrecan on the surface, while the microsized tips (Figure 3-2b)

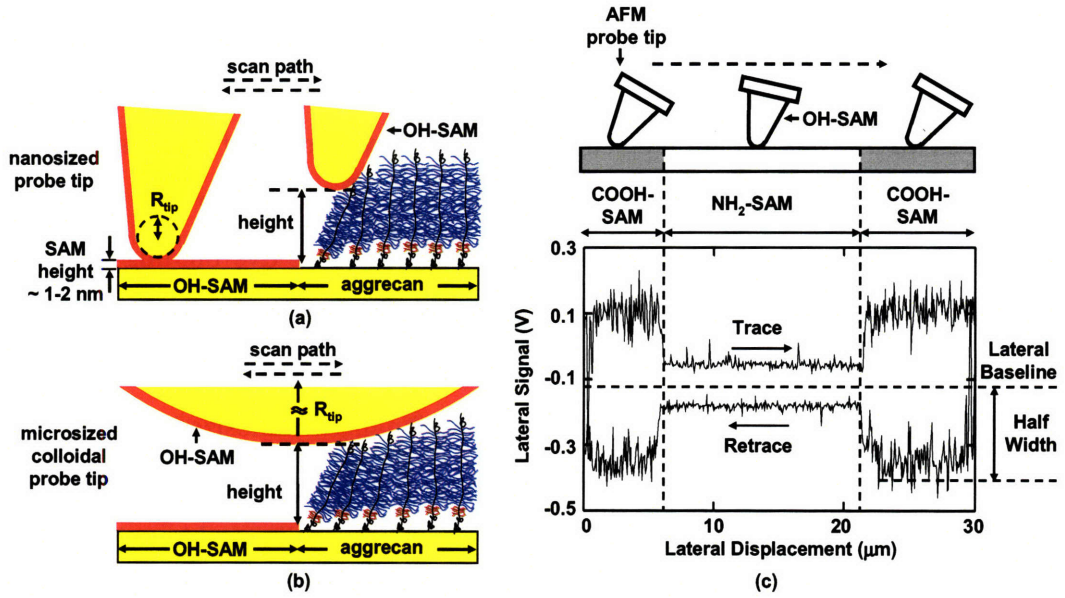

Figure 3-2: Illustrations of AFM contact mode imaging on aggrecan and OH-terminated SAM patterned substrate on which the spacing between adjacent core proteins of the aggrecan molecules are $\sim$ 25 nm apart; (a) nanosized probe tip with an end-radius, $R \sim 50$ nm; (b) microsized colloidal probe tip, $R \sim 2.5$ μm. (c) Schematic of one lateral signal loop from a single line scan crossing a COOH-NH_2 self assembled monolayer (SAM) pattern using an OH-SAM functionalized nanosized probe tip ($R \sim 50$ nm, nominal cantilever spring constant, $k \sim 0.06$ N/m) in 0.01 M NaCl solution at pH $\sim$ 10.3, adjusted by adding NaOH (not drawn on scale).

interacted with $\sim 10^3$ aggrecan [28].

3.2.2 Shear nanomechanics of aggrecan via lateral force microscopy

A Multimode Nanoscope IV AFM (Veeco, Santa Barbara, CA) was used with a PicoForce piezo for the lateral force microscopy experiments. The scan direction was parallel to the base of the V-shaped cantilever, i.e., a 90° scan angle. As the cantilever scans across the surface under a constant applied normal force (Figure 3-2c) it twists in the scanning (lateral) direction, resulting in a horizontal deflection of the laser spot on a quadrant position sensitive photodiode which outputs a lateral deflection signal

(Volts). Simultaneously, the cantilever bends in the normal direction and results in a separate output as the normal deflection signal (Volts) on the same photodiode. The normal deflection signal is of a greater magnitude and the cross-talk, or interference of the normal to the lateral signal, is typically an order of magnitude larger than the actual lateral deflection signal caused by the cantilever twisting [113]. To account for this, both forward (trace) and reverse (retrace) line scans ("lateral signal loops") were performed. The magnitude of the lateral force was calculated from the average of the lateral deflection signal (i.e., one half the trace minus retrace signal, or "half-width", Figure 3-2c). Calibration of the lateral sensitivity α (nN/V) was conducted using an extension of the "wedge method" [113, 157], thus enabling quantification of the lateral force in nN (see Appendix B). The normal deflection sensitivity β (nN/V) was determined by calibrating the normal cantilever spring constant via the thermal oscillation method [79]. Based on these methods, lateral force scans were measured at 8 locations on each hexagon as a function of the applied normal force, probe tip displacement rate, and bath ionic strength ($0.001 - 1.0$ M NaCl solutions, pH ~ 5.6). The proportionality coefficient between lateral force and applied normal force, μ, which characterizes the resistance of the aggrecan layer to lateral deformation at given applied normal forces, was estimated via linear regression on the data pooled from all eight scan positions and reported as the mean (least squares estimator) $\pm$95% confidence interval for each lateral versus normal force curve. The validity of pooling the data was tested using one-way analysis of variance test (ANOVA) followed by Tukey-Kramer post-hoc multicomparison test; there were no significant differences in the means between each of the eight scan lines at any given ionic strength (IS) or pH, suggesting that the properties of the aggrecan across the hexagon were relatively homogeneous.

During lateral force microscopy scans, the height difference between the aggrecan and OH-SAM regions was recorded simultaneously (Figure 3-2a,b), which equals the aggrecan layer height as the height of OH-SAM layer is negligible small ($\sim 1 - 2$ nm) [27]. Hence, simultaneous assessment of aggrecan height (and hence, conformation and compressive normal strain) with lateral and normal force was obtained, as

previously described [27, 28]. Lateral force was plotted versus aggrecan height and compressive normal strain, ϵ_n, which was calculated as the aggrecan height normalized by the equilibrium aggrecan height at $\sim$ zero applied normal force [28]. A 30 μm scan size and 1 Hz scan frequency were employed at a lateral scan rate 60 μm/s. In an additional series of experiments, a range of lateral scan rates from $\sim 1 - 100$ μm/s was employed. For each individual scan line, 256 data points were recorded on each trace and retrace line. Ten data points at the beginning and end of the loop (the tip reversal region), and ten data points corresponding to each pattern edge were excluded. Lateral force microscopy images of individual aggrecan-functionalized hexagons, demonstrating the lateral cantilever deflection signal at each scan location (proportional to the absolute value of lateral force), were also created to directly visualize the lateral force contrast between the inside and outside of the hexagonal patterned areas of the microcontact printed surfaces.

3.3 Results

3.3.1 Control experiments – friction between nanosized OH-SAM probe tip versus COOH-NH_2 SAM microcontact printed surface

A hexagonal microcontact printed COOH- and NH_2-SAM functionalized substrate (where the COOH-SAM was outside and the NH_2-SAM was inside the hexagons) was imaged with an OH-SAM nanosized probe tip in 0.01 M NaCl at pH $\sim$ 10.3 and 2.4, with an applied normal force $\sim$ 5 nN. Thirty-micrometer (30 μm) lateral force scans images (Figure 3-3) were constructed from the half-width of the lateral signal loop (Figure 3-2c). At pH $\sim$ 10.3, the negatively charged COO^--SAM exhibited a higher lateral force than the NH_2-SAM, corresponding to the brighter area outside of the hexagon in Figure 3-3a and the larger half-width in the lateral signal loop (Figure 3-2c) compared to that of the NH_2-SAM. The COO^--SAM also exhibited larger lateral signal fluctuations due to "stick-slip" phenomena (Figure 3-2c) [149].

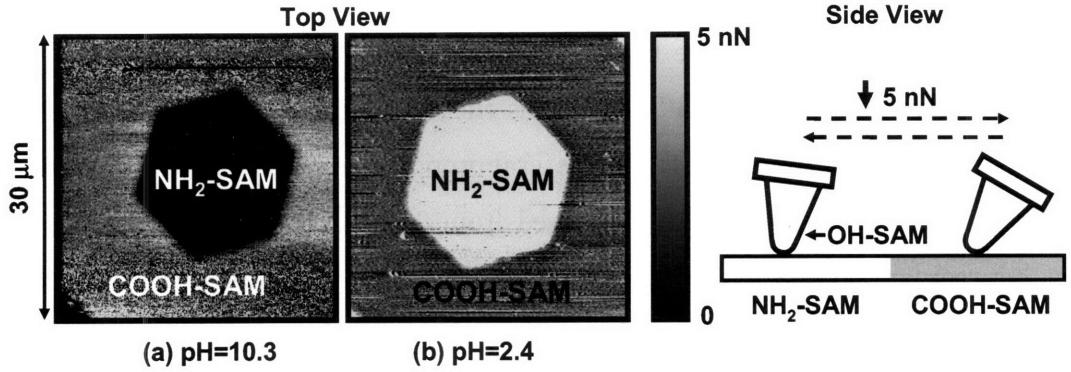

Figure 3-3: Lateral force images of a COOH-NH_2 SAM patterned substrate taken with an OH-functionalized nanosized probe tip probe tip ($R \sim 50$ nm, nominal cantilever spring constant, $k \sim 0.06$ N/m) under ~ 5 nN applied normal force in 0.01 M NaCl solutions at pH ~ 10.3 and 2.4, (pH was adjusted by adding HCl or NaOH, COOH-SAM was outside the hexagon, NH_2-SAM inside).

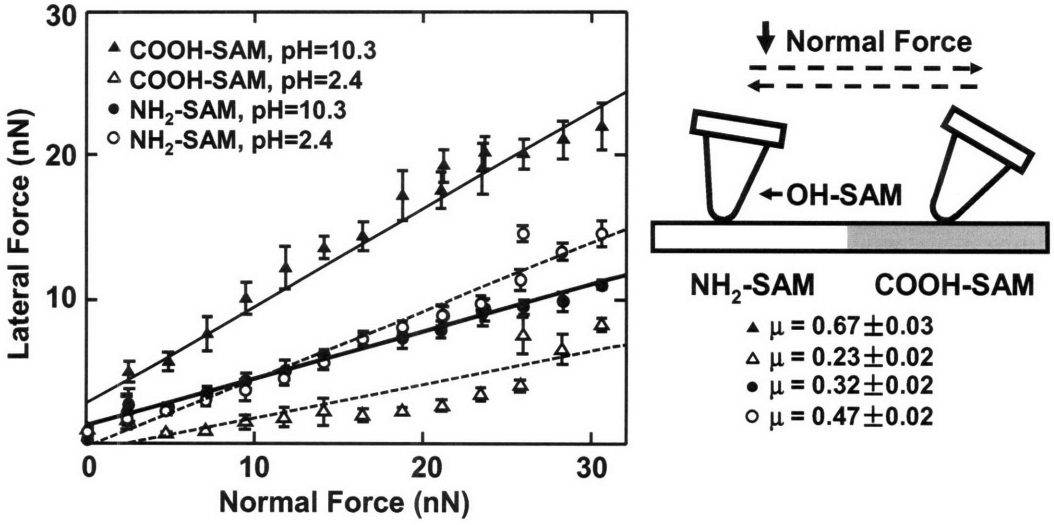

Figure 3-4: Lateral force as a function of normal force on a COOH-NH_2 SAM patterned substrate in 0.01 M NaCl at different pH values, using an OH-functionalized nanosized probe tip ($R \sim 50$ nm, nominal cantilever spring constant, $k \sim 0.06$ N/m). Each data point represents the mean ($\pm$ SD) of lateral signal loops at eight different locations across one hexagon pattern, where each loop consists of up to 256 data points. The value μ (mean $\pm 95\%$ confidence interval), the proportionality coefficient between lateral and normal force, was calculated here and in subsequent figures via linear regression on the data pooled from all eight locations.

In contrast, the NH_2-SAM showed higher lateral force at pH $\sim$ 2.4 (Figure 3-3b). Lateral forces showed a positive linear dependence with increasing normal force for both the NH_2-SAM and COOH-SAM versus the OH-SAM functionalized probe tip at pH $\sim$ 10.3 and 2.4 (Figure 3-4). The lateral proportionality coefficient, μ, between carboxyl and hydroxyl, markedly decreased from 0.67 ± 0.03 to 0.23 ± 0.02, while that between amino and hydroxyl increased from 0.32 ± 0.02 to 0.47 ± 0.02, as the pH was decreased from 10.3 to 2.4 (Figure 3-4). Visualization of the pattern reversal at different pH (Figure 3-3) and the linear dependence of lateral on applied normal force (Figure 3-4) verified the lateral force microscopy methodology by reproducing results reported previously in the literature [154].

3.3.2 Aggrecan shear using a nanosized probe tip

Lateral force images for a microcontact printed surface of chemically end-grafted aggrecan (inside the hexagon) and an OH-SAM (outside the hexagon) were taken with a nanosized OH-SAM functionalized probe tip in 0.1 M NaCl at pH $\sim$ 5.6 (Figure 3-5a). Lateral force data from this experiment were obtained at low ($\sim$ 3 nN) and high ($\sim$ 15 nN) normal imaging forces, as seen in two typical signal loops of Figure 3-5b, with a 30 μm line scan. The half width of the lateral signal and, hence, the magnitude of the lateral resistance, was much smaller for the aggrecan compared to the OH-SAM at the low applied normal force (Figure 3-5a), and increased with increasing normal force (Figure 3-6) [113]. (Note that a shift in the baseline of the lateral signal loop was observed at the edge of the hexagonal pattern due to the increase in aggrecan height, but this did not affect the magnitude of the measured lateral force given the linear response of position sensitive photo diode. This cross-talk came from the interference of cantilever normal deformation with the lateral deflection signal, which was deconvoluted by analyzing the trace-retrace scan loop, as mentioned in Methods.)

Figure 3-6 illustrates the dependence of lateral force on normal force for this same sample; each data point represents 8 line scans at different sample locations for a 30 μm scan size. Data in the OH-SAM region (Figure 3-6a) yielded a linear dependence

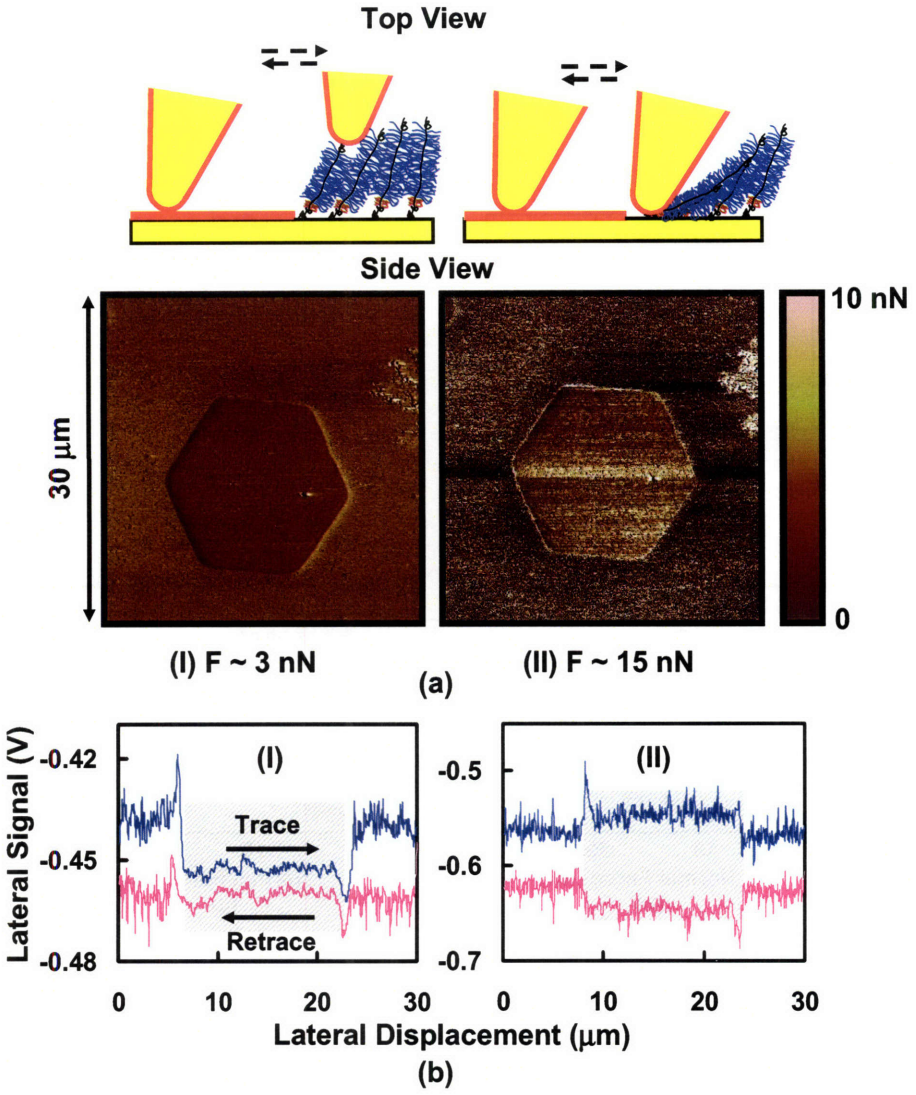

Figure 3-5: (a) Lateral force images of aggrecan-OH SAM patterned substrate in 0.1 M NaCl solution at pH $\sim$ 5.6, with an OH-SAM functionalized nanosized probe tip ($R \sim 50$ nm, nominal cantilever spring constant, $k \sim 0.06$ N/m). (The red layer in the schematic represents OH-SAMs, as in Figure 3-2a+b). (b) Corresponding lateral force loop signals across a full pattern of the aggrecan-OH-SAM region; the shaded regions in the lateral signal loops are the regions representing the aggrecan brushes. (I) normal force, $F \sim 3$ nN; (II) $F \sim 15$ nN.

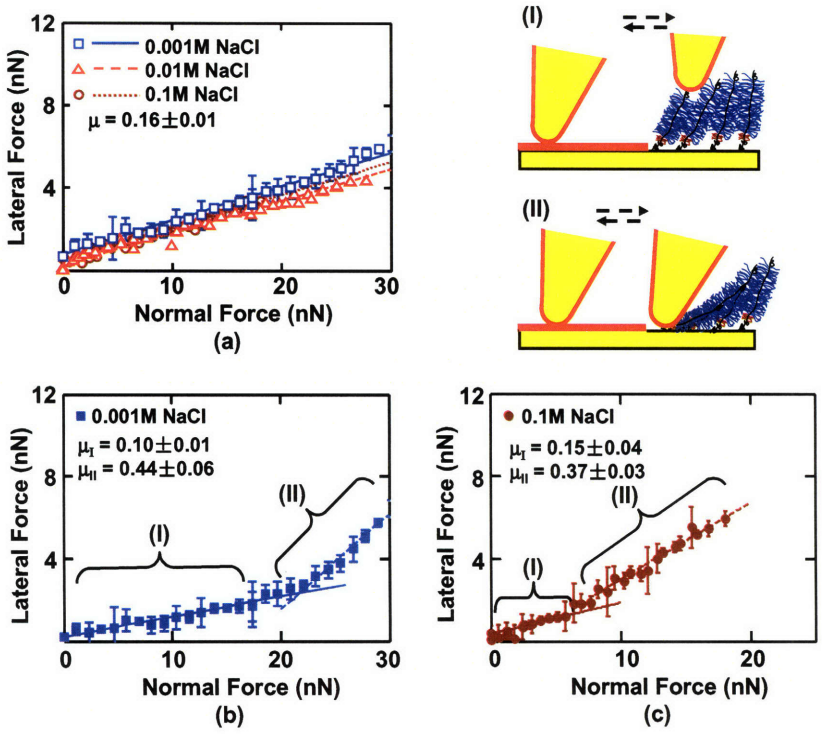

Figure 3-6: Lateral force versus applied normal load for an aggrecan-OH SAM patterned surface with an OH-SAM functionalized nanosized probe tip ($R \sim 50$ nm) in NaCl solutions, pH ~ 5.6. (a) OH versus OH. (b) OH versus aggrecan at 0.001 M IS. (c) OH versus aggrecan at 0.1 M IS. At 0.01 M, lateral linearity ratio μ is measured to be $\mu_I = 0.10 \pm 0.01$ and $\mu_{II} = 0.35 \pm 0.03$ in region (I) and (II), respectively (data not shown). Each data point represents the mean ($\pm$ SD) of at 8 different locations across one hexagon pattern at a fixed applied normal force.

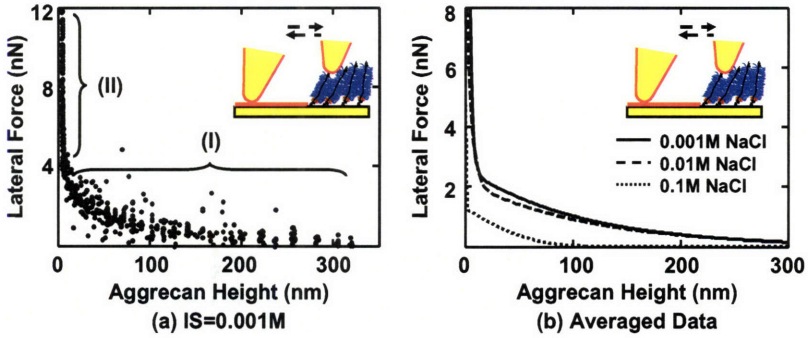

Figure 3-7: Aggrecan lateral force versus height in NaCl solutions, pH $\sim$ 5.6 using a nanosized OH-SAM functional tip ($R \sim 50$ nm, nominal cantilever spring constant, $k \sim 0.06$ N/m). (a) IS = 0.001 M; each data point represents one lateral signal loop, and the aggrecan brush height is recorded simultaneously. Region I: lower normal loads (< 20 nN), where aggrecan molecules are not highly compressed and lateral forces are expected to originate from molecular shear, rotation and bending. Region II: higher normal forces (> 20 nN), where aggrecan molecules are highly compressed and "stick-slip" mechanisms are observed in the lateral signal loops. (b) Averaged aggrecan lateral force versus height curves at different IS; 0.001 M data correspond to that shown in (a).

of lateral force on normal force with $\mu = 0.16 \pm 0.01$, which was independent of ionic strength in the range of $0.001 - 0.1$ M, as expected for neutral SAMs. For the aggrecan-functionalized region, two linear regimes were observed: one at lower forces (region I) and one at higher forces (region II, Figure 3-6b,c). In region I, μ was found to be $\mu_I = 0.10 \pm 0.01$ at 0.001 and 0.01 M IS and $\mu_I = 0.15 \pm 0.04$ at 0.1 M IS. In region II, μ increased to $\mu_{II} = 0.44 \pm 0.03$, 0.35 ± 0.03 and 0.37 ± 0.03 at 0.001, 0.01, and 0.1 M IS, respectively. The applied normal force at which this transition occurred was found to decrease with increasing ionic strength (e.g., Figure 3-6b,c). It should be noted that scanning under high force in region II produced damage to the aggrecan layer causing irreversible changes in the measured height and lateral force. Lateral force also depended markedly on aggrecan height (Figure 3-7). In the low force region of constant lateral linearity (region I), the aggrecan layer was not fully compressed (Figure 3-7a); in the higher force region II, the aggrecan layer was compressed to < 5 nm. The lateral force in both regimes depended on ionic strength

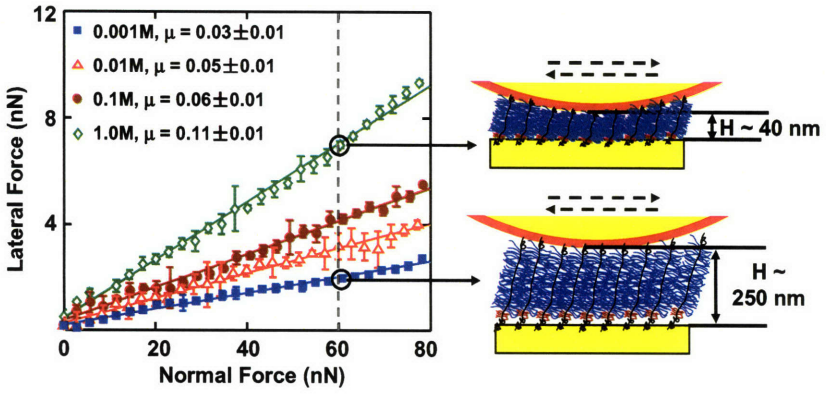

Figure 3-8: Lateral force versus normal force for aggrecan brush using an OH-functionalized microsized probe tip ($R \sim 2.5$ μm) in NaCl solutions, pH $\sim$ 5.6. Each data point represents the mean ($\pm$ SD) of lateral signal loops at 8 different locations across one hexagon pattern. Higher lateral force was measured at higher IS for the same normal force, as aggrecan layer height became smaller.

(Figure 3-7b): at any given aggrecan layer height, the lateral force increased with decreasing ionic strength.

3.3.3 Aggrecan shear using a microsized probe tip

Lateral forces between aggrecan and an OH-SAM microsized probe tip ($R \sim 2.5$ μm) were measured over a range of applied normal force between 0 and 80 nN. It is known that in this force range, the aggrecan layer is never fully compressed [28]. Lateral force was observed to vary linearly with normal force throughout the entire range of applied normal force (Figure 3-8). μ was found to be independent of loading history for several loading and unloading cycles in the range of applied normal force (data not shown), indicating a lack of damage to the aggrecan layer during scanning. A marked increase of μ with increasing ionic strength was observed, ranging from $\mu = 0.03 \pm 0.01$ at 0.001 M to 0.11 ± 0.01 at 1.0 M (Figure 3-8). The same sample was tested using the CH_3-SAM tip at 0.1 M and 1.0 M, and no significant differences in the values of μ were observed compared to the OH-SAM tip (data not shown). As shown in Figure 3-9a, the initial aggrecan layer height was greater at lower ionic strength; at any measured

height, the lateral force was larger at lower ionic strength. When these same data were plotted as a function of compressive strain ϵ_n (aggrecan height normalized to initial height at approximately zero normal force), the lateral force was found to decrease with increasing ionic strength at constant strain (Figure 3-9b). To aid in the interpretation of these results (see Discussion), the lateral force data of Figure 3-9b were replotted versus the estimated ratio of the GAG spacing divided by Debye length, the characteristic electrostatic interaction length, at different ionic strengths, to distinguish between electrostatic and non-electrostatic interactions (Figure 3-9c). The estimated average GAG spacing corresponding to varying amounts of aggrecan compression was calculated as,

$$\text{GAG spacing under compression} = \text{GAG spacing along core protein} \times \frac{\text{measured aggrecan height}}{\text{aggrecan contour length}}$$

where the GAG spacing along core protein is 3.2 ± 0.8 nm, and the contour length is 398 ± 57 nm for fetal epiphyseal aggrecan, as measured via tapping mode AFM imaging [110]. The value of GAG spacing under compression divided by Debye length is < 1 at lower IS (0.001 and 0.01 M) and > 1 at higher IS (0.1 and 1.0 M) in the range of measured lateral forces.

The lateral proportionality coefficient μ varied with the tip displacement rate in the range $\sim 1 - 100$ μm/s (Figure 3-10) in a manner that depended on ionic strength. At higher IS (0.1 and 1.0 M), μ increased significantly with tip displacement rate (confirmed by one-way ANOVA test at each ionic strength, Figure 3-10). In contrast, at IS = 0.001 M, μ did not change significantly with tip displacement rate. The trends reported in this study were found to be reproducible using at least 3 different microcontact printed samples for each experiment. The variability of the data are most likely associated with the local grafting density of the aggrecan layer within a hexagonal pattern and the previously quantified degree of aggrecan polydispersity [110]. Variations between hexagons were found to be less important.

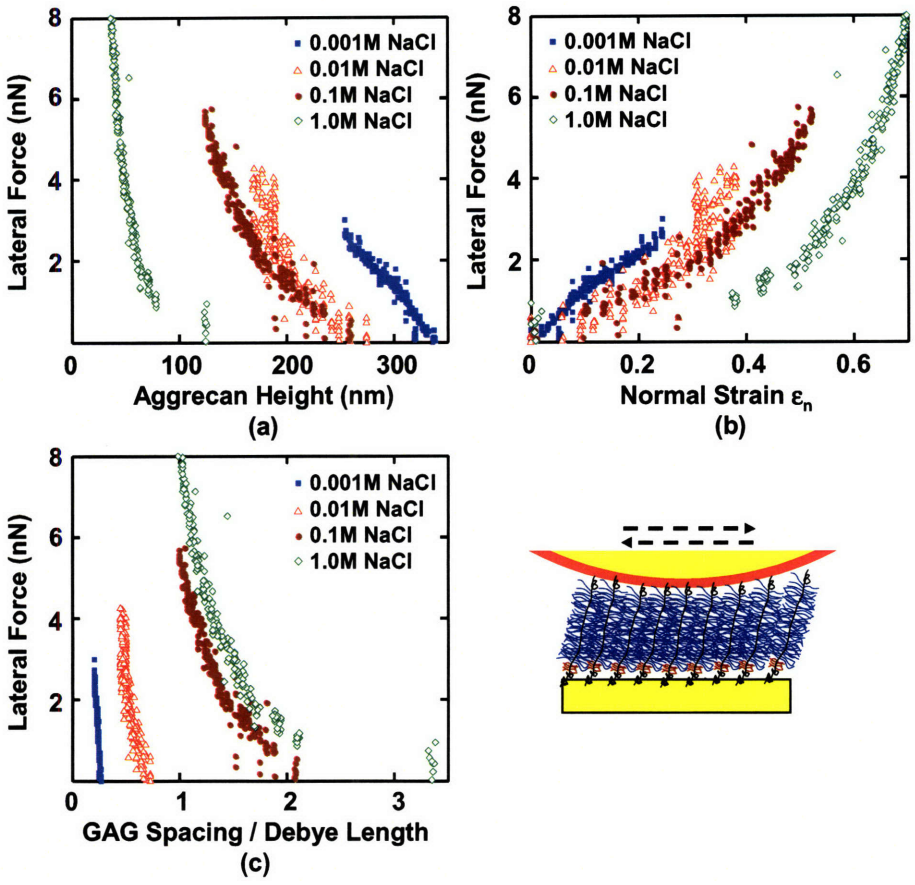

Figure 3-9: Lateral force versus (a) aggrecan layer height, (b) normal strain ϵ_n, (c) GAG spacing normalized to the Debye length, using an OH-functionalized microsized tip ($R \sim 2.5$ μm) in NaCl solutions, pH ~ 5.6. Each data point represents one lateral signal loop. Normal strain ϵ_n was calculated as the compressed aggrecan layer height normalized to its uncompressed height measured by AFM imaging at approximately zero normal force.

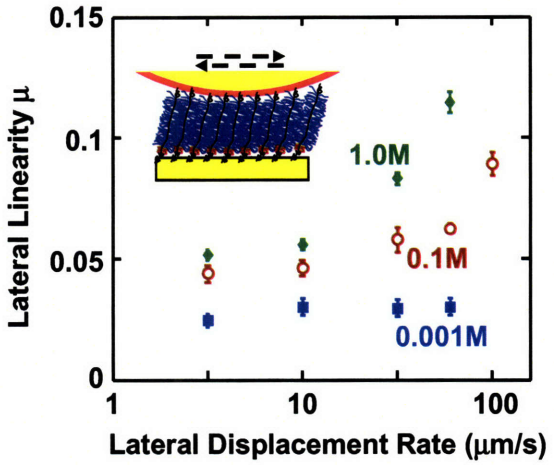

Figure 3-10: Lateral proportionality coefficient μ as a function of lateral tip displacement rate (from 3.16 to 100 μm/s) in NaCl solutions, pH $\sim$ 5.6, calculated as the least squares estimator $\pm$95% confidence interval from eight series of applied normal forces at the same IS and lateral displacement rate. μ varied significantly with displacement rate at 0.1 M and 1.0 M IS, (one-way ANOVA, $p < 0.0001$); no significant effect of rate was found at 0.001 M. μ was found to vary significantly with IS and rate (two-way ANOVA test, followed by Tukey-Kramer post-hoc multicomparison test, $p < 0.0001$).

3.4 Discussion

3.4.1 Control experiments – friction between nanosized OH-SAM probe tip versus COOH and NH_2-SAM micro-contact printed substrates

The inversion of the lateral force image pattern on the COOH-SAM compared to the NH_2-SAM sample (Figure 3-3a,b) is consistent with the ionization state of the end-functional groups at different pH, as previously reported [154]. At pH $\sim$ 2.4, the COOH-SAM is fully protonated ($pK_a^{surf} \sim 5.2$) while NH_3^+-SAMs are fully ionized ($pK_b^{surf} \sim 7$) [155]. At this pH, greater lateral force was measured between the OH-SAM tip and NH_3^+-SAM due to intermolecular hydrogen bonds between -NH_3^+ and -OH that are stronger than those between -COOH and -OH. At pH $\sim$ 10.3, the NH_2-SAM is nearly neutral while the COO^--SAM is completely ionized and, thus, there is a stronger adhesion force between the -COO^- and -OH functional groups due to stronger hydrogen bonds [154]. The "stick-slip" behavior and linear dependence of lateral force on applied normal force is consistent with previous results on SAM systems [148], and is known to correlate with adhesion of the end-functional groups [149]. The magnitude of the lateral proportionality coefficient μ may depend on many experimental factors including surface roughness, contact area, sliding speed, temperature, etc. [53], but relative trends, such as the effect of pH, are accurately assessed. The greater pH dependence of μ in the carboxyl SAM region can be attributed to the larger increase of electronegativity of the carboxyl groups by ionization, and hence the larger magnitude change of the hydrogen bonding energy [148], and thus adhesions, between hydroxyl and carboxyl SAMs from the protonated to the charged state.

3.4.2 Molecular origins of the aggrecan shear response using the microsized tip

The radius of curvature of the microsized tip is an order of magnitude larger than aggrecan height, aggrecan-aggrecan surface separation distance and the interaction

distance between the aggrecan layer and the probe tip. Thus, the ensemble of aggrecan molecules located within the tip-substrate contact area are subjected to a more uniform deformation compared to that produced by the nanosized tip, which may penetrate into the aggrecan layer. The finding that the lateral force was independent of loading history over many loading-unloading cycles suggests that the aggrecan(thiol)-gold end-grafting was stable for the experimental conditions used ($\sim$ 2 hrs for each ionic strength condition). The μ values measured in the lateral force experiments presented here may have two possible origins: through-thickness molecular-molecular interactions and/or surface interactions between the OH-SAM probe tip and the chain segments of the aggrecan in physical contact with the probe tip. Surface interactions are expected to be minimal, since it was observed that there was negligible adhesion between the aggrecan and OH-SAM tip for normal force measurements under the same conditions tested [28]. This hypothesis is further supported by the fact that no marked difference was observed between μ measured with tips having varied surface chemistry. Hence, through-thickness molecular-molecular interactions are expected to dominate and may include electrostatic repulsion, non-electrostatic repulsion (e.g., entropic, steric, excluded volume, bending, etc.), and/or molecular entanglements.

An electrostatic contribution to the shear resistance is evident in Figure 3-9a where it is observed that at any constant aggrecan layer height, the lateral force increases with decreasing IS. At the same time, clear differences in the lateral force are observed with ionic strength at constant values of the ratio of GAG spacing to Debye length (Figure 3-9c), which supports the hypothesis that nonelectrostatic interactions also contribute to aggrecan shear resistance. Theoretical studies on polymer compression have suggested that more compacted configurations have higher nonelectrostatic interactions, e.g. excluded volume effect [101]. Hence, the reduction in lateral force at a given strain ϵ_n with increasing ionic strength (Figure 3-9b), is likely due to the decrease in electrostatic repulsion interactions. This finding is also consistent with the observation that at constant normal force, greater lateral force was measured at higher IS (Figure 3-8), which would result in higher compaction of the aggrecan layer due to increased screening of electrostatic interactions.

3.4.3 Aggrecan shear response using the nanosized probe tip

For the microsized probe tip, a constant proportionality ratio μ was observed in the range of applied normal force in all tested IS (Figure 3-8). By comparison, the nanosized probe tip highlighted the existence of two different regimes of linearity in the response with applied normal force (Figure 3-6b,c). Higher normal force resulted in full compression or penetration of the tip through the aggrecan layer [27], possibly bringing the tip into contact with the underlying gold substrate. The differences in lateral force mechanisms in regions I and II (Figure 3-6b,c) can be interpreted by analyzing the shape of lateral signal loops (Figure 3-5) as well as the corresponding aggrecan height and conformation (Figure 3-7). When the aggrecan was fully compressed or penetrated at high normal force, the lateral force was likely dominated by surface interactions between the probe tip and gold layer under the aggrecan (shaded, Figure 3-5b (II)). At low normal force, lateral signals in the aggrecan region (shaded, Figure 3-5b (I)) had much smaller variations compared to those in the OH-SAM region, where the lateral forces were dominated by "stick-slip" surface interactions [149]. The transition between different lateral force mechanisms also support the hypothesis that surface interactions between aggrecan and the OH-SAM tip were small.

Under the microsized tip, a degree of normal and lateral confinement of aggrecan within the layer is expected, since $\sim 10^3$ aggrecan are compressed simultaneously. However, due to the pyramidal geometry of the nanosized tip, only $2-4$ aggrecan molecules are directly interacting with the tip and the measured aggrecan height does not necessarily represent the amount of aggrecan compression in the normal direction. Penetration of the nanosized tip into the aggrecan layer could result in both splay deformation (bending) as well as compression even in the absence of tip lateral displacement. Regardless of these geometrical factors, a linear dependence of lateral force on applied normal force was still observed in the normal force region I in Figure 3-6b,c and Figure 3-7. Although μ did not markedly vary with IS in this region (Figure 3-6 b,c), as was observed using the microsized probe tip (Figure 3-8), a strong IS-dependence was observed between lateral force and aggrecan height (Figure

3-7b). Thus, due to stronger electrostatic repulsion at lower IS, larger normal forces were required to reach a given compressed height, and electrostatic repulsion was stronger in the lateral directions as well. The nanosized probe tip has a larger lateral proportionality coefficient in region I at IS $= 0.001 - 0.1$ M compared to that with the microsized tip which is likely due to length scale and/or geometrical effects. Thus, the two lateral linearity regions measured via the nanosized probe tip (Figure 3-6b,c) helped to interpret the underlying molecular origins of aggrecan shear and to assess the lateral deformation mechanisms of a few aggrecan molecules. By comparison, the microsized tip serves to contrast the effects of compressive and lateral deformation of a larger ensemble of aggrecan molecules, and thereby more closely simulates the deformation of aggrecan within cartilage tissue.

3.4.4 Rate-dependence of aggrecan shear

The significant increase in μ with tip lateral displacement rate at 0.1 and 1.0 M IS (Figure 3-10) suggests that time dependent (e.g., viscoelastic and/or poroelastic) as well as time independent (elastic) processes are involved in lateral deformation of aggrecan. In contrast, at low IS (0.001 M) as elastic electrostatic interactions become even more dominant, no significant change in μ with displacement rate was observed (Figure 3-10). Viscoelastic behavior may be associated with interpenetration, entanglements and macromolecular friction between aggrecan molecules. Poroelastic behavior may result from lateral deformation-induced fluid flow within and through the densely-packed aggrecan layer and the associated local pressure gradients within the layer, which results in hydrodynamic friction between water and end-attached aggrecan [64, 38], as is known to occur within cartilage tissue [108, 50]. Such rate-dependent phenomena become relatively more important as rate-independent electrostatic interactions decrease with increasing IS. From the data presented here, we cannot yet distinguish between viscoelastic and poroelastic contributions, which are the subject of ongoing studies focusing on scaling approaches to the size and rate of interactions [18]. Interestingly, previous studies of the compressive nanomechanics of aggrecan, where electrostatic effects were dominant, showed negligible dependence of

aggrecan compressive stiffness on normal tip displacement rate in the range of $0.1-10$ μm/s [28].

3.4.5 Comparison to reported polyelectrolyte lateral force studies

While this study has focused on the shear deformation of the end-grafted aggrecan layer, it is still instructive to compare our findings to recent literature on the surface lubrication properties of polyelectrolytes. Feiler et al. [47] recently used LFM to measure surface forces and frictions associated with adsorbed cationic polyelectrolyte layers of very low charge density, using a similar microsized probe tip geometry ($R \sim 10$ μm) and range of lateral displacement rates ($\sim 10-100$ μm/s). Their measured values of μ in 10^{-4} M KBr were higher than the largest measured μ for aggrecan even at the highest IS of 1.0 M (Figure 3-9), at which electrostatic interactions are screened. Values of μ reported for negatively charged adsorbed polyelectrolyte layers measured using the surface forces apparatus [6, 147] at the lowest ionic strength comparable to our study were higher than that found here as well, while in some other negatively charged polyelectrolyte systems, extremely low values of the effective lateral coefficient μ_{eff} (the ratio of lateral to normal force) were also observed [126]. These differences are likely associated with differences in the molecular structure of the polyelectrolytes of interest, the arrangement of the adsorbed versus end-anchored attachment, the existence of free polyelectrolyte molecules in solution, the geometry of the opposing layers in the SFA versus AFM configuration, the lateral displacement velocity (>5 fold higher in the AFM), and the higher applied normal forces used in the SFA experiments. Nevertheless, a similar trend was observed in both AFM and SFA systems demonstrating that the presence of electrostatic interactions between charged polyelectrolytes effectively reduced the lateral forces at constant normal force [126].

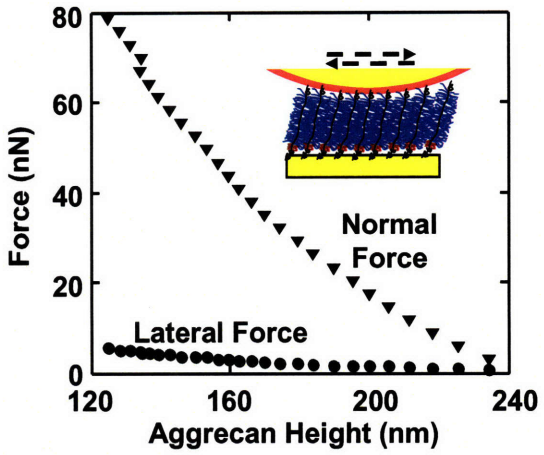

Figure 3-11: Comparison of aggrecan layer resistance to normal and shear deformation using an OH-functionalized microsized tip ($R \sim 2.5$ μm), 0.1 M NaCl, pH ~ 5.6.

3.4.6 Comparison to macroscopic shear of cartilage tissue

We first note that the observed decrease in the resistance of aggrecan to shear deformation with increasing IS (Figure 3-9) is consistent with the previously reported decrease in both the equilibrium and dynamic torsional shear modulus of cartilage disks with increasing IS at constant disk thickness *in vitro* [83]. During macroscopic deformation of cartilage *in vivo*, aggrecan would be expected to deform in both normal and lateral directions enmeshed within the collagen fibrillar network. In this study, end-attached aggrecan molecules undergo both compression and shear simultaneously. However, while the macromolecules are end-attached to the substrate, the lateral displacement of the aggrecan is not measured, as they are not attached to the tip or to each other like a network. Therefore, it is difficult to define a shear strain (or shear modulus) for the layer in the configuration of Figure 3-2a,b. Assuming aggrecan to be a rigid rod, the maximum shear deformation at 0.1 M was estimated to be ~ 0.95 of the aggrecan contour length; however, aggrecan is more coiled at physiological conditions and the actual deformation is likely much less. In native cartilage tissue, aggrecan is enmeshed within a collagen fibril network. While the configuration of Figure 3-2a,b (without the collagen network) does not replicate the mechanical constraints that reg-

ulate aggrecan deformation within native tissue, our goal is to help further establish a molecular-level understanding of cartilage tissue mechanics by isolating the different components of aggrecan deformation. To this end, the magnitudes of both the normal and lateral force as a function of aggrecan layer height using the microsized tip, replotted from the data of Figures 3-8 and 3-9, are compared in Figure 3-11 at near physiological IS (0.1 M NaCl). At any given height (normal deformation), the normal force is $\sim$ 10 fold larger than the shear force. Conversely, aggrecan resistance to shear deformation is $\sim$ 10% of its resistance to compression in this layer configuration. In native cartilage, the equilibrium shear modulus is typically $\sim$ 50% that of the compressive modulus [169]. Thus, while the experiments presented here delineate the lateral deformation properties of aggrecan layers having molecular packing densities similar to that in tissue, it is clear that interactions between aggrecan and the enveloping collagen network are also critically important for a complete understanding of the tissue-level biomechanical properties of cartilage. Ongoing studies are therefore focused on lateral nanomechanical interactions between aggrecan and collagen, and between aggrecan macromolecules enmeshed within a collagen network.

3.5 Conclusions

In this study, we examined the shear nanomechanics of aggrecan macromolecules using microcontact printing and lateral force microscopy involving deformation of a few aggrecan or a large assembly of them using nanosized or microsized probe tips, respectively. By deforming a large assembly of aggrecan at physiological concentration, the microsized tip more closely mimics deformation of aggrecan within native cartilage tissue. Using this approach, aggrecan shear force was found to depend linearly on normal force. Both electrostatic and nonelectrostatic interactions at the molecular level were identified by using a combination of probe tip geometries, functionalizations, environmental (e.g., IS) conditions, and appropriate normalization of the data. Stronger electrostatic interactions resulted in larger shear resistance at the same layer height and normal strain, accompanied by more elastic-like deformation (i.e., less rate

dependence). At physiological IS, the rate dependence of the lateral force strongly suggested the presence of visco- and/or poroelastic behavior, consistent with tissue-level aggrecan and GAG-GAG interactions that have been identified in the study of intact cartilage shear behavior.

Chapter 4

Nanoscale Shear Deformation Mechanisms of Opposing Cartilage Aggrecan Macromolecules

The nanoscale shear deformation behavior of two opposing end-grafted aggrecan layers was studied in aqueous solutions using atomic force microscopy, and was observed to depend markedly on bath ionic strength, the presence of calcium ions, and the applied lateral displacement rate. These results provide molecular-level insights into the contribution of aggrecan deformation mechanisms to cartilage tissue-level material properties.

This chapter was published as a biophysical letter in Biophysical Journal in 2007 [63].

4.1 Introduction

Aggrecan, the most abundant proteoglycan in cartilage comprising $30-35\%$ of tissue dry weight, has a densely-packed array of highly negatively charged chondroitin sulfate glycosaminoglycan (CS-GAG) chains along its core protein [65] and is critical to cartilage mechanical function [99]. Recently, we quantified shear interactions within a chemically end-grafted aggrecan layer using neutral nanosized and microsized (col-

loidal) probe tips via lateral force microscopy (LFM) [62]. At near physiological ionic strength (IS = 0.1 M, pH $\sim$ 5.6), linearity was observed between lateral and normal forces applied to the aggrecan (linearity ratio $\mu = 0.06 \pm 0.01$ at 60 μm/s lateral displacement rate). Both electrostatic and nonelectrostatic contributions to shear interactions were identified, and μ increased nonlinearly with lateral displacement rate to 0.09 ± 0.01 at 100 μm/s. These results suggested the presence of visco/poroelastic rate processes within the aggrecan layer at the nanoscale [62]. Here, we report lateral interactions between two opposing end-attached aggrecan layers, a configuration that more closely mimics aggrecan interactions during shear deformation of intact cartilage *in vivo*. In addition, we demonstrate the effects of Ca^{2+} at physiological concentration on these shear interactions, along with effects of varying bath IS and displacement rate.

4.2 Methods

Hexagonal patterned substrates with end-anchored bovine fetal epiphyseal aggrecan inside 10 μm-sided hexagons, and neutral hydroxyl-terminated self-assembled monolayers outside the hexagons (OH-SAM, height $\sim$ 1 nm, $HS(CH_2)_{11}OH$, Aldrich, St. Louis, MO), were prepared via microcontact printing, as described previously [27]. Aggrecan packing density was within the physiological range (one aggrecan per $\sim$ 25 nm $\times$ 25 nm, or $\sim 24 \pm 5$ mg/mL at 0.1 M IS [27]). Aggrecan functionalized probe tips were prepared in a similar fashion by 48 hrs incubation of gold-coated colloidal probe tips (end radius $R_{tip} \sim 2.5$ μm, nominal spring constant $k \sim 0.12$ N/m, BioForce Nanosciences, Ames, IA) in 100 μL of the 1 mg/mL thiol-functionalized aggrecan solution [28]. By these methods, $\sim 10^3$ aggrecan molecules in each layer could interact simultaneously. Normal and lateral forces were measured and calibrated using a MultiMode Nanoscope IV atomic force microscope (AFM) with a PicoForce piezo (Veeco, Santa Barbara, CA) via LFM [62]. The total height of the two opposing aggrecan layers (H in Figure 4-1a) was measured by AFM imaging of microcontact printed surfaces [28]. H was converted to normal strain ϵ_n by normalization to the height

measured by AFM imaging at negligible normal force [62]. The measured aggrecan layer height and lateral force were independent of loading history, suggesting that there was negligible shear-induced irreversible damage or conformational changes in the end-attached aggrecan layers.

4.3 Results and Discussion

Upon shear deformation (Figure 4-1a), the measured lateral force varied linearly with applied normal force (Figure 4-1b); at a given normal force, the lateral force increased with increasing IS. Lateral force increased nonlinearly with decreasing aggrecan height (Figure 4-1c) and increasing normal strain (Figure 4-1d) at all IS. At constant height (Figure 4-1c) the lateral force decreased with increasing IS, but the lateral force was less sensitive to changes in IS at constant strain (Figure 4-1d). These trends for two opposing aggrecan layers were similar to those observed with a single layer sheared by a neutral hard-wall OH-SAM probe tip [62], except for those of Figure 4-1d, where differences with IS were more pronounced in the single layer. Differences in lateral deformability as a function of IS at constant aggrecan height and strain (Figure 4-1c,d) suggest the presence of electrostatic interactions. Nonelectrostatic interactions (e.g., excluded volume, steric, entropic, van der Waals, and possible molecular interpenetration and/or entanglement) were evident in the two-layer configuration, as demonstrated by marked differences in lateral force with changes in IS when calculated at constant values of the ratio of GAG spacing to electrical Debye length (Figure 4-1e), which were also observed in the single-layer studies [62].

Interestingly, there were important differences between the two-layer system studied here and the single-layer system studied previously [62]. In general, the lateral force between the opposing aggrecan layers (Figure 4-1b-e) was observed to be $\sim 20-50\%$ less than that in the single layer [62] under the same experimental conditions, i.e., normal force, normal strain, and IS, similar to the trend observed for normal compressive loading [28]. The increased lateral compliance of two opposing layers compared to a single layer is attributed to a change in the molecular mecha-

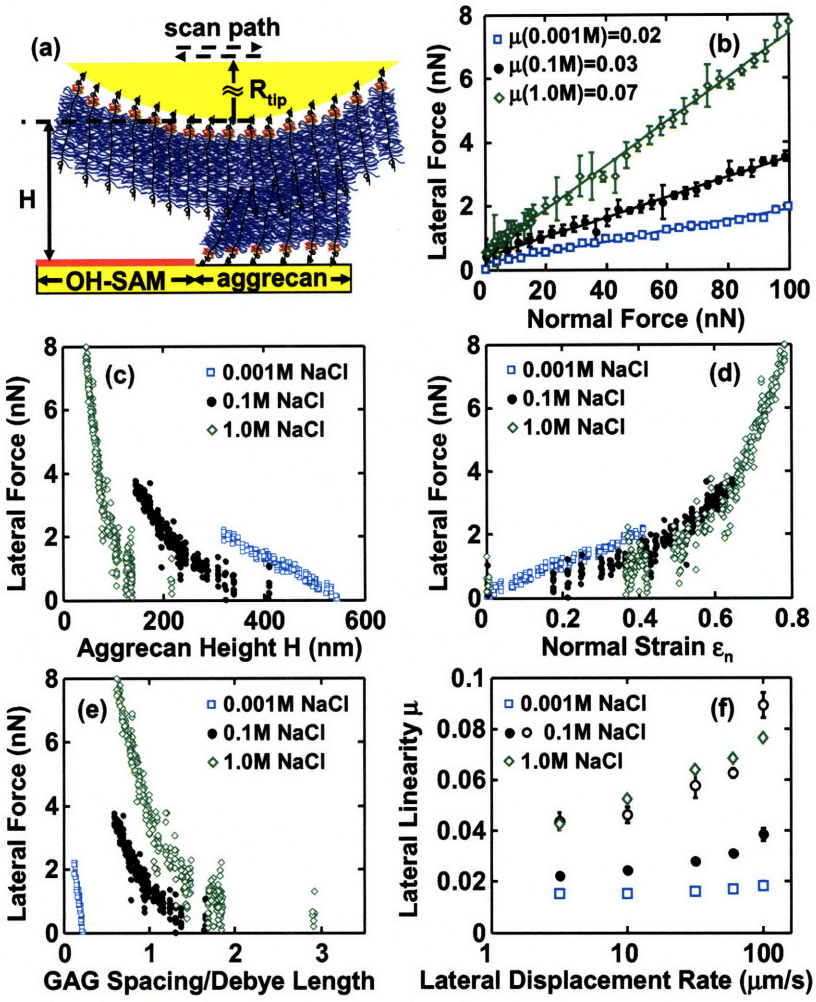

Figure 4-1: (a) Lateral motion of two opposing aggrecan layers using an aggrecan functionalized probe tip ($R_{tip} \sim 2.5$ μm) on an aggrecan-OH-SAM micropatterned sample. (b) Lateral versus applied normal force (mean $\pm$ SD, $n = 8$ different locations), 95% confidence interval of $\mu < \pm 0.01$, estimated via least-squares linear regression (LSLR), $R^2 > 0.92$ for all IS. (c) Lateral force versus total height H of two aggrecan layers. (d) Lateral force versus normal strain ϵ_n. (e) Lateral force versus estimated ratio of GAG spacing to Debye length. Each data point in (c)-(e) represents one lateral scan. (f) Lateral proportionality μ versus lateral tip displacement rate (mean $\pm$95% confidence interval at $n = 8$ different locations via LSLR, $R^2 > 0.88$ for all data). Open circles denote μ measured via an OH-SAM tip at 0.1 M IS, adapted from Han et al. [62] ($R^2 > 0.81$ for all data). Effects of displacement rate (one-way ANOVA, $p < 0.0001$ at all IS) and IS (two-way ANOVA, $p < 0.0001$) are significant. Experiments performed in NaCl, pH $\sim$ 5.6.

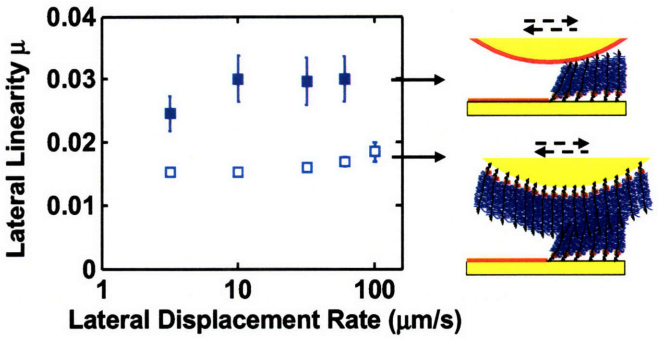

Figure 4-2: Comparison of lateral proportionality μ versus lateral tip displacement rate (mean $\pm 95\%$ confidence interval at $n = 8$ different locations via LSLR by pooling the data) at 0.001 M IS, measured via both the OH-SAM and aggrecan functionalized probe tips. $R^2 > 0.87$ for the shear of one single layer, and $R^2 > 0.88$ for the shear of two opposing layers. Effect of displacement rate is significant for the shear of two opposing layers (one-way ANOVA, $p < 0.0001$) and nonsignificant for the shear of one single layer (one-way ANOVA, $p > 0.05$). Data measured by the OH-SAM tip is adapted from Han et al. [62], for comparison.

nisms of deformation [28]. One possibility is interpenetration of aggrecan layers which is expected to increase the degree of molecular mobility compared to the single layer system in which lateral deformation is more restricted by the use of a hard-wall probe tip. Secondly, the local z-dependent charge density distribution for opposing layers would be altered compared to a single layer system with the highest charge density in the region of interpenetration. Together, these effects could result in less resistance to shear deformation of each aggrecan macromolecule. At the same normal strain ϵ_n (Figure 4-1d), lateral forces at different IS did not vary as markedly as those of the single layer [62], Figure 4-2, further suggesting that conformational mobility is an important determinant of lateral resistance. Lateral force increased significantly with lateral displacement rate at $0.001 - 1.0$ M IS (Figure 4-1f). Rate-dependent mechanisms may include viscoelastic processes such as molecular friction between chain segments, molecular reorientation/reconfiguration, and possible interpenetration and entanglement of adjacent aggrecan. Poroelastic rate processes could occur, related to local fluid flow within and through the aggrecan molecules. With increasing IS, nonelectrostatic components become relatively more important, consistent with our

observation that the rate dependence was more pronounced at higher IS. In contrast to Figure 4-1f, the lateral linearity coefficient for a single layer of aggrecan at 0.001 M IS did not show rate dependence [62]. This difference is consistent with the possibility of interpenetration of the two opposing aggrecan layers where nonelectrostatic interactions would be important even at low IS. Adhesion-related friction mechanisms [149] appear to contribute minimally to shear resistance, as adhesion between the two opposing layers became important only when the layers were held in contact statically for sufficient time to equilibrate. We found previously that rapid detachment of the two layers resulted in negligible adhesion compared to the measured shear force [61]. Here, no surface equilibration time was allowed during scanning and, as a result, adhesions between opposing layers were small.

We then studied the effect of physiologically relevant calcium concentration on the shear behavior of opposing aggrecan layers ($[Ca^{2+}] \sim 2-4$ mM in synovial fluid [99]). Addition of divalent ions can also decrease electrostatic interactions in biological polyelectrolyte systems [57]. The experiments of Figure 4-3 were performed using a buffer of NaCl + $CaCl_2$: $[Cl^-]$ was maintained at 0.15 M and as $CaCl_2$ was added, NaCl was decreased accordingly. Increasing $[Ca^{2+}]$ from ~ 0 to 0.2 to 2 mM caused an increase in μ (Figure 4-3a); however, further increases in $[Ca^{2+}]$ from 2 to 75 mM did not change μ. The presence of Ca^{2+} is thought to enhance electrostatic screening by its valence and preferential distribution closer to GAGs than monovalent ions [121]. Thus, the increase in μ with initial addition of Ca^{2+} (Figure 4-3a) is consistent with the trend seen with increasing [NaCl] in Figure 4-1b. In addition, however, Ca^{2+} (but not Na^+) can simultaneously neutralize negative charge groups by binding to both the carboxyl and sulfate moieties along the GAG chains within each of the aggrecan layers [95, 78]. Together, the screening and binding effects of Ca^{2+} can both lead to compaction of the two aggrecan layers, as seen in the decreased height at any given normal force (Figure 4-3b). This decreased height is equivalent to a decrease in the compressive stiffness of the combined opposing layers.

Interestingly, at a given height, aggrecan shear resistance was approximately the same at any $[Ca^{2+}]$ in the 0.2 to 75 mM range, though greater than 1 M NaCl

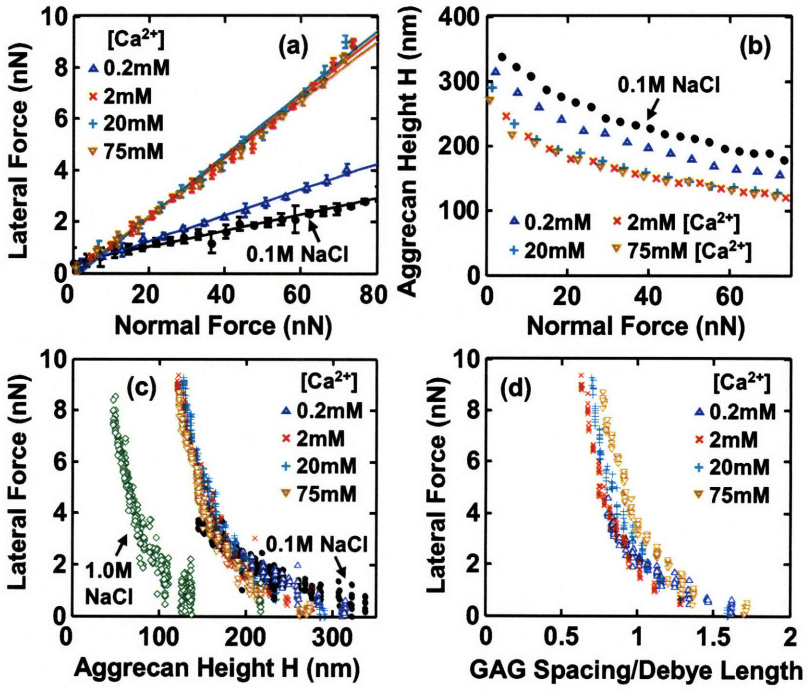

Figure 4-3: (a) Lateral versus applied normal force (mean ± SD, $n = 8$ different locations), $\mu = 0.05$ at 0.2 mM $[Ca^{2+}]$ and 0.12 at $2 - 75$ mM $[Ca^{2+}]$, 95% confidence interval of $\mu < \pm 0.01$ via LSLR, $R^2 > 0.97$ for all $[Ca^{2+}]$. (b) Aggrecan total height H versus applied normal force ($n = 8$, SD < data size). (c) Lateral force versus height H. (d) Lateral force versus estimated ratio of GAG spacing to Debye length. In (c,d) each data point represents one lateral scan. Experiments performed in NaCl + $CaCl_2$ solutions with $[Cl^-] = 0.15$ M, varying $[Ca^{2+}]$ and $[Na^+]$; pH ~ 5.6. Data at 0.1 M NaCl in (b) is adapted from Dean et al. [28], for comparison.

(Figure 4-3c). These data are replotted as a function of the ratio of GAG spacing to Debye length, as calculated for multivalent electrolyte solutions (Figure 4-3d) [121]; again, lateral force appeared insensitive to added $[Ca^{2+}]$ in the $0.2 - 75$ mM range. Electrostatic double layer repulsive interactions are similar at a constant value of this ratio under certain limiting conditions [62, 121]. Since increased screening would decrease long range electrostatic contributions to shear resistance at constant height and constant GAG spacing-to-Debye length ratio (Figure 4-3c,d) [88], the non-specific screening effects associated with Ca^{2+} appear less important. Binding effects appear to saturate at $[Ca^{2+}] \sim 2$ mM (Figure 4-3a,b), consistent with the reported values of binding constants of Ca^{2+} to GAGs [35, 138]. Taken together, binding of Ca^{2+} to GAGs affects both aggrecan compressive and shear mechanical properties, consistent with the known effects of Ca^{2+} on cartilage tissue mechanics [57, 35]. Adhesive interactions due to Ca^{2+}-bridging between the two opposing aggrecan layers had minimal effect on aggrecan shear in the present study, since the constant displacement rate does not allow the surface equilibration times (approximately seconds) necessary for adhesions between aggrecan to occur [61].

In vivo, up to ~ 100 aggrecan molecules are end-attached to hyaluronan filaments forming supramolecular aggregates enmeshed within a three-dimensional-collagen network [65, 99]. Deformation and interactions between adjacent aggrecan occur within native cartilage as the tissue deforms during joint loading. While the two-dimensional-end-attached aggrecan layer configuration used here is not identical to that within cartilage, our use of an aggrecan packing density within the physiological range [99] enables this system to replicate certain features of bulk tissue deformation, providing molecular-level insights into cartilage material properties. For example, joint loading results in a combination of cartilage compression and shear, and their simultaneous effects on densely packed aggrecan can be studied with the present system (Figures 4-1,4-3). Importantly, our nanoscale shear studies of opposing aggrecan layers demonstrate molecular-level rate and Ca^{2+} dependent properties which are consistent with macroscopic poro-viscoelastic tissue properties [57, 138], suggesting their importance to biomechanical functions.

4.4 Conclusions

In this study, shear deformation mechanisms of two opposing aggrecan layers demonstrated both electrostatic (elastic-like) and nonelectrostatic (rate-dependent) interactions, and nonelectrostatic effects became more important at higher IS due to Debye screening. Lateral interactions between two aggrecan layers exhibited smaller shear resistance than that with a single layer [62], and significant rate dependence was observed at all IS tested. The presence of Ca^{2+} ions significantly increased aggrecan shear resistance by reducing its normal compressibility, while the contribution from ion bridging-induced adhesion was minimal at rates of interest here.

Chapter 5

Cartilage Aggrecan Can Undergo Self-Adhesion

Here, we report that aggrecan, the highly negatively charged macromolecule in the cartilage extracellular matrix (ECM) undergoes Ca^{2+}-mediated self-adhesion (due to both chemical and physical interactions) after static compression even in the presence of electrostatic repulsion in physiological-like solution conditions. We propose a new hypothesis that aggrecan self-adhesion, and the macromolecular energy dissipation that results from this self-adhesion, could be an important factor contributing to the self-assembled architecture and integrity of the cartilage ECM *in vivo*.

5.1 Introduction

It has long been hypothesized that intra- and intermolecular electrical double layer and steric (e.g., entropic, excluded volume) repulsive interactions between the densely packed, highly negatively charged glycosaminoglycans (GAG) of aggrecan [65] (Figure 5-1a-c) are critical determinants of the unique biomechanical properties of cartilage tissue, in particular its compressive [165] and shear [83] stiffness. This hypothesis was initially developed based on the known molecular structure and chemical composition of aggrecan (first determined in the 1970s [109] and later imaged directly by Ng et al. [110]) and then confirmed by the measurement of tissue-level biomechanical prop-

erties of cartilage having varying GAG contents [99] and in different electrolyte solution conditions [83, 37]. It has been suggested that aggrecan also plays a critical role within connective tissues by protecting the collagen fibrillar network, within which it is embedded, from proteolytic degradation [125] as well as mechanical overload [67]. Only with recent nanotechnological advances have the local molecular interactions between aggrecan and their constituent GAG chains been directly quantified using biomimetic model systems, new surface patterning methodologies, high resolution force spectroscopy instrumentation, and Poisson-Boltzmann based electrostatic molecular-level continuum and atomistic-level modeling [27, 28, 63, 62, 4]. These studies have elucidated the molecular origins of biomechanical properties by showing that nanoscale trends in the biomimetic aggrecan systems are reflected in macroscale tissue-level behavior, e.g., the dependences of nanomechanical properties on bath ionic strength, calcium ion concentration, and displacement rate. Previous work has focused on the effects of molecular-level repulsive forces during compression and shear of aggrecan [27, 28, 63, 62]. Surprisingly, we have discovered and report here for the first time, that aggrecan macromolecules can also undergo self-adhesion and energy dissipation under certain conditions even in the presence of strong electrostatic repulsion, e.g., if they are compressed together for a sufficient amount of time. Recent studies have recognized the importance of binding interactions between aggrecan with a variety of extracellular matrix (ECM) and pericellular matrix (PCM) macromolecules, including the collagens, small proteoglycans, and other glycoproteins in the organization and stability of the aggrecan-rich matrix [30, 92]. Carbohydrate-carbohydrate binding has been proposed as critical to cell recognition and adhesion [140], signal transduction [82], and the compaction process of preimplantation embryos in mammals [60]. Certain carbohydrates (e.g., sponge-like) have also been shown to undergo self-interactions due to both non-specific [117] and/or specific binding [124]. Here, we propose a new biological function; that self-adhesion and energy dissipation of aggrecan, as well as other ECM and PCM components, could also be a factor in ECM assembly, organization, and physiological function. In this study, we quantify the self-adhesion forces and energies for two well-defined chemically end-grafted aggrecan

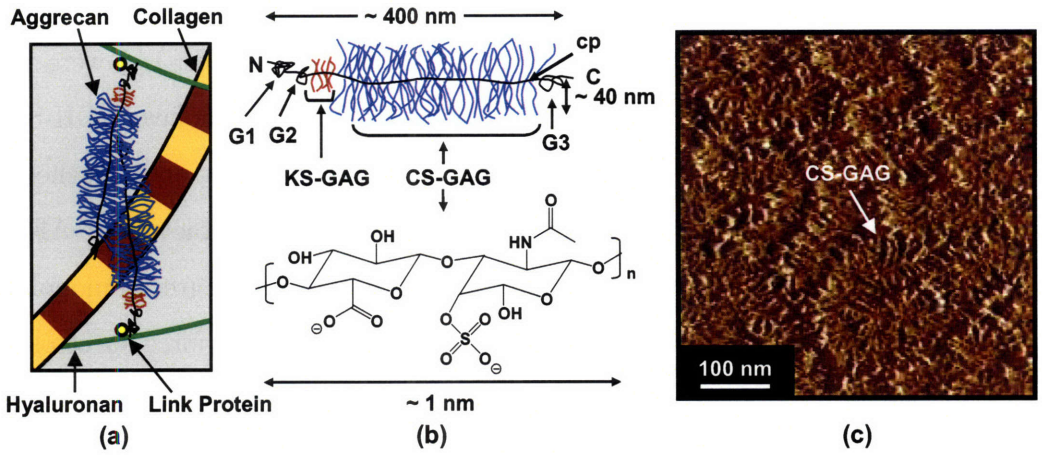

Figure 5-1: (a) Schematic of major load-bearing constituents of cartilage extracellular matrix, including the type II collagen network and proteoglycan (aggrecan). Aggrecan macromolecules are attached to hyaluronan and stabilized via link protein. (b) Schematic of cartilage aggrecan cylindrical brush-like structure (contour length, $L_c \sim 400$ nm, molecular weight ~ 3 MDa) [110], which is composed of a core protein backbone (cp) containing three globular domains (G1, G2, G3), grafted chondroitin sulfate glycosaminoglycan chains (CS-GAG, $L_c \sim 40$ nm, shown as C4S-GAG) with interchain spacing $\sim 2-4$ nm along the cp, and keratan sulfate GAG (KS-GAG) chains; N = N-terminal, C = C-terminal. (c) Tapping mode AFM image of 2D-closely packed fetal epiphyseal aggrecan on atomically flat mica surface at a density that is $\sim 40\times$ less than its physiological concentration in cartilage (adapted from Ng et al. [110]).

layers at physiologically relevant packing densities using colloidal force spectroscopy (Figure 5-2a, see Methods), involving $\sim 10^3$ aggrecan molecules, as a function of displacement rate, compression time, bath ionic strength (IS) [NaCl], and calcium concentration.

5.2 Methods

Purified fetal bovine epiphyseal aggrecan was chemically end-functionalized with thiol-groups and end-attached on a planar gold-coated silicon substrate at a physiologic-like packing density (~ 25 nm intermolecular spacing as previously described, equivalent to ~ 40 mg/mL at 0.1 M IS, as measured via dimethylmethylene blue dye

assay) [27]. Gold-coated spherical colloidal AFM probe tips (end radius $R \sim 2.5$ μm, spring constant $k \sim 0.12$ N/m, BioForce Nanosciences, Ames, IA) were functionalized with a neutral hydroxyl-terminated self-assembled monolayer (OH-SAM, 11-mecaptoundecanol, $HS(CH_2)_{11}OH$, Aldrich, St. Louis, MO) or end-attached aggrecan layer, Figure 5-2a. Aggrecan layer height measured via contact mode AFM in NaCl aqueous solutions suggest the presence of the end-attached aggrecan monolayer, rather than multilayers or other conformations [27, 28]. Colloidal force spectroscopy was performed in $0.001 - 1.0$ M NaCl aqueous solutions at pH ~ 5.6, in which the sample was moved towards the cantilever probe tip (approach) and then after contact, moved away from the cantilever probe tip (retract), using both the OH-SAM and aggrecan functionalized tips. Retraction of the z-piezo was carried out after a surface dwell time ($\sim 0 - 30$ sec) at a constant normal force ($F_{max} \sim 50$ nN) and z-piezo displacement rate ($z = 4$ μm/s). In another series of experiments, F_{max} was varied between $\sim 10 - 60$ nN at $t = 5$ s and $z = 4$ μm/s; z was also varied between $0.1 - 10$ μm/s at $t = 1$ s and $F_{max} \sim 45$ nN. Similar experiments were performed using the aggrecan functionalized tip with NaCl + $CaCl_2$ aqueous solutions at varying desired $[Ca^{2+}]$, but varying $[Na^+]$ to maintain a constant $[Cl^-] = 0.15$ M. The adhesive interaction distance D_{ad}, maximum adhesion force F_{ad} and adhesive interaction energy E_{ad} were recorded from each force-distance curve (Figure 5-2a).

5.3 Results and Discussion

Aggrecan self-adhesion was observed given sufficient surface dwell or equilibration hold time ($\sim$ seconds) at a constant compressive load for ionic strengths ranging from $0.001-1.0$ M NaCl, pH ~ 5.6 (including near physiological solution conditions of 0.1 M NaCl, pH ~ 5.6) for both neutral hydroxyl-terminated self-assembled monolayer (OH-SAM) and aggrecan-functionalized colloidal probe tips versus aggrecan-functionalized planar surfaces. Figure 5-2a shows typical force versus tip-sample separation distance datasets on approach (i.e., loading; colloidal probe tip advancing towards the planar surface) and retract (i.e., unloading; colloidal probe tip moving away from the pla-

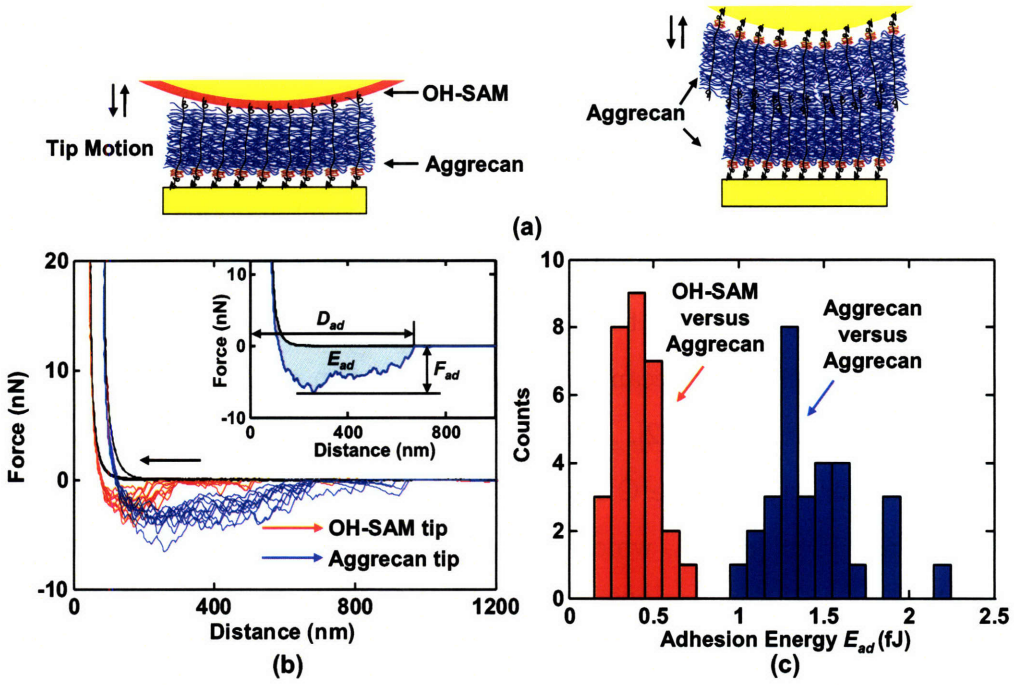

Figure 5-2: (a) Schematic of high resolution force spectroscopy (HRFS) reported in this chapter depicting the interactions between a functionalized planar substrate with end-grafted aggrecan and a hydroxyl-terminated monolayer (OH-SAM) functionalized probe tip or an aggrecan end-grafted colloidal probe tip. (b) Comparison of HRFS force-distance curves obtained via OH-SAM and aggrecan functionalized colloidal probe tips on aggrecan end-grafted planar substrates (1.0 M NaCl aqueous solution, surface dwell time, $t = 30$ s, maximum compressive force, $F_{max} \sim 45$ nN, z-piezo displacement rate, $z = 4$ μm/s). Data for different experiments carried out at ten different locations are shown for each probe tip. Inset: definition of the adhesive interaction distance, D_{ad}, the maximum adhesion force, F_{ad}, and the adhesion energy E_{ad} from each pair of approach-retract force-distance curves. Statistically significant differences were observed for F_{ad} of OH-SAM versus aggrecan tips compared to aggrecan-functionalized probe tips (ANOVA, $p < 0.001$)). (c) Histogram of E_{ad} obtained via OH-SAM and aggrecan-functionalized colloidal probe tips on aggrecan end-grafted planar substrates (1.0 M NaCl aqueous solution, surface dwell time, $t = 30$ s, maximum compressive force, $F_{max} \sim 45$ nN, z-piezo displacement rate, $z = 4$ μm/s).

nar surface) for both the OH-SAM and aggrecan-functionalized probe tips at 1.0M NaCl, pH $\sim$ 5.6 (the solution conditions which exhibited the strongest and longest range adhesive interactions due to salt screening of the electrostatic double layer repulsion forces). Here (Figure 5-2a), a long-range nonlinear attractive force profile was observed on retract with jagged contours, indicating extension of multiple bridging macromolecular chains, where the range of these adhesive forces is observed to be much greater than the expected range for van der Waals interactions [81]. The maximum force on loading, F_{max}, was $\sim 10-60$ nN which imparted compressive molecular strains of $\sim 20-50\%$ (relative to initial layer height at $\sim$ 0 nN compression [62]) which results in a similar aggrecan molecular compaction as that found within non-loaded cartilage *in vivo* [28, 162]. The maximum adhesive interaction distance, D_{ad} (Figure 5-2a), measured by the OH-SAM-functionalized colloidal probe tip (1.0 M, pH $\sim$ 5.6) was 410 ± 100 nm, which agrees well with the known contour length of fetal epiphyseal aggrecan, $L_c = 398 \pm 57$ nm [110]. D_{ad} obtained using the aggrecan-functionalized colloidal probe tip (1.0 M, pH $\sim$ 5.6) was measured to be 755 ± 145 nm, which $\approx 2 \times L_c$ of aggrecan, demonstrating that the adhesive interactions were in fact between two opposing end-attached aggrecan layers, as opposed to the tethering of aggrecan to the underlying substrate. The adhesion force, F_{ad}, was defined as the maximum force observed on retraction, and the adhesion energy, E_{ad}, was defined as the area under the retraction force versus tip-sample separation distance profile (Figure 5-2a).

The carbohydrate-carbohydrate interactions between GAG side chains of aggrecan macromonomers are a balance between a number of possible non-covalent interactions, including attractive secondary intermolecular interactions (e.g., van der Waals contacts, hydrophobicity, hydrogen bonding) [87], physical entanglements resulting from chain diffusion and interpenetration [160], interactions with multivalent cations if present and repulsive interactions (e.g., electrostatic), and repulsive configurational, translational and rotational entropic penalties, hydration effects and local steric hindrance [127]. Each CS-GAG chain contains $\sim 40-50$ disaccharide units [110] in which both polar groups (three hydroxyl, one carboxyl and one sulfate) and nonpolar groups

(one methyl, two sugar rings) are present (Figure 5-1b) [109, 140]. Hydrogen bonds could occur between the $-OH$, $-COOH$, $-COO^-$ and $-OSO_3^-$ groups (pK_a of GAG carboxyl ~ 3 in aqueous solutions [21]). In addition, nonpolar patches along CS-GAG chains can lead to possible van der Waals and hydrophobic interactions [135], Figure 5-3a. It is known that GAG chains have an extended conformation (persistence length ~ 20 nm [110]) due to the limited mobility present in the glycosidic linkage torsions and intermolecular electrostatic interactions [4, 49, 71, 39], and hence, the conformational entropic penalty is expected to be minimal (relative to a random coil) and counterbalanced by the favorable enthalpic decrease from other attractive interactions (e.g. hydrogen bonding, van der Waals, hydrophobicity etc.). Carbohydrate-protein interactions between GAGs and the aggrecan core proteins may also contribute to the aggrecan self-adhesion [109]. However, due to the fact they are surrounded by densely packed GAGs, the binding with protein is most likely unpreferable. It is currently unknown whether the specific complimentarity between GAG segments exist, as has been proposed for glycans [123]. Self-adhesion results in energy dissipation (as reflected by approach-retract hysteresis) due to entropic penalties due to extension of bridging macromolecular chains on retract.

For the OH-SAM functionalized probe tip, adhesion may originate from short-range noncovalent binding between functional groups along aggrecan molecular segments and the OH-SAM, e.g., hydrogen bonding between GAG $-OH$, $-COOH$, $-COO^-$, $-OSO_3^-$ and the OH-terminal groups on the SAM, and/or van der Waals interactions. The increased net adhesion with aggrecan-functionalized probe tips relative to OH-SAM functionalized probe tips (Figure 5-2b,c and Figure 5-3) can be attributed to both chemical and physical factors. Firstly, there is stronger hydrogen bonding between the two aggrecan layers ($-COO^-$ versus $-COOH$, $-COOH$ versus $-COOH$, $-OSO_3^-$ versus $-COOH$) [155] compared to that between the aggrecan layer and OH-SAM probe tip. Secondly, it is possible for interpenetration between opposing aggrecan macromolecules and their GAG branches to occur during compression [110, 28], which results in a larger number of molecular contacts. Additional physical adhesive interactions for the two opposing aggrecan layers include macromolecular

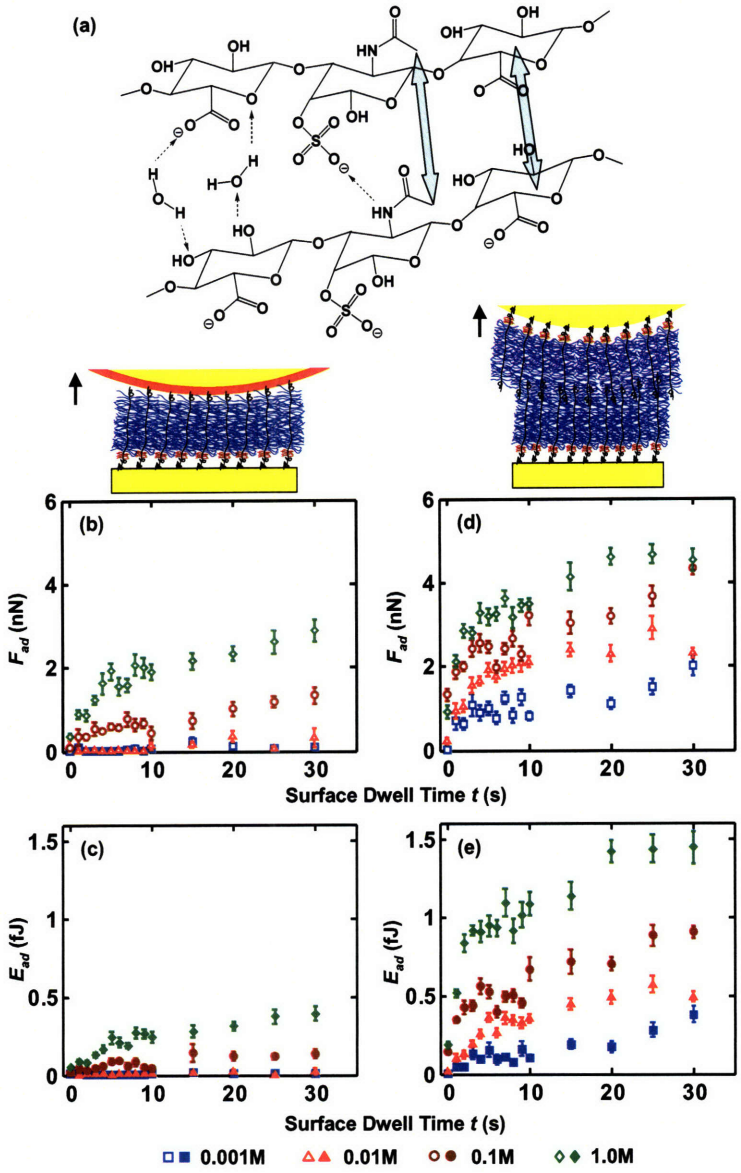

Figure 5-3: (a) Schematic of possible hydrogen bonding (dashed arrows) and hydrophobic interaction (brand arrows) between CS-GAG chains in the presence of water molecules. (b) – (e) Maximum adhesion forces, F_{ad} (open symbols) and total adhesion energy, E_{ad} (closed symbols) as a function of surface dwell time, t between an OH-SAM and an aggrecan-functionalized planar substrate (b, c) and two aggrecan end-grafted layers (d, e) in 0.001 – 1.0 M NaCl, pH $\sim$ 5.6 ($F_{max} \sim 45$ nN, $z \sim 4$ μm/s; mean $\pm$ SEM, $n \geq 30$ for each surface dwell time t at each ionic strength). Statistically significant differences were observed for F_{ad} and E_{ad} at different surface dwell times t and different IS measured by both OH-SAM and aggrecan probe tips (two-way ANOVA, $p_{\mathrm{t}} < 0.0001$, $p_{\mathrm{IS}} < 0.0001$).

entanglements between the two layers.

Figure 5-3 shows the dependence of aggrecan self-adhesion on surface dwell (equilibration) hold time, t, at a constant compressive load and salt concentration [NaCl] for both the OH-SAM and aggrecan-functionalized probe tips versus the aggrecan functionalized planar surfaces. The nonlinearly increasing adhesion force and energey with t for both the OH-SAM and aggrecan-functionalized probe tips (Figure 5-3) is attributed to the time-dependent increase in the number of molecular interactions, which may be facilitated by the configurational rearrangement of aggrecan macromolecules. The trend observed in Figure 5-3 has been observed for many different non-macromolecular systems (e.g., silica versus silicon, and silica versus mica); however, the equilibration time to reach plateau values of F_{ad} and E_{ad} in those systems is typically $\sim 1-2$ seconds (s) [85], which is shorter than that observed for aggrecan (~ 5 s). The time to reach plateau values of F_{ad} and E_{ad} was found to be similar for the OH-SAM functionalized and aggrecan-functionalized probe tips, indicating that the introduction of the second macromolecular layer (on the colloidal probe tip) did not delay the formation of adhesive interactions. As observed in Figure 5-3b,c, there is minimal adhesion between the OH-SAM functionalized probe tip and aggrecan at the lower ionic strengths ($0.001-0.01$ M NaCl) in the presence of strong electrostatic double layer repulsion. The larger adhesion observed between two opposing aggrecan layers at these lower salt concentrations, Figure 5-3d,e, could be the result of both increased regions of molecular contact between two aggrecan layers, stronger molecular interactions, and the presence of physical adhesive interactions, e.g., molecular entanglements. As the ionic strength is increased, the electrostatic double layer repulsion is screened as reflected in a decrease in the electrical Debye length, both resulting in a decrease in CS-GAG molecular spacing [28].

In the presence of Ca^{2+}, the adhesive interaction energy E_{ad} experienced a ~ 4 fold increase from 0 to 75 mM $CaCl_2$ at fixed $[Cl^-] = 0.15$ M (Figure 5-4). This significant increase, even at the near physiological $[Ca^{2+}] = 2$ mM, could be due ion-bridging effects associated with the presence of multivalent ions [23], as it is known that one Ca^{2+} can bind electrostatically between two monovalent negative charges on

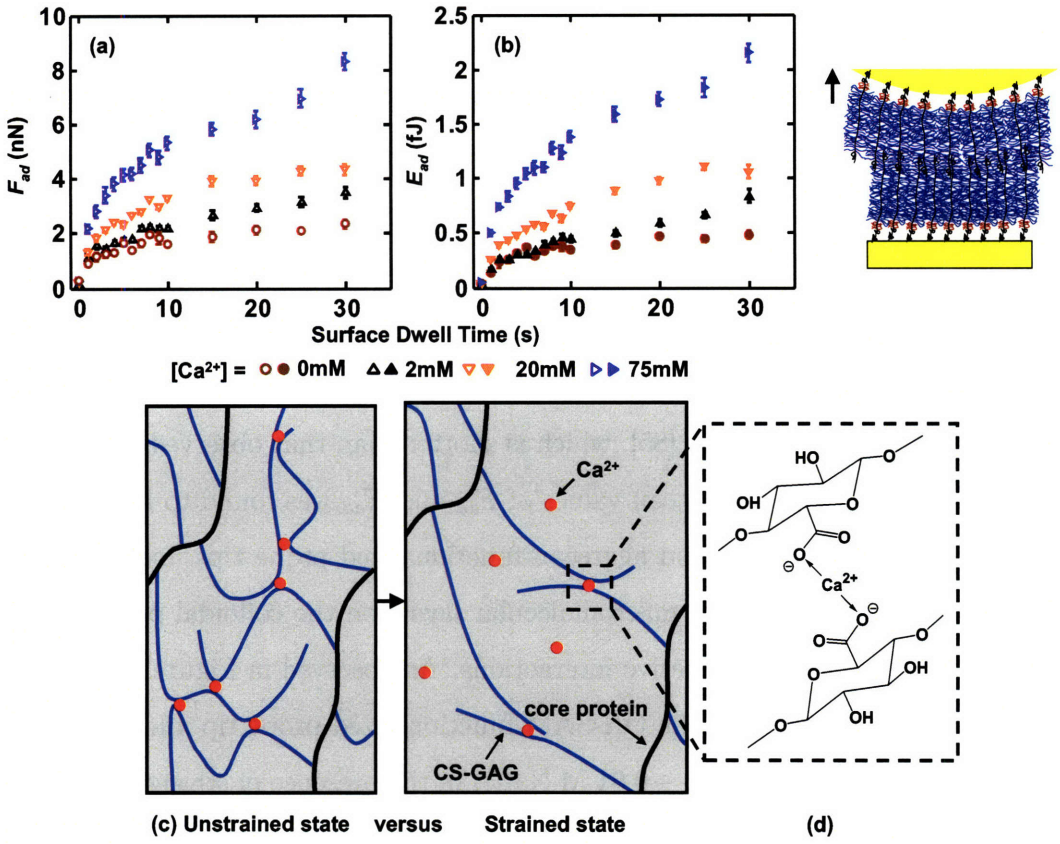

Figure 5-4: (a) Maximum adhesion forces F_{ad} (open symbols) and (b) total adhesion energy E_{ad} (closed symbols) as a function of surface dwell time t between two opposing aggrecan layers in NaCl + $CaCl_2$ solutions, $[Cl^-] = 0.15$ M at varying $[Ca^{2+}]$ concentration, pH ~ 5.6 ($z \sim 4$ μm/s, $F_{max} \sim 45$ nN; mean $\pm$ SEM, $n \geq 30$ for each surface dwell time t at each IS). Statistically significant differences were observed for F_{ad} and E_{ad} at different different $[Ca^{2+}]$ (two-way ANOVA test, $p < 0.0001$). (c) Schematic of aggrecan self-adhesion due to Ca^{2+}-mediated ion-bridging, and energy dissipation of the Ca^{2+}-ion-bridges upon mechanical elongation of GAG side chains upon loading (not drawn on scale). (d) Schematic of one possible $[Ca^{2+}]$-mediated ion-bridging mechanism between CS-GAGs via the carboxyl groups.

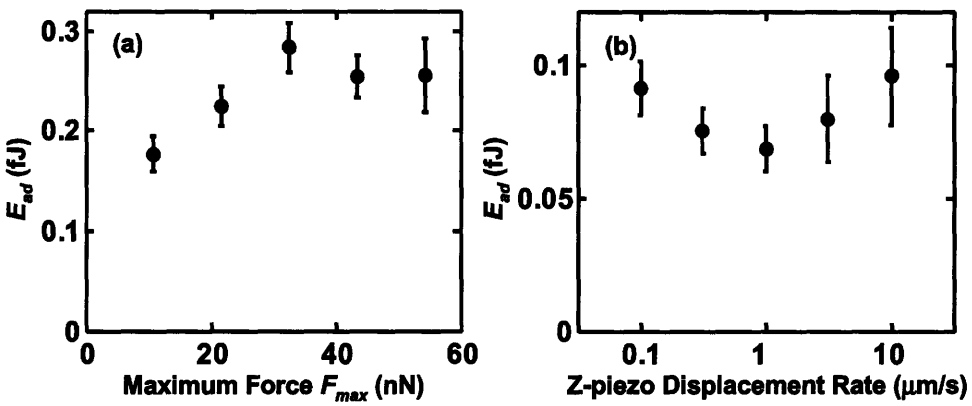

Figure 5-5: Total adhesion energy E_{ad} as a function of (a) maximum compressive force F_{max} and (b) z-piezo displacement rate between two opposing aggrecan layers in 0.1 M NaCl, pH $\sim$ 5.6 (For (a) $t = 5$ s, $z \sim 4$ μm/s; mean $\pm$ SEM, $n \geq 30$ for each F_{max}, one-way ANOVA $p > 0.05$; (b) $t = 1$ s, $F_{max} = 45$ nN; mean $\pm$ SEM, $n \geq 30$ for each z, one-way ANOVA $p > 0.05$). The trends observed at other ionic strengths are similar.

the GAG side chains [95, 78] and the core protein [131] from two opposing aggrecan molecules, Figure 5-4d. This Ca^{2+}-mediated binding mechanism is also known to occur between other biological molecules. For example, the carbohydrate-carbohydrate interactions between trisaccharide Lewis X is relevant to cell-cell adhesion [24], and the adhesion between type I collagen and other noncollagenous biomacromolecules (e.g. osteopontin) in bone is an essential contributor to the mechanical properties of bone [44]. Even a small amount of Ca^{2+} ($[Ca^{2+}] \sim 1 - 2\%$ of $[Na^{+}]$) can lead to large energy dissipation [44] upon mechanical deformation induced molecular strain of the aggrecan network (Figure 5-4c) corresponding to physiological range ($\sim$ 70% increase in E_{ad} at 2 mM, Figure 5-4b). Besides affecting self-adhesion of aggrecan, here, the presence of Ca^{2+} directly changes aggrecan compressive and shear properties by neutralizing the negative charges along GAG side chains [63].

There was no significant effect of maximum compressive force F_{max} in the range of $\sim 10 - 60$ nN (corresponding to the molecular conformation of aggrecan *in vivo* [28]) on the measured adhesion energy for both the OH-SAM functionalized (data not shown) and aggrecan functionalized colloidal probe tips (Figure 5-5a). The loading-

unloading z-piezo displacement rate ($0.1 - 10$ μm/s) also did not significantly affect the measured adhesion energy (Figure 5-5b), suggesting that aggrecan behaves in an elastic-like (non-rate dependent) manner in this range of loading rates, consistent with previous measurement of aggrecan compressive properties in the same range of displacement rates [28]. This negligible dependence of adhesion on displacement rate suggests that the applied unloading rates ($\sim 0.5 - 50$ pN/s per pair of aggrecan) are within the range of quasi-equilibrium conditions. In the unloading rate range far from equilibrium, rupture forces measured in interaction force experiments depend logarithmically on loading rates [40, 102], as observed in other similar systems that test the binding forces between single or a few biological molecules, such as hyaluronan versus hyaluronan binding protein [94], and biotin versus streptavidin [102]. Independence of unloading rate has been observed for other molecules in which the experiments were carried out under quasi-equilibrium conditions [171, 3, 168, 134] (e.g., unbinding of ureido-4[1H]-pyrimidinone dimmers $(UPy)_2$ in hexadecane at 330K at $\sim 10^4 - 10^5$ pN/s unloading rate [171] and 6-ferrocenylhexanethiol (C6Fc) and thiol-functionalized 2-mercaptoethanol (C2OH) in Milli-Q water at $\sim 10^3 - 10^6$ pN/s [168]). The z-piezo displacement rates used in the present study ($0.1 - 10$ μm/s) correspond to the range consistent with known quasi-equilibrium macroscopic behavior of cartilage [28], suggesting that aggrecan self-adhesion can occur within cartilage under quasi-equilibrium conditions.

Our experimental setup was designed to be as close as possible to physiological conditions; the 2-dimensional chemical end-grafting of aggrecan onto a planar gold surface simulates the 3-dimensional binding of aggrecan to hyaluronan via its G1 domain, the corresponding strain and aggrecan packing density at $F_{max} \sim 10 - 60$ nN are consistent with aggrecan molecular concentration *in vivo* [28], the loading-unloading rate ($0.1 - 10$ μm/s, or $\sim 10 - 1000$ ms) covers the time scale of joint loading (within $10 - 150$ ms) [139], and the aqueous solution (IS = 0.15 M, $[Ca^{2+}]$ = 2 mM) mimics *in vivo* ion concentrations (IS = 0.15 M, $[Ca^{2+}] \sim 2 - 4$ mM) [99]. The self-adhesion forces, F_{ad}, and energies, E_{ad}, reported in this study, which involved large, well-defined assemblies of $\sim 10^3$ aggrecan macromolecules, were highly

repeatable (as indicated by the relatively low standard error values, Figures 5-3 – 5-5) and did not have the additional complexities that need to be considered in single molecule binding measurements, such as nonspecific surface interactions, multi-bridging macromolecules, and the effect of molecular linkers [164]. To summarize, we have discovered that two opposing aggrecan layers, when compressed together for a sufficient amount of time (seconds), can undergo self-adhesion (up to 5 nN forces or ± 1 pN per aggrecan pair) which enables the extension of the macromolecular chains and, correspondingly, a large energy dissipation (up to 1.5 fJ) even in the presence of strong electrostatic double layer repulsion. Aggrecan self-adhesion was found to be highly dependent on the time of compression ($0 - 30$ s), as well as [NaCl] $= 0.001 - 1$ M and [Ca^{2+}] $= 0 - 75$ mM concentrations, but independent of the displacement rate ($0.1 - 10$ μm/s) and compressive load ($10 - 60$ nN) in the ranges tested. Our results are consistent with the known characteristics of other carbohydrate - carbohydrate interactions, time-dependent formation of interactions, and a strong dependency on divalent cations [Ca^{2+}] [123, 69]. Aggrecan self-adhesion may have both chemical (e.g., van der Waals, H-bonding) and physical (i.e. molecular entanglements) contributions. In the presence of Ca^{2+} (also present *in vivo*), ion-bridging could be another important factor that contributes to self-adhesion.

The estimated average binding force between one pair of opposing aggrecan at IS $= 0.15$ M, [Ca^{2+}] $= 2$ mM (Figure 5-4a), is ~ 1 pN; however, since adhesion may only occur between a fraction of the total aggrecan ensemble, this value should be taken as a lower limit. It should be noted that the estimated aggrecan-aggrecan ~ 1 pN binding force is much weaker compared to experimentally measured single molecule binding forces involving other ECM proteoglycans, e.g., hyaluronan/aggrecan G1 core protein domain (40 ± 11 pN) [94], decorin/decorin (16.5 ± 5.1 pN), type IX collagen/biglycan (~ 15 pN) [19], type I collagen/decorin (core protein) (54.5 ± 20 pN), and type I collagen/decorin (GAG side chain) (31.9 ± 12.4 pN) [167]. Two differences between these experiments measuring single- or double-molecular interactions and the data presented here on adhesion between two opposing aggrecan are as follows: firstly, aggrecan-aggrecan intermolecular interactions within each of the layers could affect

local binding interactions; secondly, the maximum compressive load for a single pair of aggrecan monomers within the densely packed layers is much less than the single molecular interactions on lower grafting density surfaces.

5.4 Conclusions

Based on these experimental results, we propose a new hypothesis that aggrecan self-adhesion and the resulting energy dissipation could be an important factor contributing to the self-assembled architecture and integrity of the cartilage ECM *in vivo*. Even though the magnitude of the self-adhesion forces is at least an order of magnitude smaller than the repulsive forces arising from the electrostatic double layers between aggrecan GAGs, the multiplicity of interactions existing within the aggrecan moiety would result in a large reservoir for energy dissipation through the rupture of reversible self-adhesion interactions [44], and hence, could protect the fine collagen meshwork upon repeated joint loading or impact. This hypothesis is supported by the self-assembly of glyconanoparticles *in vitro* due to similar carbohydrate-carbohydrate interactions [25]. Additionally, adhesive interactions between ECMs constituents are critical for ECM assembly and play essential roles in overall tissue organization and the proper tissue physiological function [59]. For example, the reversible sacrificial bonding of osteopontin in bone is thought to act as an adhesive layer between the mineralized collagen fibrils and to be responsible for significant amounts of tensile strength at specific locations [43]. It is known that aggrecan can bind to other ECM macromolecules, for example, to hyaluronan via its G1 domain in the presence of link protein, which is essential for the construction of the proteoglycan aggregate motif *in vivo* [66, 74]. Aggrecan also interacts with type II collagen fibrils via its keratin sulfate GAG chains, which is thought to contribute to the structural integrity of the aggrecan aggregate [73]. In addition, aggrecan can bind to fibulin-2 via the C-type lectin in its G3 domain [115], and the CD44 protein on the cartilage chondrocyte cell via its GAG chains in the presence of Ca^{2+} to stimulate specific biological interactions [52].

Chapter 6

Time-Dependent Cartilage Nanomechanics and the Relation to the Nanostructure of its Type II Collagen Network

6.1 Introduction

Articular cartilage is a dynamic biological tissue composed of two major components, aggrecan and collagen, that serves as a load-bearing material in the joint. Cartilage is known to exhibit poroelastic behavior at the tissue level, and the solid matrix of cartilage also exhibits intrinsic viscoelastic properties [97]. Previous nanoindentation studies on cartilage have focused on the effect of enzymatic digestion [143], osteoarthritis [86] and tissue repair [32] on cartilage nanoscale mechanical properties. Other nanomechanical studies on cartilage ECM components have unveiled the interactions between opposing aggrecan, indicating a critical role of electrostatic interactions from their highly negatively charged GAG branches [28]. The contribution and structure of the collagen II network to the mechanical properties of cartilage is explored in this work. To better understand the molecular mechanisms underlying

the biomechanical behavior of cartilage and its constituent collagen network, here we report the time-dependent nanomechanical behavior of intact and proteoglycan (PG)-depleted cartilage using AFM-based force indentation, force relaxation and dynamic oscillatory experiments. In addition, tapping mode AFM (TM-AFM) imaging was used to study the nanoscale structures of the type II collagen network, obtained by enzymatic digestion of the proteoglycan content of bovine cartilage discs. By isolating the collagen II network in its physiological/original orientation and structure, it was possible to explore its nanostructure and through nanomechanical tests, describe its contribution to the mechanical properties of cartilage. The goal of this work is to relate the molecular structure of the ECM macromolecules to the nanoscale and tissue level properties of cartilage.

6.2 Methods

6.2.1 Cartilage sample preparation

Cartilage disks (9 mm diameter $\times \sim 0.5$ mm thickness) were harvested from the intact surface and middle/deep zone of the femoropatellar groove of $1-2$ weeks old bovine calves by microtoming and maintained in 0.15 M sterile phosphate buffered saline (PBS, without Mg^{2+}, Ca^{2+}). Additional groups of disks from both zones were digested with 1 mg/mL trypsin (0.15 M NaCl, 0.05 M Na_3PO_4, pH $\sim$ 7.2) for 24 hours at 37°C, followed by 0.1 U/mL chondroitinase-ABC (0.15 M NaCl, 0.05 M Tris-HCl, pH $\sim$ 8.0) for 24 hours at 37°C, which resulted in loss of $>$ 95% of matrix proteoglycan (PG), as assessed by dimethylmethylene blue (DMMB) dye binding assay [45], leaving the residual type II collagen network [20]. In a separate study, type I collagen fibrils were extracted from rat tail tendon [56] and digested with trypsin and chondroitinase-ABC as above, to remove PG constituents from the tendon fibril network.

6.2.2 Nanostructure of type II collagen fibrils

Native and proteoglycan-depleted cartilage disks from both the intact surface and middle/deep zone were air-dried overnight. In a separate experiment, calf chondrocytes were seeded in 2% w/v alginate beads ($\sim$ 3 mm diameter). On day 18 of culture, the beads were depolymerized in 55 mM sodium citrate, gently releasing the cells and their newly synthesized PCM. The cells with PCM were absorbed to cleaved mica, dried in ambient conditions. Both samples were imaged via tapping mode in air with a Nanoscope IIIA Multimode AFM (Veeco, Santa Barbara, CA) using Olympus AC240TS-2 rectangular silicon cantilevers ($R < 10$ nm, nominal spring constant $k \sim$ 2 N/m). Type I collagen fibrils from rat tail tendon was deposited on an atomically flat mica surface and dried overnight, and imaged via the same probe tip as the control to distinguish different structural features between type I collagen fibrils and type II collagen fibrils from bovine cartilage. Images from cartilage and rat tail tendon were processed via Fast Fourier Transform (FFT) to quantify their banding patterns.

6.2.3 Cartilage nanoindentation and time-dependent nanomechanics

AFM-based nanoindentation was carried out on both the untreated and PG-depleted disks from the middle/deep zone at a maximum load $\sim$ 70 nN in 0.15 M PBS using a Nanoscope IV AFM with a PicoForce piezo in the force-displacement mode (Veeco, Santa Barbra, CA) in a given range of AFM piezo-displacement rates ($0.1-10$ μm/s). As the PicoFoce piezo is close-looped in z-direction, the exact position of z-piezo and cantilever deflection could be captured, enabling the quantification of indentation force curves. Both standard nanosized pyramidal AFM probe tips (end radius $R \sim 50$ nm, NP tip D, silicon nitride, V-shaped cantilever, nominal spring constant $k \sim$ 0.58 N/m, Veeco, Santa Barbara, CA) and microsized spherical colloidal probe tips ($R \sim 2.5$ μm, $k \sim 0.58$ N/m, Bioforce Nanosciences, Ames, IA) were used. Both were coated with 2 nm Cr and 50 nm Au, and then functionalized with a neutral hydroxyl-terminated self-assembled monolayer (OH-SAM) by immersion in 3 mM

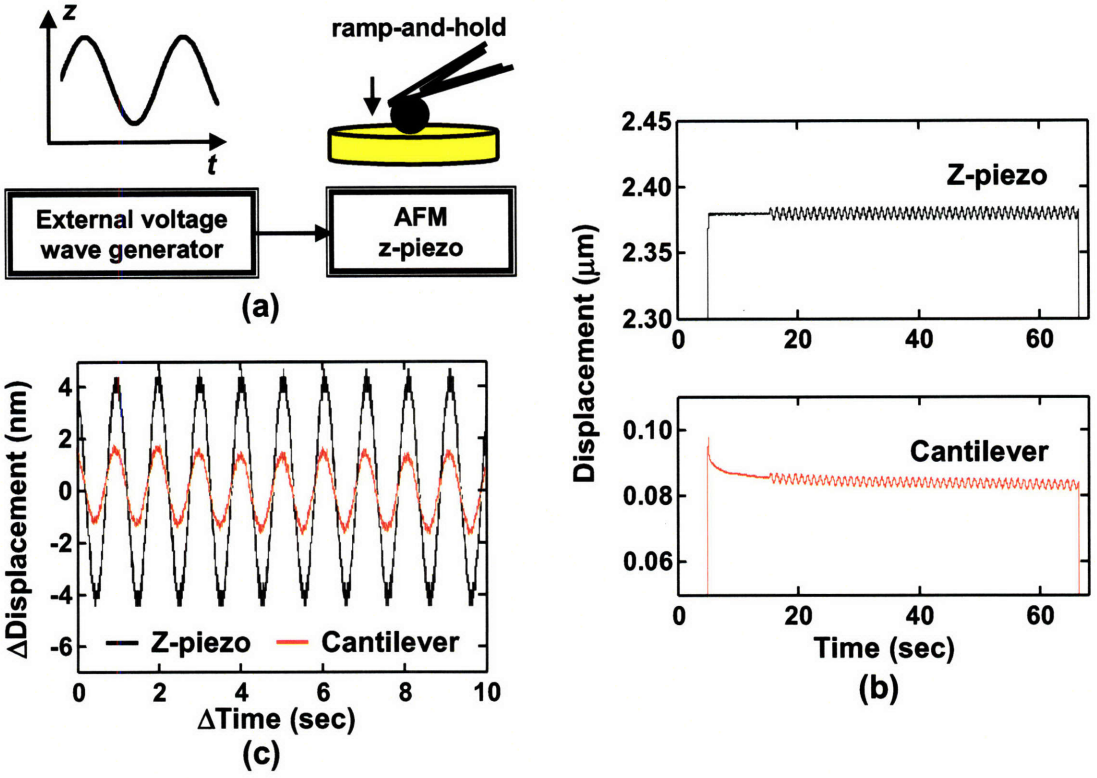

Figure 6-1: (a) Schematic of experimental set-up on dynamic loading during ramp-and-hold stress relaxation experiment on cartilage disks. (b) One pair of z-piezo and cantilever displacement curves as a function of time during ramp-and-hold and dynamic loading at 1 Hz applied frequency and $\sim$ 4 nm z-piezo oscillation amplitude on untreated cartilage sample using an OH-SAM functionalized colloidal probe tip. (c) One random sampling of z-piezo and cantilever dynamic deformation data from data shown in panel (b) in the range of steady state time scope ($t_0 \sim 35-50$ seconds).

$HS(CH_2)_{11}OH$ ethanol solution for 24 hours to eliminate electrostatic interactions arisen from probe tip surface. On each sample, at least 6 different locations were indented, and 10 different curves were obtained at each location at a given z-piezo displacement rate (0.1, 1, and 10 μm/s).

A ramp-and-hold tip stress-relaxation experiment was performed in the script mode of the Nanoscope IV AFM. The probe tip was programmed to move towards the surface at a given constant z-piezo displacement rate for $\sim 2-2.5$ μm, and was hold for 60 seconds before unloaded from the sample. The z-piezo displacement and

cantilever deflection were recorded as a function of time from $2-3$ seconds before the start of loading until ~ 1 second after unloading. As the z-piezo is not close-looped in the script mode, a force-indentation was performed at a maximum given load ~ 85 nN (indentation depth $\sim 1-1.5$ μm for untreated disk and $\sim 1.5-2$ μm for PG-depleted disk) immediately before each of the ramp-and-hold experiment to keep the maximum indentation force approximately constant.

An external sinusoidal electronic function generator was connected to the Pico-Force piezo controller to enable the z-piezo movement in a sinusoidal fashion (Figure 6-1a). For each of the tested frequencies ($1-1000$ Hz) and cartilage deformation amplitudes ($\sim 2-50$ nm, corresponding to $\sim 4-120$ nm of z-piezo displacement), dynamic oscillatory deformation of the z-piezo was enabled after $10-15$ seconds of loading during one ramp-and-hold experiment. Before applying to cartilage disks, this system was calibrated by applying to a hard mica surface at the same frequencies and amplitudes, as the control experiment to correct the system errors, which was discussed in details in Appendix F. For each cartilage sample, the experiment was performed on at least 6 different positions.

6.3 Data Analysis

6.3.1 Nanoindentation

First, the average of cantilever deflection (V) and z-piezo displacement (nm) was calculated for the ten force-displacement curves collected at each z-piezo displacement rate and indentation position. The contact point of the probe tip and was determined by the position where the cantilever deflection signal exceeds five times the noise level (the standard deviation) of deflection signals in the noncontact region. The indentation depth was then calculated as the z-piezo displacement (nm) minus the cantilever deflection (nm) with respect to the values at the contact point. Hertz model has been widely used to estimate the dynamic material elastic modulus upon indentation, for the spherical colloidal probe tip with end-radius $R \sim 2.5$ μm on the

flat cartilage sample with thickness $h >> R$,

$$F = \frac{4}{3}\frac{E}{(1-\nu^2)}R^{1/2}D^{3/2} \tag{6.1}$$

where F is the indentation force, D the indentation depth, ν the Poisson ratio of the cartilage sample ($\nu = 0.1$ for the bovine cartilage [97]) and E the calculated elastic modulus of cartilage disk. As the modulus of cartilage is highly nonlinear, especially in the indentation depth range < 500 nm, the force-indentation curves were fit in the upper 75% percent region of the loading curve with modified Hertz model, or the power-law equation [116],

$$F = \frac{4}{3}\frac{E}{(1-\nu^2)}R^{1/2}(D-D_f)^{3/2} \tag{6.2}$$

where D_f is the offset position where the good fit of Hertz model on the experimental data was achieved via least squares nonlinear regression. Similar fitting was performed on the force-indentation curves data achieved via the pyramidal nanosized probe tip ($R \sim 50$ nm, tilted angle $\alpha \sim 35°$) [116],

$$F = \frac{\pi}{2}\frac{E}{(1-\nu^2)}\tan\alpha(D-D_f)^2 \tag{6.3}$$

The mean and standard error of mean values of effective stiffness E were calculated from the fit at different positions for both the untreated and PG-depleted disks.

6.3.2 Ramp-and-hold stress relaxation

For each pair of the ramp-and-hold stress relaxation time series data, the data corresponding to the loading (ramp) part was first analyzed in the same fashion as the nanoindentation data to calculate the indentation depth and elastic effective stiffness. The 60-second holding (stress-relaxation) part was then fit with the modified Hertz model adding the 3-element spring and dashpot viscoelastic component using the

spherical probe tip [22],

$$F = \frac{4}{3}\frac{E}{(1-\nu^2)}R^{1/2}(D-D_f)^{3/2}(1+\frac{\tau_\sigma-\tau_\epsilon}{\tau_\epsilon}\exp-\frac{t}{\tau_\epsilon}) \tag{6.4}$$

where τ_ϵ and τ_σ are the relaxation time constant under constant deformation and loading, respectively. The data from the first second after loading was excluded from the fit. The same fitting process was applied to the data obtained via the pyramidal probe tip to calculate the relaxation time constants,

$$F = \frac{\pi}{2}\frac{E}{(1-\nu^2)}\tan\alpha(D-D_f)^2(1+\frac{\tau_\sigma-\tau_\epsilon}{\tau_\epsilon}\exp-\frac{t}{\tau_\epsilon}) \tag{6.5}$$

effective stiffness and relaxation time constants were estimated via the fit.

6.3.3 Oscillatory dynamic loading

Similar to the ramp-and-hold stress relaxation data, for each pair of the oscillatory dynamic loading time series data at a given z-piezo deformation amplitude and frequency, the data corresponding to the loading (ramp) part was first analyzed in the same fashion as the nanoindentation data to calculate the indentation depth and elastic effective stiffness. The time region corresponding to the steady-state dynamic loading was then randomly sampled for 100 times (Figure 6-1b, c). Upon each sampling, the amplitude and phase lag between the sinusoidal waves of oscillatory force $\widetilde{F}$ and cartilage deformation $\widetilde{D}$ were calculated (for details, see Appendix F). To calculate the dynamic oscillatory modulus, extended model was obtained by expanding the Hertz model in the indentation depth D by a Taylor series [96],

$$F \approx \frac{4}{3}R^{1/2}(\frac{E_0}{(1-\nu^2)}D^{3/2}+\frac{3}{2}\frac{E_1}{(1-\nu^2)}D^{1/2}\widetilde{D}) \tag{6.6}$$

where E_0 and E_1 are the effective stiffness with respect to the zeroth and first order expansion of the Taylor series, the higher ordered term was neglected as the oscillatory deformation amplitude $\widetilde{D}$ is several orders of magnitude smaller than the indentation depth D. Hence, the oscillatory dynamic modulus E_1 was calculated from

the oscillatory part of the force and deformation data,

$$\widetilde{F} \approx 2\frac{E_1}{(1-\nu^2)}R^{1/2}D^{1/2}\widetilde{D} \tag{6.7}$$

The same criteria was applied for the data achieved via the pyramidal probe tip,

$$\widetilde{F} \approx \pi\frac{E_1}{(1-\nu^2)}D\widetilde{D}\tan\alpha \tag{6.8}$$

6.4 Results

6.4.1 Collagen network nanostructure

The air-drying process resulted in a collapse of the cartilage solid collagen network, hence the pore size and porosity of this scaffold *in vivo* could not be tested via the tapping mode AFM imaging technique in air. However, the dehydration does not change the inner structural features of the solid collagen fibrils, e.g. the fibril diameter, hence the high resolution AFM imaging would provide valid information on the nanostructural features of the type II collagen fibrils. Tapping mode images of air-dried untreated cartilage in air did not yield clear characteristic nanostructures due to the presence of both the proteoglycan (PG) constituents and the collagen fibrils (Figure 6-2a). Enzymatic treatment with trypsin and chondroitinase-ABC revealed collagen fibrils randomly oriented in the image plane of intact superficial zone and middle zone disks, with fibril diameters $\sim 80 \pm 8$ nm (Figure 6-2b, c), consistent with previous reports on cartilage ultrastructure [109]. Different collagen alignment was observed from the disks obtained from the cartilage intact surface and middle/deep zone. As the collagen fibrils are randomly aligned in the three dimensions in the middle/deep zone, and the microtoming sample preparation has trimmed the cartilage fibrils (Figure 6-2b), the fibrils are randomly aligned in the two-dimensional-plane of the cartilage surface (Figure 6-2c). The same banding structures are clearly observed on both disks. Fourier transforms of the AFM images revealed a distinct $\sim$ 23 nm periodic banding substructure within these type II fibrils from cartilage (Figure 6-

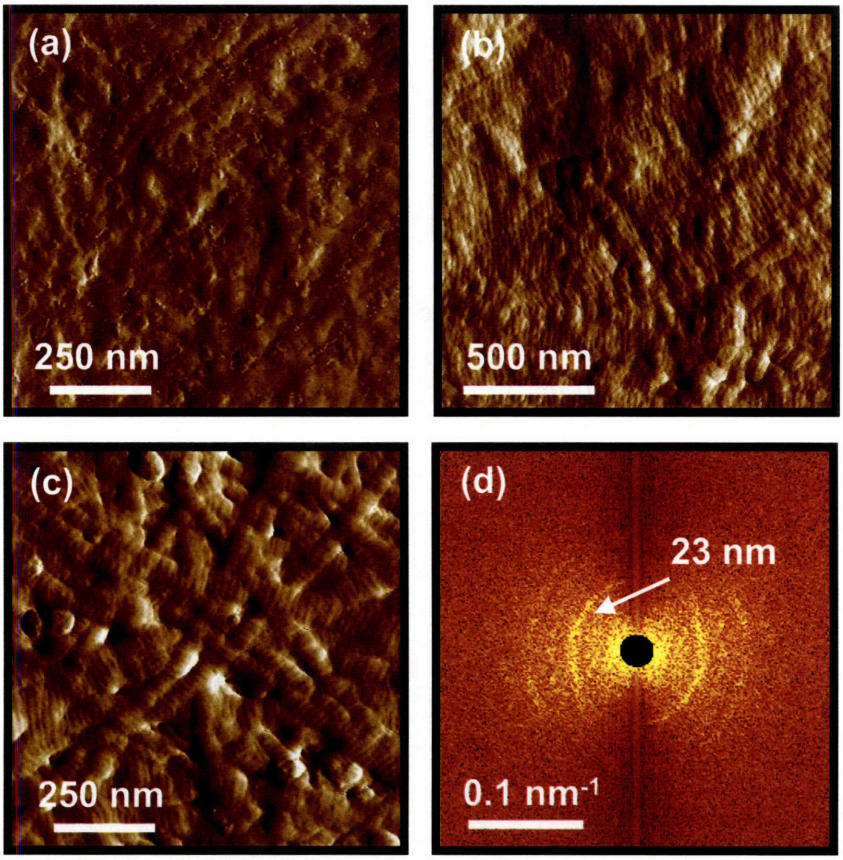

Figure 6-2: Tapping mode AFM amplitude images of (a) untreated cartilage disk from middle/deep zone, (b) PG-depleted cartilage disk from the intact cartilage surface, (c)PG-depleted cartilage disk from middle/deep zone, the disks were dried in air before imaging via a shape silicon probe tip ($R < 10$ nm, $k \sim 2$ N/m, Olympus) in air. (d) Fast Fourier Transform (FFT) of image (b).

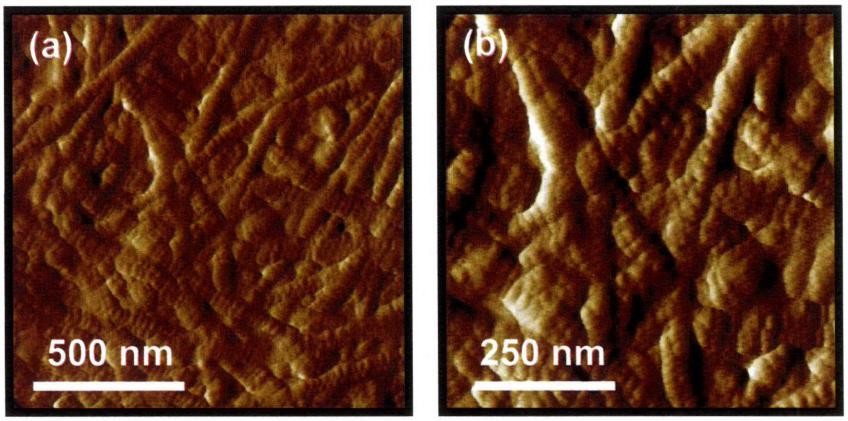

Figure 6-3: Tapping mode AFM amplitude images of type II collagen fibrils developed in chondrocyte pericellular matrix (PCM) *in vitro*, the disks were dried in air before imaging via a shape silicon probe tip ($R < 10$ nm, $k \sim 2$ N/m, Olympus) in air.

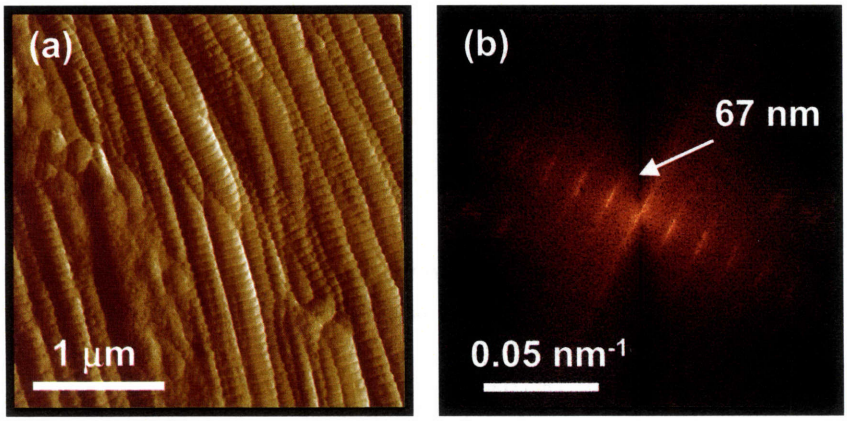

Figure 6-4: (a) Tapping mode AFM amplitude images of PG-depleted type I collagen fibrils from rat tail tendon. The fibrils was deposited on a flat mica substrate and dried in air before imaging via a sharp silicon probe tip ($R < 10$ nm, $k \sim 2$ N/m, Olympus) in air. (b) FFT of image (a).

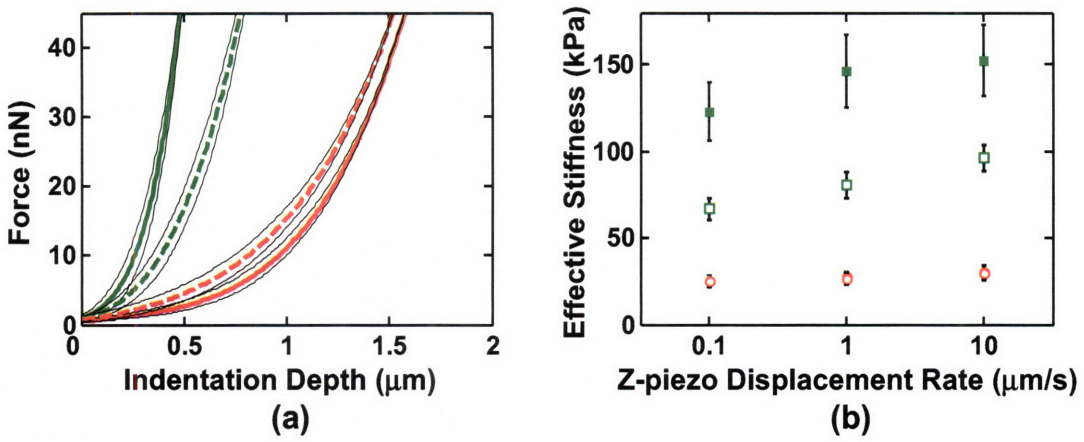

Figure 6-5: (a) Force versus indentation depth curves using the OH-SAM functionalized colloidal (solid lines, $R \sim 2.5$ μm, $k \sim 0.58$ N/m) and pyramidal (dashed lines, $R \sim 50$ nm, $k \sim 0.58$ N/m) tips on untreated (green) and PG-depleted (red) middle/deep zone cartilage disks, mean $\pm$ SEM, $n \geq 6$ different positions. (b) Estimated effective stiffness of untreated (squares) and PG-depleted (circles) cartilage disks via Hertz model from force-indentation depth curves obtained in panel (a) using the spherical (closed symbols) and pyramidal (open symbols) tips, mean $\pm$ SEM, $n \geq 6$ different positions.

2d), which was also was clearly observed on newly synthesized cartilage pericellular matrix type II collagen fibrils by calf knee chondrocytes *in vitro*, Figure 6-3, [111]. In contrast, the predominant banding observed in rat tail tendon type I collagen fibrils is ~ 67 nm (Figure 6-4), consistent with the well-known D-banding pattern [133]. As the 67 nm D-banding pattern could be clearly observed via the same AFM imaging technique on the proteoglycan depleted type I collagen fibrils (Figure 6-4), this 23 nm banding is not an artifact by the imaging process or proteoglycan depletion.

6.4.2 Cartilage nanoindentation and ramp-and-hold stress relaxation

Nonlinear indentation behavior was observed for both untreated and PG-depleted cartilage disks (Figure 6-5a), consistent with previous studies on cartilage nanoindentation [143, 86] and compressive nanomechanics of aggrecan layers [28]. However, the Hertz model fit within the top 75% of all the indentation force curves yielded

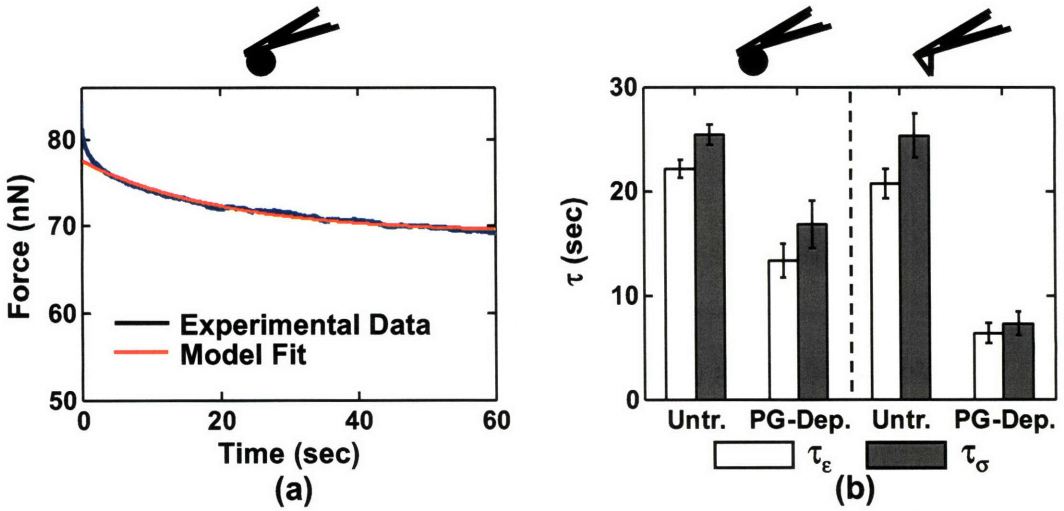

Figure 6-6: (a) Illustration of one stress-relaxation force curve obtained via OH-SAM functionalized colloidal probe tip on untreated cartilage sample and the fit using 3-element model with one relaxation time constant by least squares nonlinear regression. (b) Estimated stress relaxation constants under constant deformation τ_ϵ and load τ_σ, for both untreated and PG-depleted cartilage disks using OH-SAM functionalized colloidal and pyramidal probe tips via 3-element stress-relaxation viscoelasticity model, mean $\pm$ SEM, $n \geq 6$ different positions.

good fit ($R^2 > 0.98$), suggesting the linear (constant effective stiffness) deformation behavior in this applied force range. The effective stiffness, calculated using the Hertz model [84], yielded $E = 146 \pm 20$ kPa for untreated, and $E = 28 \pm 3$ kPa for PG-depleted tissue via the colloidal probe tip at 1 μm/s z-piezo displacement rate, Figure 6-5b. Significant lower modulus was observed on the untreated disk measured by the pyramidal probe tip ($E = 81 \pm 8$ kPa) compared to the colloidal probe tip (two-way ANOVA, $p < 0.0001$), while there is no significant difference observed on the PG-depleted disk with these two probe tips ($E = 27 \pm 3$ kPa for pyramidal tip, two-way ANOVA, $p > 0.05$). Significant increases of effective stiffness while increasing the z-piezo displacement rate ($0.1 - 10$ μm/s) was observed for both the untreated and PG-depleted disks measured via both probe tips (nonparametric Friedman's test, $p < 0.05$), although the magnitude of increase is smaller than the variation due to the different indentation positions.

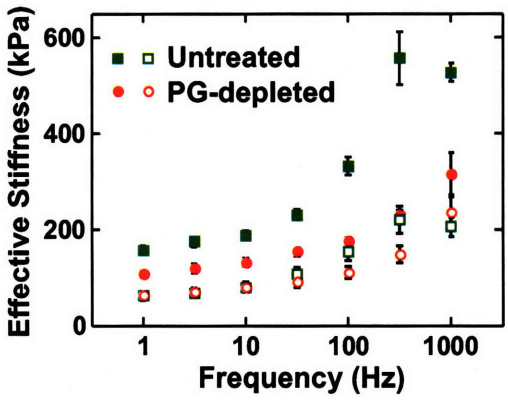

Figure 6-7: Estimated effective stiffness of untreated (squares) and PG-depleted (circles) cartilage disks (thickness ~ 0.5 mm) measured via the OH-SAM functionalized colloidal (closed symbols, $R \sim 2.5$ μm, $k \sim 0.58$ N/m) and standard nanosized pyramidal probe tip (open symbols, $R \sim 50$ nm, $k \sim 0.58$ N/m) as a function of deformation frequency ($1 - 1000$ Hz) at ~ 2 nm deformation amplitude, estimated via Hertz model [96], mean $\pm$ SEM, $n \geq 6$ different positions.

Time-dependent poro-viscoelastic behavior was observed for both disks, as continuously decrease of force was observed during the 60-second holding process, Figure 6-6a. The 3-element viscoelastic model predicts good fit for the time $t > 1$ second after loading. For $0 < t < 1$ second, a good fit ($R^2 > 0.95$ for all the data) could be achieved by introducing an additional time relaxation constant via a 5-element viscoelastic model, during which case, the faster relaxation time constant is ~ 1 second, and most of the fitting errors are within first second after loading (data not shown). These results suggest the spring-dashpot viscoelastic models predict the stress-relaxation behavior of cartilage well in the longer time scope (> 1 second), but not in the short time scope. Significant drop of the relaxation time constant was observed after PG-depletion, measured by both the spherical and pyramidal probe tips (Figure 6-6b). For the untreated cartilage disk, the pyramidal tip yielded no significant difference of relaxation time constant (20.7 ± 1.4 sec) compared to the spherical tip (22.1 ± 0.9 sec) for the untreated cartilage; a more marked effect was observed for the PG-depleted cartilage, as a more than 50% decrease in the relaxation time constant was measured when using the pyramidal tip, Figure 6-6b.

6.4.3 Cartilage dynamic oscillatory nanomechanics

At $\sim$ 2 nm deformation amplitude, a significant increase in dynamic stiffness was observed for the untreated cartilage disk as deformation frequency increases from 1 Hz to 316 Hz, using both the spherical and pyramidal probe tips; the stiffness measured at 1000 Hz is not significantly different from that measured at 316 Hz. By comparison, a continuous increase in stiffness was measured for the PG-depleted disk up to 1000 Hz using both probe tips, Figure 6-7. PG-depletion resulted in a decrease in stiffness measured by the spherical probe tip at all tested frequencies, Figure 6-7a, consistent with the nanoindentation, ramp-and-hold experiment and other tissue-level studies [99]. Interestingly, there is no significant difference between the stiffness measured on the untreated and PG-depleted disks at $1 - 31.6$ Hz and 1000 Hz, and the stiffness is higher for the untreated cartilage at 100 and 316 Hz measured by the pyramidal probe tip, Figure 6-7b. For both disks, similar continuous increase of the phase lag between deformation and force as increasing deformation frequency was observed via both probe tips, suggesting the increasing importance of energy-dissipative deformation mechanisms at higher frequencies, Figure 6-8.

The dynamic oscillatory deformation was tested at different deformation amplitudes ($\sim$ 2 to $\sim$ 50 nm) up to 100 Hz. Using both probe tips, the same increase trend in stiffness on frequency was observed for both disks. There is no significant difference in stiffness measured at different deformation amplitudes at the same frequency for the untreated cartilage, tested by both probe tips. A significant drop in stiffness was observed for the PG-depleted disk at larger amplitude ($\sim$ 50 nm), also tested by both probe tips, and the drop is more marked when measured by the spherical probe tip, Figure 6-9. Similar trends were observed for the phase lag dependence, as increasing frequency resulted in an increase in the phase lag for both disks. No significant difference in the phase angle was observed for the untreated cartilage at the same frequency, and the phase lag was higher when deforming at larger amplitude for the PG-depleted cartilage, also tested by both probe tips, Figure 6-10.

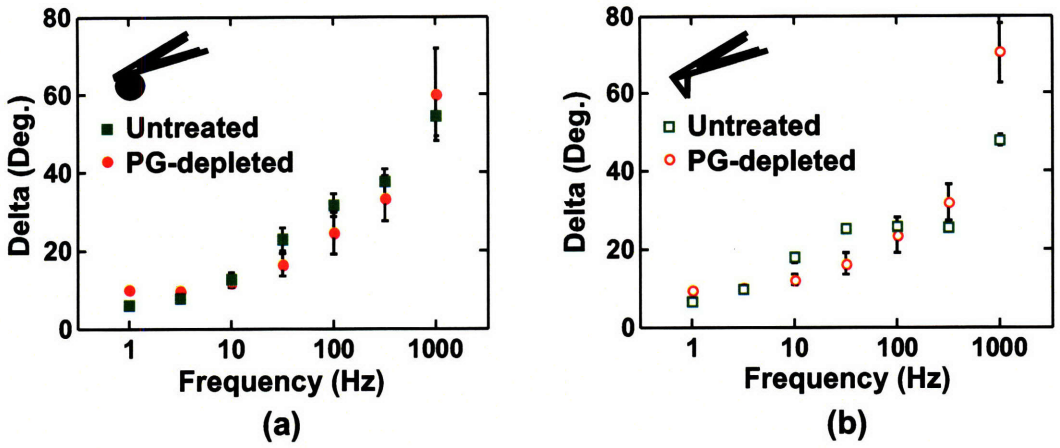

Figure 6-8: Estimated phase lag of deformation with respect to applied force of untreated (squares) and PG-depleted (circles) cartilage disks (thickness $\sim$ 0.5 mm) measured via the OH-SAM functionalized (a) colloidal probe tip (closed symbols, $R \sim 2.5$ μm, $k \sim 0.58$ N/m) and (b) standard nanosized pyramidal probe tip (open symbols, $R \sim 50$ nm, $k \sim 0.58$ N/m) as a function of deformation frequency ($1-1000$ Hz) at $\sim$ 2 nm deformation amplitude, mean $\pm$ SEM, $n \geq 6$ different positions.

6.5 Discussion

6.5.1 Type II collagen network banding pattern

The predominant 67 nm periodical D-banding pattern found in type I collagen fibrils was suggested as the staggering packing of the heterometric triple collagen helices [133] due to the hydrophobic and electrostatic interactions along the amino acid sequences [104]. Similar 67 nm D-banding pattern was found in type II collagen fibrils from human [58] and bovine [7] intervertebral discs, as well as human costal cartilage [10] via low angle X-ray diffraction, supported by the modeling on interactions along the type II collagen amino acid sequence [118]. However, a number of studies have detected the 23 nm banding patterns in type II collagen fibrils, which was observed in electron micrographs of both embryonic tissues [161] and lamprey notochord sheath [36], as well as the predentin fibrils via transmission electron microscopy [5]. Besides, tapping mode AFM imaging on type I collagen fibrils from rat tail tendon also observed this pattern, though $< 3\%$ compared to the dominating 67 nm D-banding

periodicity [158]. As the collagen fibrils in cartilage are heterofibrils that also contain lesser type IX and XI besides type II collagen, with the proteoglycan moiety surrounded [41]. The interactions between the collagen fibrils and proteoglycan, though not exactly known, could be a factor that contributes to the formation of the 23 nm banding structure [5]. As the 23 nm banding is approximately 1/3 of the D-spacing, it was suggested that a three-fold overlay of the D-banding periodicity could lead to the apparent 23 nm periodicity [158]. In addition, X-ray studies clearly showed the existence of the D-banding pattern in type II collagen fibrils, and the 23 nm banding was argued as a "pseudo-periodicity", which represents $\sim 1/3$ of the D-banding (possibly the overlap zone) . Though it remains unclear the exact structural details of the 23 nm banding and its molecular origins, this structural feature could be a factor that contribute to the structural integrity of cartilage extracellular matrix by interacting and entrapping the proteoglycan within its network.

6.5.2 Comparison to other cartilage tissue-level and nanoscale studies

The measured elastic modulus is approximately on the same order as the tissue-level indentation using millimeter-sized clinical indenters on bovine cartilage [143, 86, 1, 145, 139]. For example, Aspden et al. [1] measured the stiffness for bovine knee cartilage of $0.58 - 1.63$ MPa. Other experiments performed on human cartilage yielded higher stiffness: Swanepoel et al. [145] determined the stiffness of healthy human lumbar apophyseal cartilage of 2.8 MPa, Shepherd et al. [139] reported the compressive elastic modulus of human articular knee cartilage under physiological loading rates of $4.4 - 27$ MPa, etc., which is due to the different material properties of cartilage from different species. Other indentation studies using microscale spherical and nanoscale pyramidal probe tips have yielded similar results. Stolz et al. [143] reported a 100-fold modulus difference measured on porcine articular cartilage using spherical (2.6 MPa) and pyramidal (0.021 MPa) tips, and attributed this difference to the heterogeneity of cartilage ultrastructure. Kilger et al. [86] compared the stiffness

measured on both healthy (46.8 ± 5.8 kPa) and osteoarthritic (22.7 ± 1.6 kPa) human cartilage, and observed the same trend of mechanical deterioration upon enzymatic digestion. Interestingly, when the proteoglycan motif is fragmented by cathepsin D but remained in the collagen network, no significant change of stiffness was observed [143].

6.5.3 Cartilage quasi-static nanomechanics

The magnitude of the measured cartilage stiffness upon PG-depletion via nanoindentation was consistent with previous studies on similar system [86]. As the proteoglycan moiety not only directly contribute to $\sim$ 50% of the compressive stiffness, but protect the deformation of collagen fibrils from local deformation, the depletion of GAG could result in a $>$ 50% drop of the indentation stiffness, as shown in Figure 6-5b. A significant increase in measured stiffness of untreated cartilage (though $<$ 20%) as increasing z-piezo displacement rate from 0.1 to 10 μm/s, Figure 6-5, suggests the presence of both poro/viscoelastic and elastic deformation mechanisms. The same effect was observed on the PG-depleted cartilage sample, Figure 6-5. Comparing to the rate-independent deformation of the 2D densely packed end-grafted aggrecan layer on a planar substrate in the same tested rate range [28], the rate-dependence could be due to the difference conformation of aggrecan in the cartilage disk (end-attached on the hyaluronan and entrapped in collagen network) as well as the molecular frictions between aggrecan and the collagen fibrils. The independence of effective stiffness on probe tips measured on the PG-depleted disk suggests the mechanical properties of the solid type II collagen network does not depend on the deformation geometry. Though the end-radius of the pyramidal probe tip ($R \sim 50$ nm) is on the same order of the collagen fibril diameter, the indentation depth (~ 1 μm) has involved the deformation of fibrils in contact with both the top and sides of the pyramidal tips. As these collagen fibrils form an interconnected network, the deformation induced by both the spherical and pyramidal probe tip are related to the deformation involved an assembly of collagen fibrils on the same micrometer scale, hence resulted in the same stiffness. On the other hand, lower stiffness was observed on the untreated

cartilage via the pyramidal tip, Figure 6-5, for the deformation manner of the proteoglycan moiety could be different under these two tips. As the brush-like aggrecan macromonomers are bind to the hyaluronan and entrapped in the collagen network and have a larger degree of deformation freedom compared to the collagen, penetration of a sharp pyramidal tip could cause splay-like lateral deformation and deplete the aggrecan molecules underneath the probe tip. It is hypothesized that a lower stiffness could be measured due to the lower aggrecan density under the pyramidal tip. This hypothesis is supported by the observation that end-grafted aggrecan layer expresses much higher compressive stiffness under the spherical probe tip compared to that under the nanosized pyramidal tip [28].

The poor fit of the viscoelastic time-dependent models on cartilage relaxation behavior suggests that intermolecular reptation and/or friction induced viscoelasticity may not be the only molecular origin that contributes to the time-dependent manner in the short time range. In fact, poroelasticity from fluid flow and local pressure gradient has been identified in cartilage tissue mechanics, and could be a critical component that determines cartilage short-time relaxation behaviors [97]. In the longer time scope, viscoelasticity model predicts the cartilage relaxation relatively well, Figure 6-6b. Depletion of GAGs accelerates the longer-time stress relaxation, as measured by both probe tips, as the presence of proteoglycan increases the solution viscosity and hinder the movement of the collagen fibrils.

6.5.4 Cartilage dynamic nanomechanics

The slowest characteristic poroelastic deformation time constant could be estimated as [108],

$$\tau \sim \frac{L^2}{Hk} \tag{6.9}$$

, where L is the characteristic deformation length scale ($\sim$ 1 μm in this sytem), H the bulk modulus ($\sim$ 1 MPa) and k the cartilage permeability ($\sim 10^{-15}$ $\mathrm{m}^4 \cdot \mathrm{N}^{-1} \cdot \mathrm{s}^{-1}$) [108]. The reason that there is no significant difference between the stiffness measured at 316 and 1000 Hz for the untreated disk (Figure 6-7) could be due to the fact that

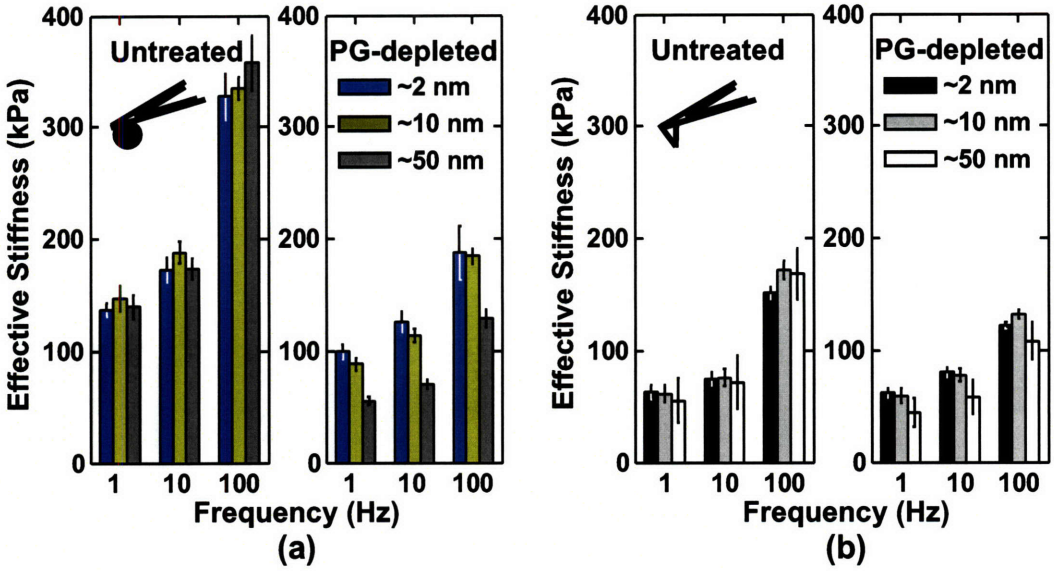

Figure 6-9: Estimated stiffness of untreated and PG-depleted cartilage disks (thickness $\sim$ 0.5 mm) measured OH-SAM functionalized (a) colloidal probe tip ($R \sim 2.5$ μm, $k \sim 0.58$ N/m) and (b) standard nanosized pyramidal probe tip ($R \sim 50$ nm, $k \sim 0.58$ N/m) as a function of deformation frequency ($1 - 100$ Hz) at different deformation amplitudes ($\sim 2 - 50$ nm), estimated via Hertz model, mean $\pm$ SEM, $n \geq 6$ different positions.

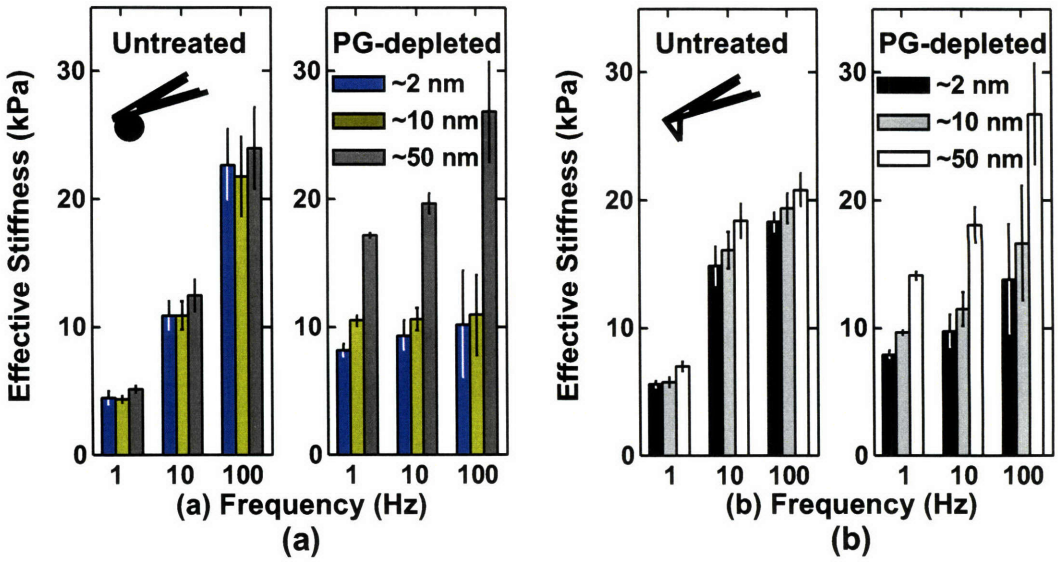

Figure 6-10: Estimated phase lag of deformation with respect to applied force of untreated and PG-depleted cartilage disks (thickness ~ 0.5 mm) measured OH-SAM functionalized (a) colloidal probe tip ($R \sim 2.5$ μm, $k \sim 0.58$ N/m) and (b) standard nanosized pyramidal probe tip ($R \sim 50$ nm, $k \sim 0.58$ N/m) as a function of deformation frequency ($1 - 100$ Hz) at different deformation amplitudes ($\sim 2 - 50$ nm), estimated via Hertz model, mean $\pm$ SEM, $n \geq 6$ different positions.

these frequencies are corresponding to the same order of its poroelastic relaxation time, $\tau \sim 1$ ms. Enzymatic digestion of the proteoglycan content increase the permeability k for ~ 1000 fold, and $\tau \sim 1$ μs for the PG-depleted disk. Hence, a significant increase in E was observed for the PG-depleted cartilage in $1 - 1000$ Hz frequencies. The increase of phase lag from 1 to 1000 Hz for both disks (Figure 6-8) suggests the energy-dissipative deformation mechanisms are more important at higher deformation frequencies. At ~ 2 nm deformation amplitude, the same order of the GAG-spacing ($2 - 4$ nm) along aggrecan core protein [109] and much less than other dimensional features in cartilage (e.g. collagen fibril diameter, pore size, aggrecan contour length etc.), the energy-dissipation could be originated from the poroelasticity-related molecular frictions between GAG and solvent molecules, or molecular friction among GAG branches and collagen fibrils. As the proteoglycan motif is entrapped in the solid type II collagen matrix, it could protect the collagen fibrils from molecular contacts between two nonadjacent fibrils due to large deformation, at higher deformation amplitudes (~ 50 nm), the proteoglycan and collagen fibrils could be moving together, and the energy dissipation mechanism are hence similar to the smaller amplitudes. Hence, the measured stiffness and phase lag are the same at different amplitudes for the nontreated disk (Figures 6-9, 6-10). Without the proteoglycan motif, the collagen scaffold would collapse at larger deformation amplitude and molecular contacts between nonadjacent fibrils could occur. Hence, a lower stiffness with larger phase lag was measured (Figures 6-9, 6-10). Interestingly, changing the probe tip geometry did not change any of the frequency or amplitude dependence trends on either disk, this could be due to the fact that the deformation amplitudes, even as high as ~ 50 nm, is less than the dimension of aggrecan, and hence the splay-like deformation induced by the sharp pyramidal probe tip could have less effect on the nanoscale dynamic deformation.

6.6 Conclusions

In this study, we quantified the quasistatic and dynamic deformation of cartilage and its associated collagen network via both spherical and pyramidal probe tips. Depletion of the proteoglycan content resulted in a decrease in stiffness and characteristic relaxation time constant. Frequency-dependence of oscillatory dynamic deformation properties could be related to the poroviscoelastic mechanisms on nanoscale. The different frequency dependence at deformation deformation amplitudes could be associated with the characteristic structural features of the untreated and PG-depleted cartilage disks.

Appendix A

Microcontact Printing and Lateral Force Microscopy Imaging

The technique of microcontact printing (μCP) [163], or soft lithography, has been applied to prepare the micropatterned surface of different self-assembled monolayers (SAMs) with well-defined boundaries. Previously, these chemically-patterned substrates were employed to probe surface chemical properties of different SAMs, as two or more different SAMs could be studied simultaneously on the same substrate and ambient conditions [159, 91, 129]. In this study, a number of thiol-end functionalized SAMs were used as control experiment for lateral force microscopy on aggrecan end-attached micropatterned surface (see Table A.1).

To prepare a micro-patterned substrate composed of two different SAMs, a polydimethylsiloxane (PDMS) stamp with hexagonal-shaped indentations (10 μm side length) on its surface was immersed in 3 mM ethanol solution of the first type of SAM molecule for a minimum of 30 min. Silicon wafers were coated with 2 nm of Cr and 50 nm of Au via thermal evaporation in 10^{-6} Torr vacuum and cut into 1 cm $\times$ 1 cm square samples before using. The gold-coated substrates were immersed in fresh Piranha solution (volume ratio 3:1 mixture of 98% H_2SO_4 and 30% H_2O_2) for $15 - 20$ minutes to remove organic contaminations. The PDMS stamp was then taken out of SAM solution, dried in air for $\sim$ 1 minute and the patterned surface was immediately brought into contact with the Piranha-treated gold substrate for $1 - 2$

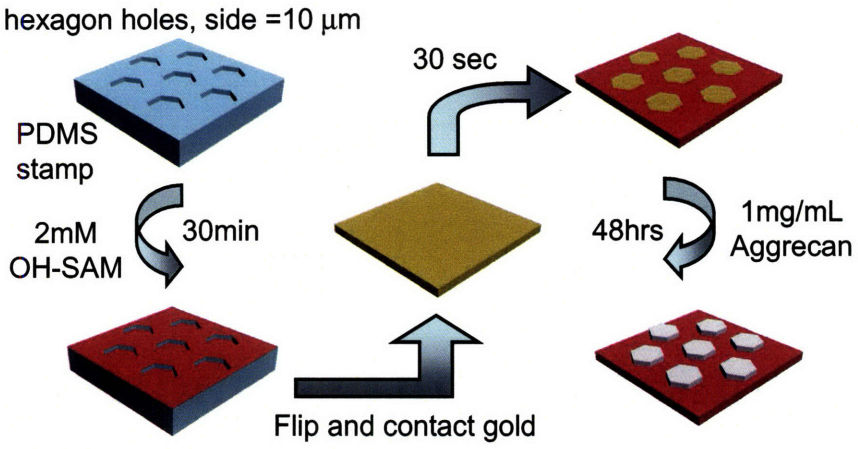

Figure A-1: Schematic of formation of aggrecan-OH-SAM patterned surface via microcontact printing using a hexagonal patterned PDMS stamp.

minutes. The first SAM is chemically attached to the region outside hexagons on the substrate through thiol-gold chemical bonds. Afterwards, non-specifically absorbed SAM molecules are rinsed away with ethanol and the substrate is then incubated in a 3 mM ethanol solution of the second type of SAM solution overnight to form well-defined SAM layer inside the hexagons. A chemically patterned substrate was prepared via μCP, as illustrated in Figure A-1. The substrate is then imaged using lateral force microscopy with chemically functionalized AFM probe tips. Different lateral forces from the regions covered by different SAMs would result in a hexagonal-shaped pattern via lateral force microscopy imaging.

Lateral force microscopy (LFM) is a special contact mode atomic force microscopy, in which mode, the scan angle (the scanning direction of AFM tip to its reference direction, the point-out direction of the cantilever) is set to 90°, and the probe tip scans across the surface under a constant normal force. The cantilever twists in the scanning (lateral) direction resulting in a horizontal deflection of the laser spot on a 4-quadrant position sensitive photodiode (PSPD), giving a voltage output proportional to lateral deflection. The lateral force signal is at least an order of magnitude smaller than the interference from normal deflection, thus in order to avoid the cross-talk effect from normal signal, both the trace (forward) and retrace (backward) lateral

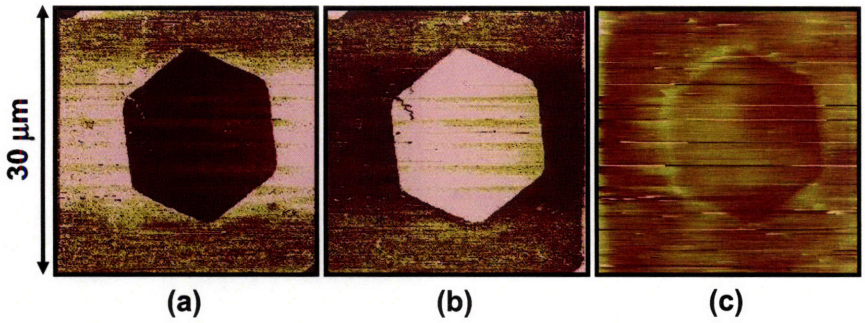

Figure A-2: (a) Trace and (b) Retrace LFM images of COOH-CH_3 patterned substrate with a CH_3-functional probe tip ($R \sim 50$ nm, $k \sim 0.06$ N/m) under ~ 5 nN applied normal force in air with COOH-SAM outside the hexagon and CH_3-SAM inside , where the brighter contrast corresponds to the larger lateral signal in (a) and smaller lateral signal in (b). (c) Height image recorded simultaneously.

scan signals are recorded. Scanning in both directions, the cantilever is twisted in two opposite directions while the cross-talk of normal signals remains the same. The real lateral signal is taken as the half-width of the lateral signal loop. As surface topography could significantly affect the measured lateral signal [144], the measurements on surface chemistry are conducted on flat substrates. Upon proper calibration, the absolute values of lateral force (nN) can be quantified. Lateral force microscopy has been applied to study a number of surface properties, e.g., adhesion, friction, hydrophobicity [130, 128, 150, 151, 112], surface roughness [17], and pharmaceutical interactions [29].

To test the techniques of μCP and LFM, the control experiment was firstly performed on a microcontact printed substrate with hexagonal patterns, with the methyl-functionalized self-assembled monolayer (CH_3-SAM, ethanethiol, CH_3CH_2HS, Aldrich, St. Louis, MO) inside the hexagon and carboxyl-functionalized SAM (COOH-SAM, 11-mercaptoundecanoic acid, $HOOC(CH_2)_{10}HS$, Aldrich) outside. LFM was applied using a CH_3-SAM functionalized standard nanosized AFM probe tip (NP tip D, silicon nitride, V-shaped cantilever, Veeco, Santa Barbara, CA) in air. Larger lateral signals in the COOH patterned region resulted in a brighter contrast on the trace image and darker contrast on a retrace map outside hexagons, Figure A-2a,b,

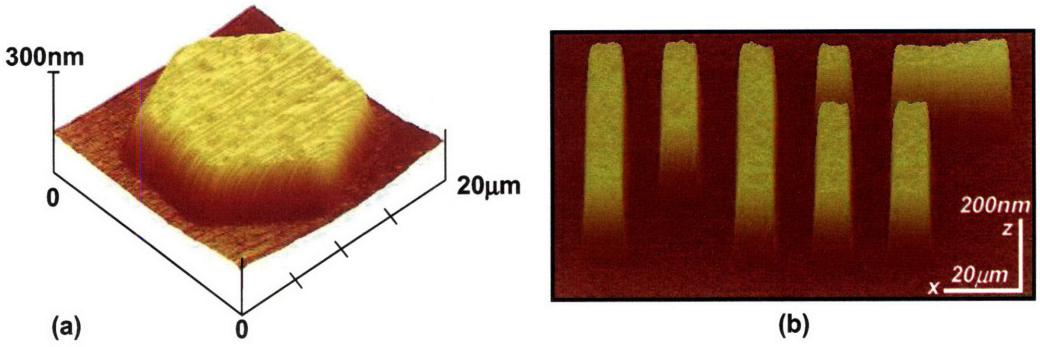

Figure A-3: Three dimensional AFM height images of aggrecan-OH-SAM patterned substrates in 0.001M NaCl aqueous solution with aggrecan inside the patterns and OH-SAM outside: (a) hexagon, (b) MIT logo patterns via an OH-SAM functionalized nanosized probe tip ($R \sim 50$ nm, $k \sim 0.06$ N/m) under ~ 5 nN applied normal force.

consistent with the literature [156]. In air, the adhesion between methyl groups is mainly van der Waals, while stronger capillary forces are present between $-CH_3$ and $-COOH$ groups, and hence "stick-slip" induced friction are stronger between the latter. As predicted, there is no remarkable pattern observed in the height image, since the height difference between the two SAMs was negligible (< 1 nm), Figure A-2c.

Aggrecan and hydroxyl-SAM (OH-SAM, 11-mercaptoundecanol, $HO(CH_2)_{11}HS$, Aldrich) micropatterned surface was prepared in a similar fashion, in which case the clean gold-coated substrate was incubated in 50 μL 1 mg/mL aggrecan solution for 48 hours after μCP of OH-SAM. Marked height difference could be measured between the aggrecan and OH-SAM layers, suggesting the successful end-attachment of aggrecan on the gold-coated substrate, Figure A-3. Using this micropatterned substrate, aggrecan compressive and shear nanomechanical properties were studied in $0.001 - 1.0$ M NaCl aqueous solutions and NaCl + $CaCl_2$ aqueous solutions ($[Cl^-]$ = 0.15 M) by using both the standard nanosized pyramidal (end-radius $R \sim 50$ nm) and colloidal spherical (end-radius $R \sim 2.5$ μm) probe tips (see Chapters 3 and 4).

Table A.1: Thiol end-functionalized self-assembled monolayers

Chemical Name	Chemical Formula	End-Functional Group	MW (g/mol)
11-mercaptoundecanoic acid	$HS(CH_2)_{10}COOH$	-COOH	218.36
11-mercaptoundecanol	$HS(CH_2)_{11}OH$	-OH	204.37
2-mercaptoethanesulfonic acid, sodium salt	$HS(CH_2)_2SO_3Na$	$-SO_3^-$	164.18
ethanethiol	$HSCH_2CH_3$	$-CH_3$	62.13
2-mercaptoethylamine hydrochloride	$HS(CH_2)_2NH_2 \cdot HCl$	$-NH_2$	113.61

Appendix B

Lateral Force Calibration

B.1 Wedge method for calibration of nanosized probe tips

Lateral deflection signals (V) from a position sensitive photodiode (PSPD, resolution $\sim$ 1 mV) were recorded during line scans. To convert these data into forces, the lateral cantilever deflection sensitivity, α (nN/V), had to be determined. Different calibration methods have been used [113, 157, 54, 15, 46, 72, 93, 34, 142, 141, 9] and compared [16] previously to quantify α. Among these, the nondestructive "wedge" method [113, 157], which calibrates the ratio of α to the normal deflection sensitivity β (nN/V), has been the most widely accepted. This approach can be performed in combination with lateral force experiments, thereby eliminating uncertainties introduced by a separate calibration of cantilever stiffness and by changes in experimental conditions including the optical geometry of the laser beam path. The wedge method was first developed using standard nanosized silicon AFM probe tips ($R < 100$ nm) to scan $SiTiO_3$ samples having geometrically well specified slopes (i.e., the (101) and (103) crystallographic planes) [113]. Varenberg et al. [157] extended this approach by replacing the $SiTiO_3$ sample with an etched silicon calibration sample having both planar and tilted regions (TGF-11, Mikromasch, Wilsonville, OR). This technique allowed use of probe tips having an end-radius $R <\sim 1$ μm. In this study, we mod-

ified the calculation procedure of α by removing the assumption that the applied normal force remains constant on the horizontal and tilted regions during scanning. In addition, we extended the wedge method to calibrate larger probe tips with end-radii $R > 1$ μm. In this case, the reported method using the TGF-11 sample cannot be used because the probe tip makes simultaneous contact with both the horizontal and tilted regions when scanning (i.e., the length of the tilted region ~ 1 μm, the slope 54°44′) resulting in noise that was an order of magnitude larger than the lateral deflection signal itself. By using two different mica samples, one horizontal and the other tilted at $\sim 20°$, we developed new calibration procedures and analysis for larger probe tips, which is applicable to probe tips with smaller end-radii as well. In order to clarify our modifications on the wedge method, we use the approach based on Eqs. $1 - 12$ of Varenberg et al. [157]. The tip (height h, end-radius R, Figure B-1) is subjected to forces applied by the probe tip (i.e., the contact, adhesion, and friction forces N, A, and f, respectively), and the cantilever of thickness t (i.e., the applied normal and lateral force, L and T, and the torsion moment M). The subscripts u and d are corresponding to the forces and moments during uphill and downhill motions, respectively. Momentum equilibrium is described for uphill and downhill motions by Eqs. 11 and 12 in [157]:

$$M_u + L_u R \sin\theta - T_u(R\cos\theta + h - R + \frac{t}{2}) = 0 \tag{B.1}$$

$$M_d + L_d R \sin\theta - T_d(R\cos\theta + h - R + \frac{t}{2}) = 0 \tag{B.2}$$

For nanosized probe tip $h >> R$, Eqs. B.1 and B.2 are simplified as

$$M_u = T_u(h + \frac{t}{2}) \tag{B.3}$$

$$M_d = T_d(h + \frac{t}{2}) \tag{B.4}$$

The nanosized probe tip used in this study was calibrated following the experimental procedures described in [157]. A series of 1.1 μm lateral scan loops (256 datapoints each on trace and retrace) were performed on the TGF-11 calibration grid (surface

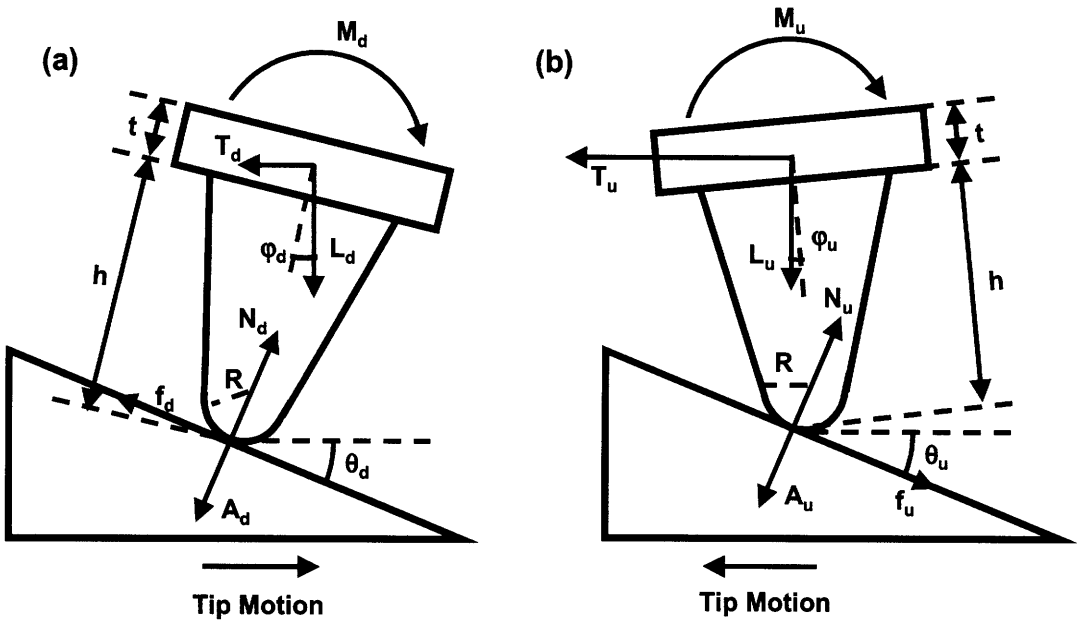

Figure B-1: Free-body diagrams of the cantilever tip during scanning in both (a) trace (downhill) and (b) retrace (uphill) motions, adapted from Fig. 1 of Varenberg et al. [157], where R is the tip end-radius, h the tip height, t the cantilever thickness, u and d the slope angles of the tilted region during upward and downward scans respectively, N, A, and f are the contact, adhesion, and friction forces executed between the probe tip and the sample surface, respectively, and L, T, M are the applied normal and lateral forces, the torsion moment respectively. The subscripts u and d are corresponding to the forces and moments during uphill and downhill motions, respectively.

roughness $\sim$ 13.5 nm, slope of tilted region = 54°44′) at varying applied normal force. Each scan loop included both horizontal and tilted regions (Figure B-2) at a 1 Hz scan rate (2.2 μm/s); scanning rates exceeding 3 μm/s on the tilted region resulted in the noise at least an order of magnitude larger than the lateral signal. Three types of signals were measured from each lateral scan loop: the half-width of the lateral signals loop in the horizontal region, $W_o(0)$(corresponding to the data in region I in Figure B-2), the half width in the tilted region, $W_o(\theta)$(region II in Figure B-2), and the offset of baseline signal in the tilted region related to that in the horizontal region $\Delta_o(\theta - 0)$(i.e., the mean value of the trace-retrace signal loop in region I minus mean value in region II). The subscript o indicates the PSPD lateral signal measured in volts rather than converted data (force in nN). The lateral signal loop, Figure B-2, is directly related to the moments M and lateral forces T:

$$\frac{W}{h + t/2} = W_o\alpha = \frac{M_u - M_d}{2(h + t/2)} = \frac{T_u - T_d}{2} \tag{B.5}$$

$$\frac{\Delta(\theta - 0)}{h + t/2} = \Delta_o(\theta - 0)\alpha = \frac{M_u + M_d}{2(h + t/2)} = \frac{T_u + T_d}{2} \tag{B.6}$$

The adhesion force A is measured to be negligible and, hence, it can be calculated as a function of applied normal force L,

$$W_o\alpha = \frac{(1 + \mu^2)(L_u - L_d)\sin\theta\cos\theta + \mu(L_u + L_d)}{\cos^2\theta - \mu^2\sin^2\theta} \tag{B.7}$$

$$\Delta_o(\theta - 0)\alpha = \frac{(1 + \mu^2)(L_u + L_d)\sin\theta\cos\theta + \mu(L_u - L_d)}{\cos^2\theta - \mu^2\sin^2\theta} \tag{B.8}$$

B.2 New modifications of wedge method for calibration of nanosized probe tips

It was observed that scanning on a tilted surface resulted in normal deflection errors that could not be corrected by the AFM instrument and, thus, $L_u \neq L_d$(Figure B-2). The deflection signals recorded were used to calculate the normal forces exerted from

the cantilever,

$$L = (d + s - b_V) \times \beta \tag{B.9}$$

where d is the vertical deflection signal, s the setpoint, b_V the vertical baseline (corresponding to the vertical signal in the unengaged state), and β (nN/V) the cantilever's normal deflection sensitivity, which is the product of its normal spring constant k (nN/nm) and inverse optical lever sensitivity (nm/V) [79]. For a given tilted angle θ and tip scanning rate, d was observed to be independent of s and remained constant during scanning under a series of vertical setpoints. In addition, it was found that for uphill and downhill motion,

$$d_u = -d_d \tag{B.10}$$

The applied normal force can be rewritten as,

$$L_u = L_0 + \delta \tag{B.11}$$

$$L_d = L_0 - \delta \tag{B.12}$$

where $L_0 = (s - b_V) \times \beta$ is the normal force on the horizontal surface (the subscript 0 indicates the force on the horizontal region), and $\delta = d_u\beta$ is the additional normal force that resulted from scanning on a tilted surface. The value δ was observed to remain constant for the series of applied normal forces L_0 at a given tilted angle and tip displacement rate (Figure B-2). Hence,

$$W_o\alpha = \frac{\mu L_0 + (1+\mu^2)\delta \sin\theta\cos\theta}{\cos^2\theta - \mu^2\sin^2\theta} \tag{B.13}$$

$$\Delta_o(\theta - 0)\alpha = \frac{(1+\mu^2)L_0 \sin\theta\cos\theta + \mu\delta}{\cos^2\theta - \mu^2\sin^2\theta} \tag{B.14}$$

$W_o(0)$, $W_o(\theta)$ and $\Delta_o(\theta - 0)$ were plotted as a function of applied normal force L_0 (Figure B-3), where each data point represents the mean of 8 lateral scan loops at different locations, and the slopes $W_o' \equiv dW_o/dL_0$ and $\Delta_o(\theta - 0)' \equiv d\Delta_o(\theta - 0)/dL_0$ were measured from the data of Figure B-3. Due to the observed independence of δ on L_0, the lateral proportionality coefficient μ between the tip and substrate in the

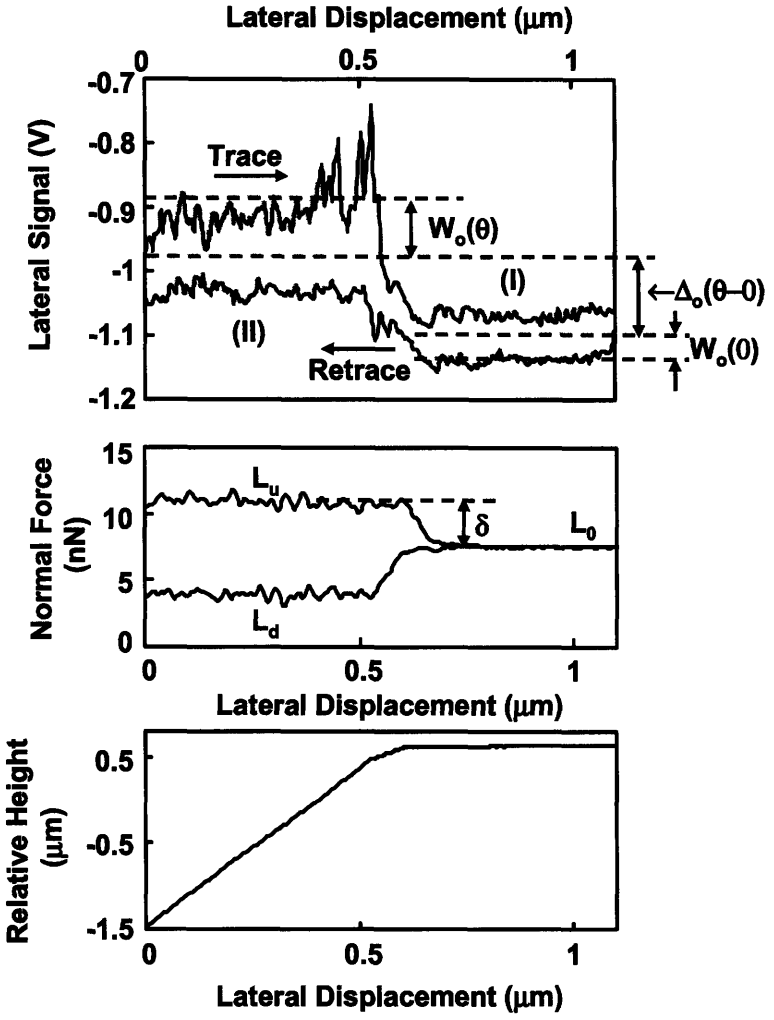

Figure B-2: Lateral signal loop on silicon calibration sample in deionized water with corresponding normal force and height profile using an OH-SAM functionalized nano-sized probe tip ($R \sim 50$ nm, nominal cantilever spring constant, $k \sim 0.06$ N/m, at a normal force, $L_0 \sim 7$ nN; (I) is the tilted area of the sample (corresponding to an angle $\theta = 54°44'$), (II) is the horizontal area of the sample (corresponding to an angle $\theta = 0°$), W_o is the magnitude of the average lateral signal within each shaded region (taken at 10% from the edge of the tilted-horizontal border), and Δ_o is the baseline offset of the tilted region, L_u is the applied normal force profile during uphill motion (trace), and L_d during down hill motion (retrace).

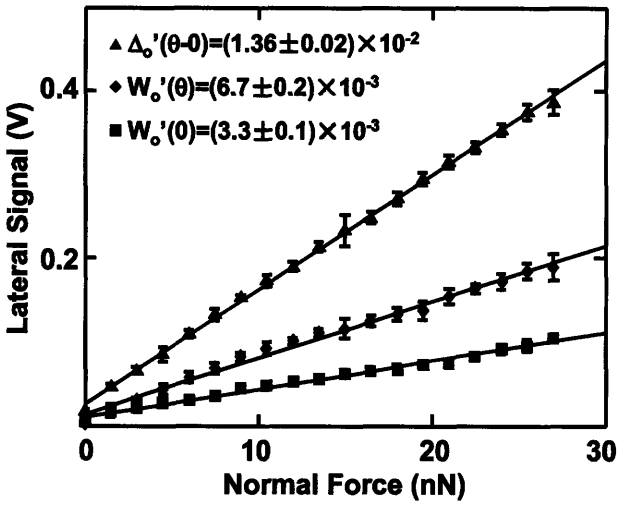

Figure B-3: Lateral calibration parameters W_o and Δ_o versus normal force where slopes of these curves are given as inset text (indicated by primes) using an OH-SAM functionalized nanosized probe tip ($R \sim 50$ nm, nominal cantilever spring constant, $k \sim 0.06$ N/m). Each data point represents 8 independent scan loops under a fixed applied normal force.

tilted region was calculated following [113]:

$$\mu + \frac{1}{\mu} = \frac{2\Delta_o'(\theta - 0)}{W_o'(\theta)\sin 2\theta} \tag{B.15}$$

The lateral sensitivity α was calculated as:

$$\alpha = \frac{1}{W_o'(\theta)} \frac{\mu}{\cos^2\theta - \mu^2 \sin^2\theta} \tag{B.16}$$

and the lateral proportionality coefficient on the horizontal surface was then calculated as,

$$\mu_0 = \alpha W_o'(0) \tag{B.17}$$

The true physical value of μ and μ_0 may not be equal but should be close to each other, hence the physical solution from the two possible solutions derived from Eqs. B.15 to B.17, (μ_1, α_1) and (μ_2, α_2), was determined by comparing the values of $|\mu - \mu_0|$; the solution corresponding to the smaller $|\mu - \mu_0|$ is the real solution [157]. The nanosized

probe tip used to obtain the lateral force data for both the control and aggrecan shear experiments was found to have a lateral sensitivity $\alpha = 122 \pm 2$ nN/V (Figure B-3). Thus, using a PSPD with $\sim$ 1 mV resolution, the minimum detectable amount of lateral force was $\sim$ 100 pN, based on the measured lateral sensitivity.

B.3 Modifications of wedge method for calibration of microsized probe tips

The lateral sensitivity of the microsized (colloidal) probe tip used in this study could not be calibrated using the wedge method since the radius of the colloid is bigger than the length of the tilted region, and scanning on a tilted region having $\theta = 54°44'$ resulted in uncorrectable noise due to the relatively large tilted angle. We therefore replaced the TGF-11 sample (Mikromasch) with two mica substrates, one having a horizontal surface and the other a surface with tilt angle $\theta \sim 20°$. A series of 10-μm lateral scan loops (256 datapoints each on trace and retrace) was performed on both the horizontal and the tilted mica substrates at varying applied normal force at 1 Hz scan rate (20 μm/s). The half-widths and the offsets of baseline signals of the lateral signal loops were measured from both the horizontal ($W_o(0)$ and $\Delta_o(0)$) and the tilted ($W_o(\theta)$ and $\Delta_o(\theta)$) samples. The jump of the baseline offset $\Delta_o(\theta - 0)$ from the horizontal to the tilted sample could not be directly measured, for one single scan loop including scanning on both horizontal and tilted regions could not be obtained when using two separate samples. However, the lateral baseline offset was found to be affected only by two factors, the applied normal force L_0 due to the crosstalk between the normal and the lateral deflection signals, and the tilt angle θ, which causes the lateral projection of the compression force N (Figure B-1). The crosstalk between normal and lateral deflection signals is determined by the laser path from the AFM head to the PSPD [144] and, hence, the effect of the crosstalk is the same during scanning on the two different samples as long as the optical laser beam path is untouched while changing the samples. In that case, the difference of lateral baseline

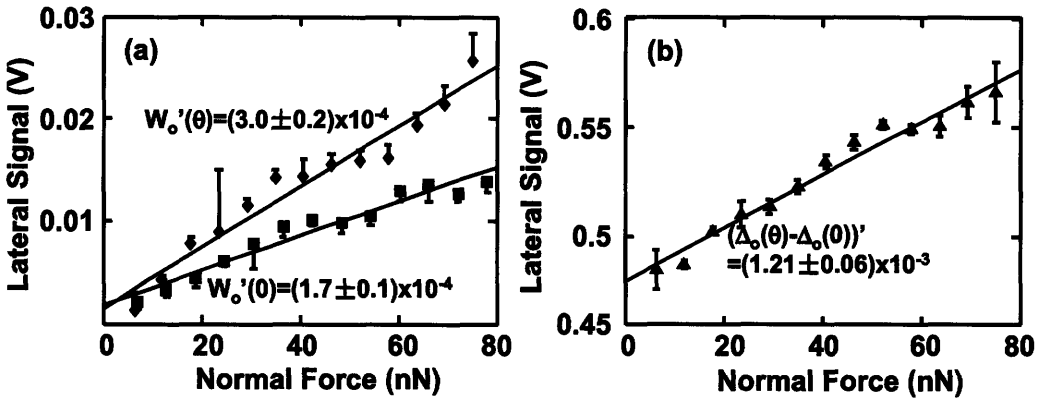

Figure B-4: (a) Half-width of lateral signal loop W_o on both the tilted ($W_o(\theta)$, $\theta \sim 20°$) and horizontal ($W_o(0)$) mica substrates as a function of applied normal force using an OH-SAM functionalized microsized probe tip ($R \sim 2.5$ μm, nominal cantilever spring constant, $k \sim 0.12$ N/m). (b) Lateral signal baseline offset jump ($\Delta_o(\theta) - \Delta_o(0)$) as a function of applied normal force. Each data point represents 8 independent scan loops under a fixed applied normal force in (a), and two pairs of 8 independent scan loops under a fixed applied normal force on the tilted and horizontal mica substrates in (b).

dependences on normal force measured on these two samples, $(\Delta_o(\theta) - \Delta_o(0))'$, has the same physical meaning of lateral baseline jump from a horizontal to a tilted region on one single scan on the same sample, $\Delta_o'(\theta - 0)$. For the microsized probe tip, where $h = 2R$, Eqs. B.1 and B.2 are simplified as,

$$M_u = T_u[R(1+\cos\theta) + \frac{t}{2}] - L_u R\sin\theta \tag{B.18}$$

$$M_d = T_d[R(1+\cos\theta) + \frac{t}{2}] - L_d R\sin\theta \tag{B.19}$$

Hence, with negligible measured adhesion force A, the two calibration parameters are calculated as,

$$\frac{W}{h+t/2} = W_o\alpha = \frac{M_u - M_d}{2[R(1+\cos\theta)+t/2]} = \frac{T_u - T_d}{2} - \frac{(L_u - L_d)\sin\theta}{2[R(1+\cos\theta)+t/2]} \tag{B.20}$$

$$\frac{\Delta(\theta)-\Delta(0)}{h+t/2}=[\Delta_o(\theta)-\Delta(0)]\alpha=\frac{M_u+M_d}{2[R(1+\cos\theta)+t/2]}=\frac{T_u+T_d}{2}-\frac{(L_u+L_d)\sin\theta}{2[R(1+\cos\theta)+t/2]} \tag{B.21}$$

Equations B.20 and B.21 can be written as a function of the applied normal force:

$$W_o\alpha=\frac{\mu L_0+(1+\mu^2)\delta\sin\theta\cos\theta}{\cos^2\theta-\mu^2\sin^2\theta}-\frac{\delta R\sin\theta}{[R(1+\cos\theta)+t/2](\cos^2\theta-\mu^2\sin^2\theta)} \tag{B.22}$$

$$(\Delta_o(\theta)-\Delta_o(0))\alpha=\frac{(1+\mu^2)L_0\sin\theta\cos\theta+\mu\delta}{\cos^2\theta-\mu^2\sin^2\theta}-\frac{L_0R\sin\theta}{[R(1+\cos\theta))+t/2](\cos^2\theta-\mu^2\sin^2\theta)} \tag{B.23}$$

and the lateral proportionality μ is then calculated as:

$$\frac{(\Delta_o(\theta)-\Delta_o(0))'}{W_o'(\theta)}=(\mu+\frac{1}{\mu})\sin\theta\cos\theta-\frac{1}{\mu}\frac{R\sin\theta}{[R(1+\cos\theta)+t/2]} \tag{B.24}$$

The cantilever lateral sensitivity α is calculated using Eq. B.16 and the same criteria used for the nanosized probe tip was used to determine the true physical solutions of μ and α. The microsized probe tip used in this study was calibrated to have a lateral sensitivity $\alpha = 148 \pm 17$ nN/V (Figure B-4).

Appendix C

Nanomechanical Properties of Aggrecan from Bovine Fetal Epiphyseal and Mature Nasal Cartilage

C.1 Introduction

Cartilage tissue is characterized by high stiffness and strength and some articular cartilage, the tissue on the surface of load bearing joints, able to withstand mechanical loads encountered over many years of life, ideally with little damage [107, 2]. The tissue's dense extracellular matrix (ECM) responsible for these mechanical properties is comprised mostly of water ($60-80\%$ by weight) and macromolecules, such as collagen type II ($\sim 60\%$ dry weight) and proteoglycans ($\sim 35\%$ dry weight). The mechanical properties of the tissue are directly related to the structure and interactions of these various macromolecules [99].

Of the various proteoglycans found in cartilage, the most abundant ($\sim 50-85\%$ by weight) is aggrecan [76], which is thought to be responsible for $\sim 50\%$ of the compressive stiffness of the tissue [14, 37]. It is distinguished by its ~ 100 highly

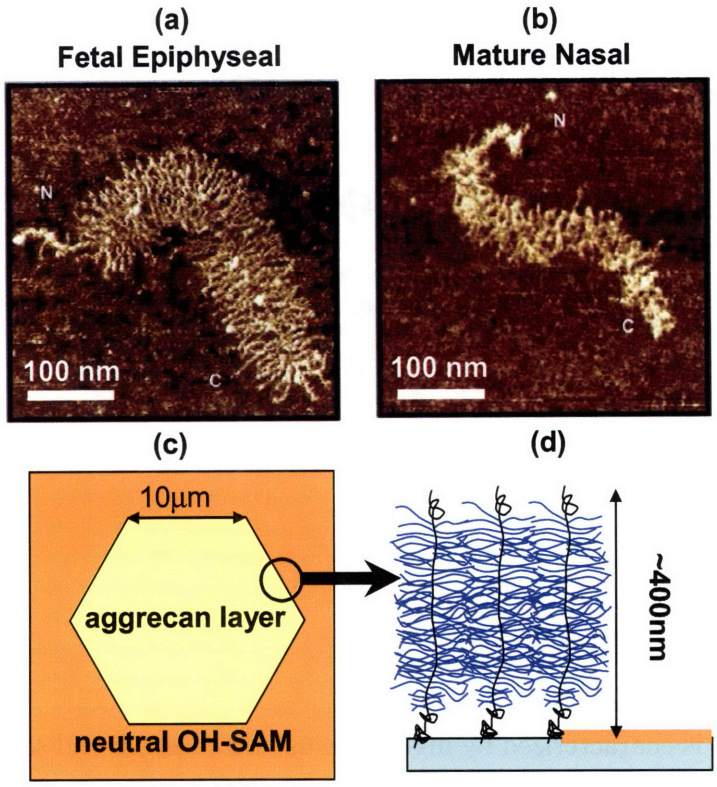

Figure C-1: Tapping mode AFM image in air of bovine (a) fetal epiphyseal and (b) mature nasal aggrecan [110]. Schematic of patterned sample used in the nanomechanics experiments (c) top view and (d) side view of the area indicated in the circle.

negatively charged chondroitin sulfate glycosaminoglycan (CS-GAG) chains attached to a core protein in a "bottle-brush" like structure (Figure C-1) [110]. GAG length, spacing, and sulfation are known to vary with age, source, and location [110, 11, 105]. These differences in structure are thought to contribute to the wide variations in observed biomechanical properties of cartilage [165]. This study focuses on the molecular-level compressive properties of aggrecan taken from two different bovine tissues, fetal epiphyseal and mature nasal cartilage.

Previously, individual aggrecan from two different bovine cartilage samples, fetal epiphyseal (FE) and mature nasal (MN), were imaged via atomic force microscopy (AFM) (Figure C-1a,b) [110]. The significantly different architectural features of these two types of aggrecan are distinguished, as shown in Table C.1 [110]. The molecular stiffness of the two different aggrecan, characterized as the persistence length, from the AFM images of isolated aggrecan molecules deposited on the planar mica surfaces were quantified. Both the core protein and the GAG chains were found to have significantly shorter persistence length in the MN compared to the FE aggrecan, Table C.2.

The AFM images of aggrecan on mica in air show great detail and help to visualize the single molecule stiffness. However, in tissue, aggrecan is very densely packed (average GAG spacing $\sim$ 3 nm [110]) in solution ($\sim$ 0.15 M ionic strength). Moreover, the aggrecan core protein is noncovalently bonded to hyaluronan, strengthened by its G1 domain (amine terminal end globular domain), to form large aggregates. Therefore, in order to understand how the molecular-level compressive properties of aggrecan change between different tissues *in vivo*, it is important to directly measure these properties in a more native-like state.

We previously reported the nanoscale compressive interaction forces between opposing end-grafted FE aggrecan layers, and found that the measured normal stress at near physiological ionic strength (IS) of 0.1 M NaCl increased sharply at aggrecan densities under the tip of $\sim 40 - 50$ mg/mL, which corresponds to an average 3D-GAG spacing of $\sim 4 - 5$ nm (or $4 - 5\times$Debye length) [27, 28]. This characteristic spacing is consistent with the onset of significant electrostatic interactions between

GAG chains of opposing aggrecan molecules at physiological IS. The objective of this study was to test the hypothesis that the nanomechanical properties of MN aggrecan are very different from those of FE aggrecan, as suggested by the measured age and source-related differences in GAG length, spacing, and sulfation.

C.2 Methods

Cantilevers with micron-sized gold-coated silica colloids (BioForce Nanosciences, end-radius $R_{tip} \sim 2.5$ μm, nominal spring constant $k \sim 0.12$ N/m) were functionalized with a OH-terminated self-assembled monolayer (OH-SAM, $HS(CH_2) - 11OH$) by immersion in 3 mM 11-mercaptoundecanol (Aldrich, St Louis, MO) in ethanol for 48 hours. Aggrecan and OH-SAM patterned planar substrates were prepared by micro-contact printing [163], as previously described [27]. The regions outside a hexagonally-shaped repeating pattern on the gold substrate were filled with an OH-SAM using a polydimethylsiloxane stamp (Figure C-1c). Purified A1A1D1D1 fetal bovine epiphyseal (FE) aggrecan, MW $\sim$ 3 MDa, and mature nasal (MN) aggrecan, MW $\sim$ 2 MDa [110], were end-functionalized by reaction with 1 mM dithiobis(sulfosuccinimidyl propionate) and 0.1 mM dithiothreitol (Pierce, Rockford, IL), each for 1 hour [27]. Excess reactants were removed by spinning (3500 rpm) overnight with a centrifugal filter (Centricon, Millipore, 10 kDa cutoff). Approximately 100 μL of 1 mg/mL thiol-functionalized aggrecan solution was then incubated on the patterned sample for 48 hours in a humidity chamber. Aggrecan was therefore chemically end-grafted inside the hexagon patterns while the area outside was coated with OH-SAM [27] (Figure C-1c,d). Prior to nanomechanical measurements, the surfaces were thoroughly rinsed with deionized water.

The aggrecan packing density within the hexagons, measured via dimethylmethylene blue (DMMB) dye assay [45], was $\sim$ 8 mg/m^2 ($\sim$ 1 aggrecan per 25 nm $\times$ 25 nm, equivalent) for both the FE and MN aggrecan samples. A Multimode PicoForce Nanoscope IV atomic force microscope (AFM, Veeco, Santa Barbara, CA) was used to measure the height of the aggrecan monolayer as well as the force be-

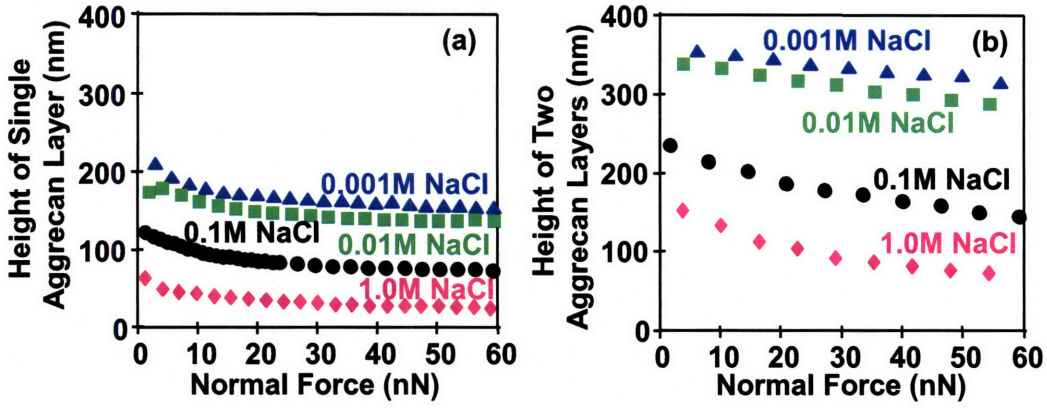

Figure C-2: Height versus normal force for (a) one single and (b) two opposing end-grafted mature nasal aggrecan monolayers at different ionic strengths ($0.001 - 1.0$ M NaCl) measured by an OH-SAM functionalized colloidal probe tip (end-radius $R_{tip} \sim 2.5$ μm, nominal spring constant $k \sim 0.12$ N/m).

tween the aggrecan layer and the neutral probe tip. The height of the aggrecan monolayer was measured using contact mode AFM in different ionic strength (IS) solutions ($0.001 - 1.0$ M NaCl, pH ~ 5.6) at different compressive loads ($\sim 0 - 80$ nN). The normal compressive force versus tip-sample separation distance (F-D) between the identical OH-SAM probe tip and aggrecan layers was also measured using high resolution force spectroscopy (HRFS) [136].

F-D curves were converted to normal stress (s) versus normal molecular strain (ϵ) curves: s was calculated as the force per unit surface area using the surface element integration method [8], a variant of the Derjaguin approximation, and ϵ was $1 - (H/H_0)$, where H_0, the uncompressed aggrecan layer height, was set equal to the distance at which the measured normal force increased above noise level (~ 10 pN) in the HRFS experiment minus $5\times$ the Debye length ($\kappa^{-1} \sim 1$ nm) [27].

C.3 Results

The heights of both FE [28] and MN aggrecan decreased nonlinearly with increasing IS and increasing compressive force (Figure C-2). FE aggrecan height attained a maximum of ~ 320 nm at 0.001 M under low load (~ 0 nN) and a minimum of ~ 31

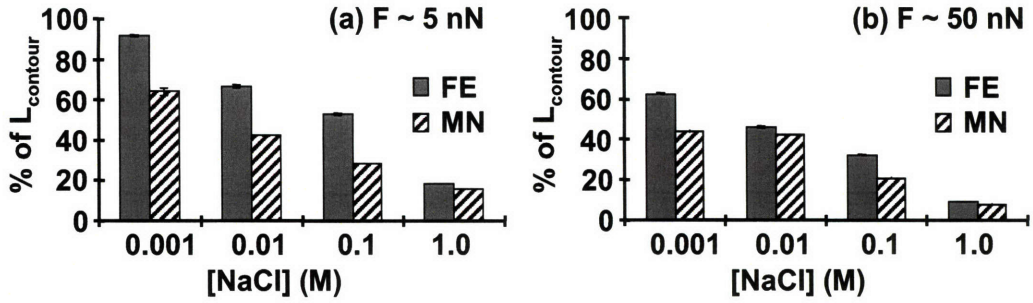

Figure C-3: Height (mean ± std) relative to their contour lengths of a single end-grafted layer of the FE (gray bars) and MN (hashed bars) aggrecan measured by an OH-SAM functionalized colloid tip ($R_{tip} \sim 2.5$ μm, $k \sim 0.12$ N/m) under (a) 5 nN and (b) 50 nN normal force.

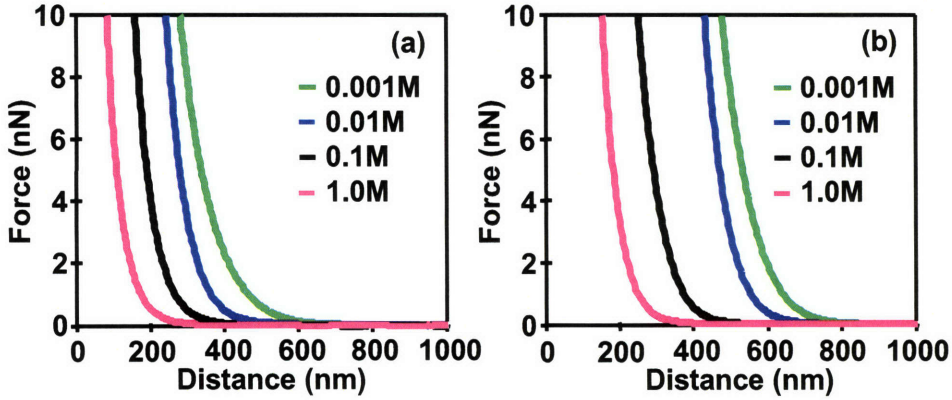

Figure C-4: Force versus separation distance between an end-grafted aggrecan layer and (a) an OH-SAM functionalized colloidal tip and (b) a colloidal tip with end-grafted aggrecan in varying ionic strength aqueous solutions (0.001 – 1.0 M NaCl) ($R_{tip} \sim 2.5$ μm, $k \sim 0.12$ N/m).

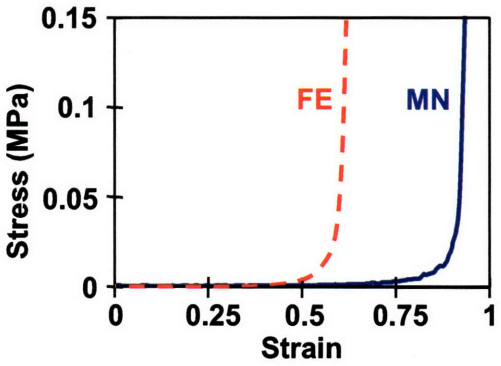

Figure C-5: Molecular stress versus strain of a single MN and FE aggrecan layers being compressed by an OH-SAM functionalized colloidal tip ($R_{tip} \sim 2.5$ μm, $k \sim 0.12$ N/m) in 0.1 M NaCl aqueous solution.

nm at 1 M under high load ($\sim$ 80 nN). MN aggrecan height attained a maximum of $\sim$ 208 nm at 0.001 M under low load and a minimum of $\sim$ 20 nm at 1 M under high load (Figure C-2b). The MN aggrecan required lower normal force than the FE aggrecan to compress to the same amount relative to its contour length, L_c. At 0.1 M NaCl, the MN compressed to $0.95 \times L_c$ whereas the FE aggrecan compressed to $0.66 \times L_c$ at $\sim$ 50 nN compressive force, Figure C-3. Force versus distance curves measured by HRFS with OH-SAM colloidal tips for the FE aggrecan (data not shown) was very similar to what has already been reported with similar tips [28]. The MN aggrecan HRFS force-distance data showed the same decrease in force with increase in IS (Figure C-4) as the FE aggrecan [28]. However, the forces were smaller for all the IS tested. In 0.1 M NaCl (near physiological IS), the forces measured using HRFS were nonlinear repulsive and started at $H \sim L_c$ (i.e. $s \sim 0$) for both types of aggrecan (Figure C-4). However, s increased nonlinearly with ϵ much more sharply for the FE than the MN aggrecan (Figure C-5). At $\epsilon = 0.5$, the measured stress was $> 10\times$ larger for the FE ($\sim$ 5 kPa) compared to the MN aggrecan ($\sim$ 0.3 kPa) (Figure C-5).

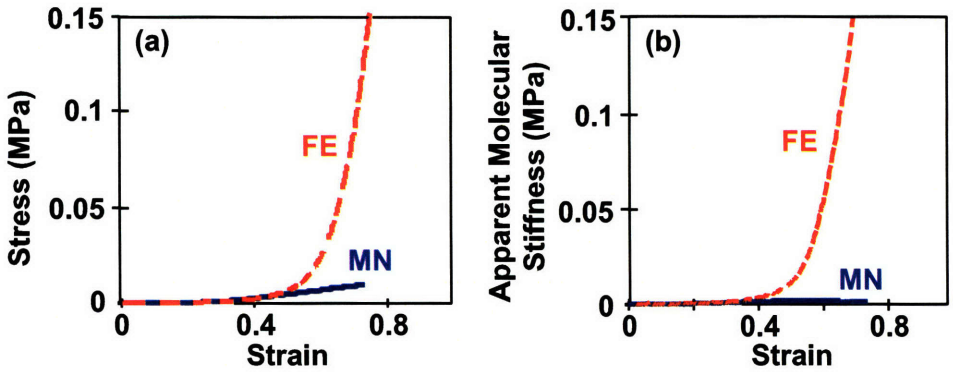

Figure C-6: Molecular (a) stress versus strain and (b) calculated apparent molecular stiffness versus strain in 0.1 M NaCl aqueous solution for two opposing MN and FE aggrecan layers via aggrecan-functionalized colloidal probe tips ($R_{tip} \sim 2.5$ μm, $k \sim 0.12$ N/m).

C.4 Discussion

Both types of aggrecan were end-grafted onto gold substrates at similar packing densities (within the physiological range of $20 - 80$ mg/mL [68]), thus allowing for direct comparison of their nanomechanical properties. The FE aggrecan layer was stiffer than the MN aggrecan for all the tested IS since more force was required to compress the FE layer to the same height relative to its contour length than MN aggrecan. This observation is likely due to the fact that the FE aggrecan has both increased electrostatic and nonelectrostatic (steric and entropic) repulsive interactions compared to the MN. The increased electrostatic forces come from the increased charge per GAG chain of FE compared to MN aggrecan, as well as the smaller GAG-GAG molecular spacing along the core protein. The increase in nonelectrostatic interactions may arise from the larger dimensions of the aggrecan (i.e., core protein and GAG L_c) and also the smaller GAG-GAG molecular spacing along the core protein. This is supported by the fact that the FE aggrecan appears to be stiffer than the MN at 1M NaCl when most of the electrostatic interactions are shielded. Although FE aggrecan is markedly stiffer than MN aggrecan at near physiological conditions (0.1 M NaCl, Figure C-5,C-6), they both exhibit similarly shaped nonlinear nanomechanical stress-

strain behavior. In cartilage tissue, aggrecan molecules are precompressed, occupying less volume than in the dilute extended conformation [68], even at zero tissue-level strain. Therefore it is difficult to know what value on the molecular stress-strain curve corresponds to tissue strain *in vivo*. However, these directly measured molecular-level stress-strain curves are similar to previous results on swelling pressure of proteoglycan solutions [35, 152]. This study further confirms that the mature bovine aggrecan is more compressible than the fetal aggrecan.

Table C.1: Summary of measured dimensions from AFM images of aggrecan (mean ± STD) [110]

	$L_{c,total}$ (nm)	R_{ee} (nm)	GAG spacing	$L_{c,\text{barecoreprotein}}$ (nm)	$L_{c,\text{CS-brush}}$ (nm)
Mature nasal aggrecan	352 ± 88	226 ± 81	–	81 ± 17	268 ± 73
Fetal epiphyseal aggrecan	398 ± 57	257 ± 87	–	93 ± 14	327 ± 43
Mature nasal GAG	32 ± 5	26 ± 7	4.4 ± 1.2	–	–
Fetal epiphyseal GAG	41 ± 7	32 ± 8	3.2 ± 0.8	–	–

Table C.2: Persistence length of aggrecan and GAG from AFM images [110]

	L_p (nm), mean	95% confidence interval (nm)
Mature nasal aggrecan	82	$73 - 94$
Fetal epiphyseal aggrecan	110	$102 - 120$
Mature nasal GAG	14	$10 - 21$
Fetal epiphyseal GAG	21	$17 - 25$

Appendix D

Effect of m-Calpain Degradation on Cartilage Aggrecan Nanomechanical Properties

D.1 Introduction

Aggrecan (contour length $L_{contour} \sim 400$ nm), the most abundant proteoglycan in the cartilage extracellular matrix, is known to provide $\sim 50\%$ of the compressive tissue modulus [100, 165] due to intra/intermolecular interactions between its densely packed chondroitin sulfate glycosaminoglycan (CS-GAG) side chains [65] ($L_{contour} \sim 40$ nm, molecular separation distance $\sim 2 - 4$ nm [110]). A number of enzymes present *in vivo* are responsible for the degradation of aggrecan by cleaving the core protein backbone at specific sites. For example, m-calpain, activated at $[Ca^{2+}] \sim$ mM (physiological), cleaves sites within the interglobular, chondroitin sulfate 1, and keratan sulfate domains [119]; aggrecanase (ADAMTS, a disintegrin and metalloprotease with thrombospondin motifs) cleaves sites within the interglobular and chondroitin sulfate domains [132], Figure D-1. One of the earliest events in osteoarthritis and post acute injury is the loss of aggrecan from cartilage, possibly due to the upregulation of these enzymes, which leads to irreversible deterioration of the tissue's biomechanical

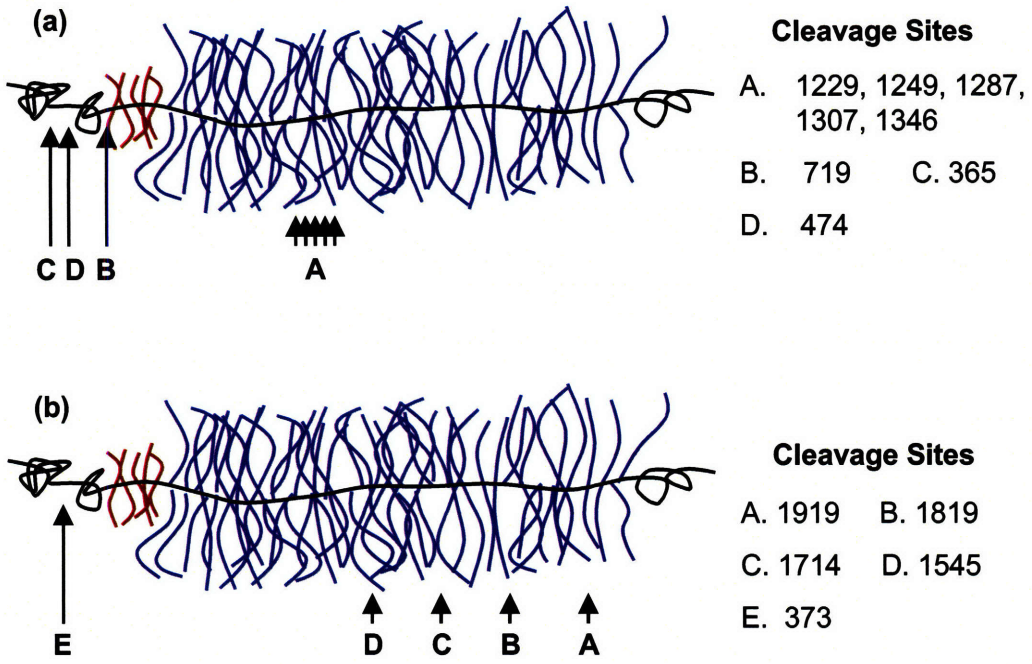

Figure D-1: Schematic of amino acid cleavage sites along aggrecan core protein backbone by (a) m-calpain [119] and (b) aggrecanase (ADAMTS) [132].

properties [119]. Therefore, to quantify the effects and kinetics of aggrecan cleavage by m-calpain on the nanomechanical properties of aggrecan *in vitro*, and to understand the relationship between the nanomechanical properties of enzymatically degraded aggrecan and essentially the effects on cartilage tissue mechanical properties, we measured the change of aggrecan compressive nanomechanical properties during m-calpain digestion via atomic force microscopy (AFM).

D.2 Methods

Purified mature bovine nasal (MN) aggrecan was chemically end-functionalized with thiol-groups. Micropatterned gold-coated substrate with end-grafted MN aggrecan and hydroxyl-functionalized self-assembled monolayer (OH-SAM, $HS(CH_2)_{11}OH$, 11-mecaptouethanol, Aldrich, St. Louis, MO) was formed via microcontact printing [163], as described previously [27]. Atomic force microscopy related techniques were

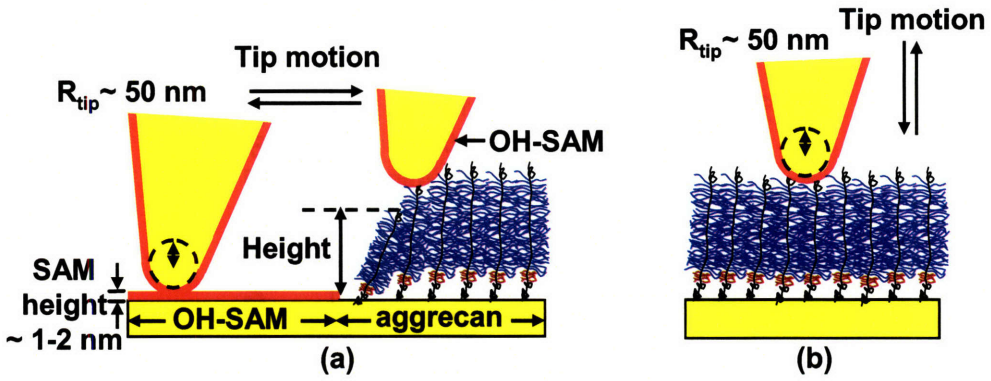

Figure D-2: (a) Schematic of contact mode atomic force microscopy (AFM) to measure the aggrecan layer height at different applied normal force using an OH-SAM functionalized nanosized probe tip (end-radius $R_{tip} \sim 50$ nm, nominal spring constant $k \sim 0.06$ N/m) on an OH-SAM and aggrecan patterned substrate made via microcontact printing. (b) Schematic of force versus separation distance between the OH-SAM tip and end-attached aggrecan layer via high resolution force spectroscopy (HRFS).

then applied to monitor the degradation of end-attached aggrecan layer in the presence of m-calpain. Before the addition of m-calpain, aggrecan height as a function of applied normal force was measured via contact mode AFM and force-separation distance curves were measured via high resolution force spectroscopy (HRFS) at ionic strength (IS) = 0.001 M NaCl aqueous solution, pH $\sim$ 5.6, using an OH-SAM functionalized standard nanosized probe tip ($R_{tip} \sim 50$ nm, NP tip D, silicon nitride, V-shaped cantilever, nominal spring constant $k \sim 0.06$ N/m, Veeco, Santa Barbara, CA), Figure D-2, under which condition, the electrostatic repulsion, and hence aggrecan compressive stiffness is the strongest [27, 28]. The sample was then immersed in the mixed buffer solution containing 110 mM imidazole, 5 mM 2-mercaptoethanol and 1 mM ethylene glycol tetraacetic acid (EGTA) and 7 mM of calcium chloride (IS $\sim$ 0.15 M, pH $\sim$ 7.5) [119] and measured in the same fashion of contact mo de AFM imaging and HRFS force-distance curves before addition of m-calpain. After the AFM measurement, 0.4 nM m-calpain in the same buffer solution was added at room temperature and the change of HRFS force-distance curve profile was monitored up to 60 minutes after the addition of m-calpain. After the m-calpain digestion, ag-

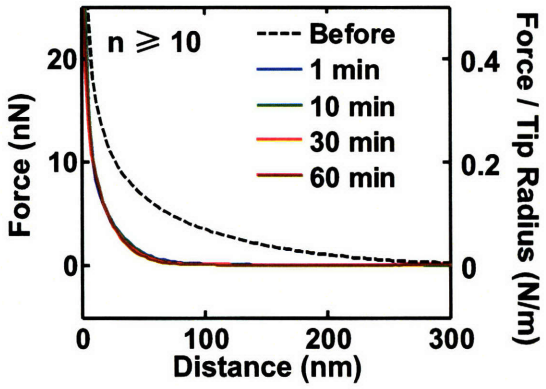

Figure D-3: Force versus separation distance between an OH-SAM functionalized probe tip ($R_{tip} \sim 50$ nm, $k \sim 0.06$ N/m) and end-attached aggrecan layer before and $1 - 60$ minutes after addition of 0.4 nM m-calpain measured in the mixed buffer solution (IS ~ 0.15 M, pH ~ 7.5).

grecan height was measured via contact mode AFM in both the mixed buffer solution and 0.001 M NaCl solution to compare with the height and normal force profiles before the degradation. The same experiment was also performed in 0.15 M phosphate buffered saline (PBS).

D.3 Results

In the mixed buffer solution, as well as 0.15 M PBS solution, da quick drop of magnitude in the repulsive force was observed (< 1 minute after addition of m-calpain), which then remained constant with increasing incubation time, Figure D-3, suggesting the completion of cleavage within 1 minute. The height of the end-attached aggrecan layer was measured at applied normal force $F \sim 3$ nN in the mixed buffered solution before, 1 minute and 60 minutes after adding m-calpain via contact mode AFM. A more than 60% drop of aggrecan layer height was observed 1 minute after the addition of m-calpain, and there is no significant change between 1 and 60 minutes of aggrecan height, Figure D-4a, consistent with the HRFS force measurement. A homogeneous degrade of aggrecan layer height was observed after 60 minutes of digestion along the whole hexagonal pattern, Figure D-4b. Aggrecan compressive stiffness was observed

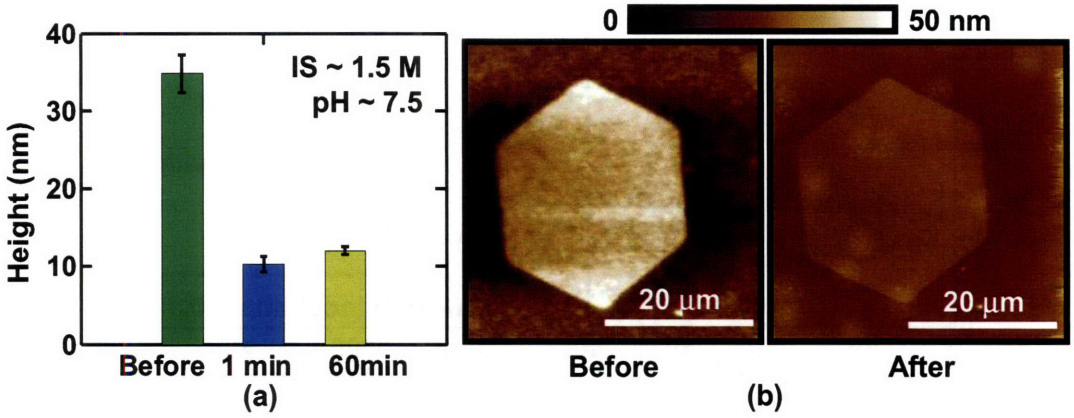

Figure D-4: (a) Aggrecan layer height measured solution by an OH-SAM functionalized probe tip ($R_{tip} \sim 50$ nm, $k \sim 0.06$ N/m) on the OH-SAM and aggrecan micropatterned substrate measured at $F \sim 3$ nN applied normal force via contact mode AFM, before and after the addition of 0.4 nM m-calpain in the mixed buffer. (b) Height image of the micropatterned substrate, where end-attached aggrecan is inside the hexagonal pattern and OH-SAM outside, measured before and 60 minutes after the addition of 0.4 nM m-calpain in the mixed buffered solution (IS $\sim$ 0.15 M, pH $\sim$ 7.5).

to degrade at different applied normal force in 0.001 M NaCl solution, Figure D-5a. Interestingly, stronger repulsion force was still observed in 0.001 M NaCl solution compared to the mixed buffer solution, IS $\sim$ 0.1 M, Figure D-5b.

D.4 Discussion

After the depletion, aggrecan uncompressed layer height is $\sim$ 40 nm at 0.001 M IS, Figure D-5a, indicating that the aggrecan layer is not fully degraded. Based on the known cleavage sites of m-calpain along aggrecan core protein, Figure D-1a, the cleavage could most likely occur within the CS domain (sites A) in this monolayer configuration, possibly due to the steric effect that prevents the molecular contact of m-calpain to other sites near the gold-coated substrate, Figure D-6. This hypothesis is further supported by the observation that a larger repulsion force observed at 0.001 M than at 0.15 M IS, Figure D-5b, suggesting the presence of electrostatic repulsion, hence GAG side chains, on aggrecan after the digestion. As aggrecan is attached

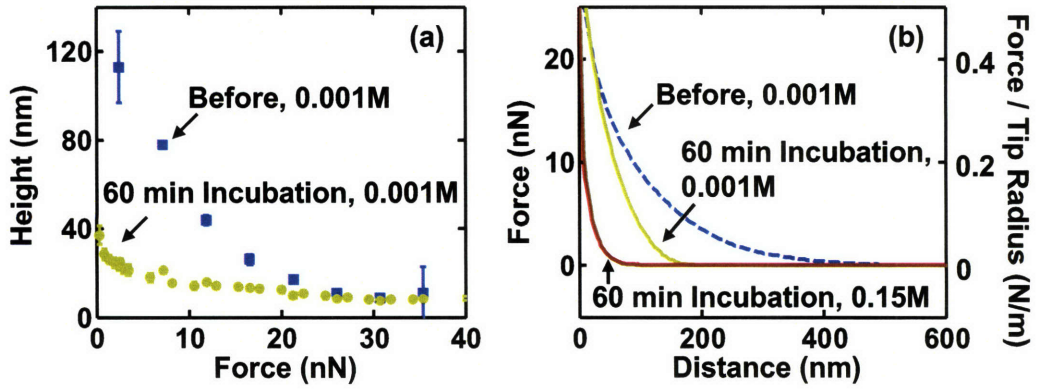

Figure D-5: (a) Aggrecan layer height versus applied normal force by an OH-SAM functionalized probe tip ($R_{tip} \sim 50$ nm, $k \sim 0.06$ N/m) on the OH-SAM and aggrecan micropatterned substrate measured via contact mode AFM in 0.001 M NaCl aqueous solution (pH $\sim$ 5.6) before and after the addition of 0.4 nM m-calpain. (b) Comparison of force versus separation distance curves measured by the OH-SAM tip via HRFS in both 0.001 M NaCl aqueous solution (pH $\sim$ 5.6) and the mixed buffer solution (IS $\sim$ 0.15 M, pH $\sim$ 7.5).

on the gold substrate via its N-terminal, in a similar fashion to its end-anchorage on hyaluronan to form the proteoglycan aggregate *in vivo*, the > 60% reduction of aggrecan layer height and repulsion force at near physiological IS (0.15 M, Figures D-3,D-4) can contribute to the deterioration of cartilage mechanical properties during aggrecan enzymatic digestion *in vivo*.

By comparing to the other systems conducting aggrecan enzymatic degradation, a much quicker digestion by m-calpain was observed here. For example, in cartilage plugs, it takes 8 hours for $\sim$ 50% aggrecan to degrade in cartilage plugs by aggrecanase-1 (ADAMTS-4) [48]; in a 200 μL vial, digesion of aggrecan solution occurs within less than 30 minutes by m-calpain [119]. The much quicker homogeneous digestion (Figure D-4b) observed along the hexagonal end-attached aggrecan layer could be due to smaller diffusion lengths using end-attached aggrecan layer compared to the aggrecan solution or aggrecan entrapped in the collagen network in cartilage. The decreased time for force/height is likely due to a diffusion-controlled reaction mechanism. Ongoing studies using lower m-calpain concentration would facilitate to understand the digestion kinetics in further details.

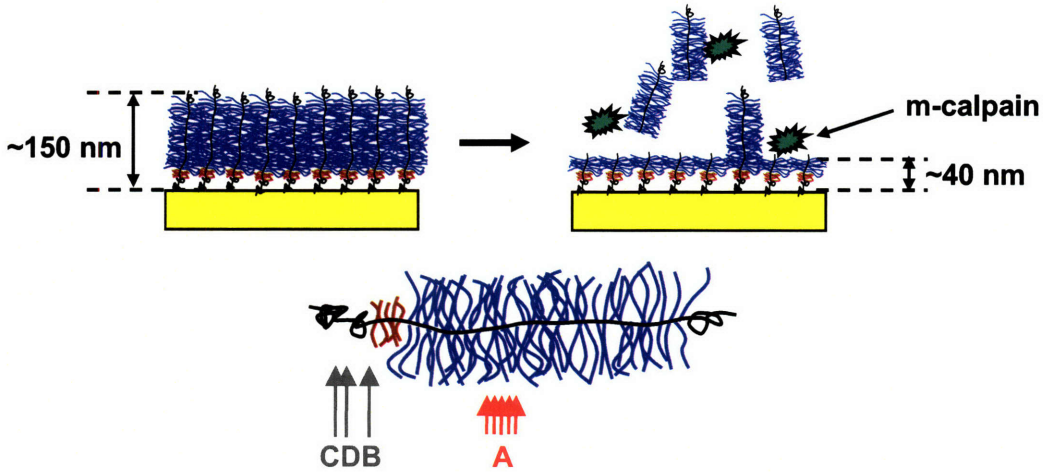

Figure D-6: Schematic of the suggested m-calpain cleavage sites (sites A) along its core protein backbone in this experimental system, where the access of sites B - D at the bottom of the layer could be prevented by the steric effects.

D.5 Conclusions

The methodology presented in this study using microcontact printing in conjunction with AFM allows for quantifying the kinetics of enzymatic degradation of nanomechanical properties of aggrecan. Aggrecan digestion by m-calpain occurs predominantly in the CS domain, and results in a more than 60% reduction of electrostatic repulsion. The digestion of m-calpain is in a manner similar to that expected from aggrecanase (ADAMTS-4,5). This method could hence be applied to other enzymes, e.g. ADAMTS, matrix metalloproteinase (MMP) families, to probe the degradation of aggrecan and its effect on tissue post-injury or with osteoarthritis.

Appendix E

Ionic Strength Dependence of Cartilage Nanoindentation Properties

E.1 Introduction

Articular cartilage functions as the load bearing tissue between joints during motion. The extracellular matrix of cartilage is mainly composed of water, solid type II collagen network and the proteoglycasn motif. Aggrecan, the most abundant proteoglycan, has a "bottle-brush" like architecture, with densely-packed highly negatively charged glycosaminoglycan (GAG) side chains along its core protein backbone [65, 110]. The electrostatic repulsion between GAG chains is known to contribute $\sim$ 50% of cartilage compressive tissue modulus [14, 37]. Besides, the aggrecan aggregate formed via end-attachment of aggrecan on hyaluronan protects the type II collagen matrix from mechanical overload [67] as well as enzymatic digestion [125]. In this study, nanoindentation was performed on both untreated and PG digested cartilage disks in NaCl aqueous solutions at different ionic strengths (IS) to study the electrostatic contribution to cartilage nanoscale mechanical properties.

E.2 Methods

Cartilage disks (9 mm diameter $\times \sim 0.5$ mm thickness) were harvested from the middle/deep zone of femoropatellar groove of $1-2$ weeks old bovine calves by microtoming and maintained in 0.15 M sterile phosphate buffered saline (PBS, without Mg^{2+}, Ca^{2+}). Proteoglycan-depleted cartilage disks were prepared by digestion in 1 mg/mL trypsin (0.15 M NaCl, 0.05 M Na_3PO_4, pH $\sim$ 7.2), and 0.1 U chondroitinase ABC (0.15 M NaCl, 0.05 M Tris-HCl, pH $\sim$ 8.0), each for 24 hours at 37°C, which resulted in $>$ 95% digestion of matrix proteoglycan. Nanoindentation was performed on both untreated and PG-depleted disks by a colloidal probe tip (end-radius $R_{tip} \sim 2.5$ μm, nominal spring constant $k \sim 0.58$ N/m, BioForce Nanosciences, IA) functionalized with a neutral hydroxyl-terminated self-assembled monolayer (OH-SAM, $HS(CH_2)_{11}OH$, 11-mecaptoudecanol, Aldrich, St. Louis, MO) [27] using a Nanoscope IV Multimode atomic force microscope (AFM) with a PicoForce scanner. The upper 75% of the indentation force curves were fit with the Hertz model to calculate its effective stiffness [116],

$$F = \frac{4}{3}\frac{E}{(1-\nu^2)}R^{1/2}(D-D_f)^{3/2}. \tag{E.1}$$

E.3 Results and Discussion

Typical nonlinear indentation force curves were observed for both untreated and PG-depleted cartilage disks in NaCl solutions, Figure E-1a,E-2a, consistent with previous studies on cartilage nanoindentation [143, 86]. A deterioration of cartilage stiffness was observed on the nontreated disks as increasing IS, Figure E-1b. This is possibly due to the screening of electrostatic repulsion along the GAG side chains, and consistent with the previous observation on cartilage tissue mechanics [37] and aggrecan compressive nanomechanics [27, 28]. The effective stiffness experienced a $\sim$ 25% decrease when IS was increased from 0.001 to 0.1 M, and a further $\sim$ 50% drop as IS increased to 1.0 M. The less marked effect of IS on stiffness from 0.001 to 0.1 M could

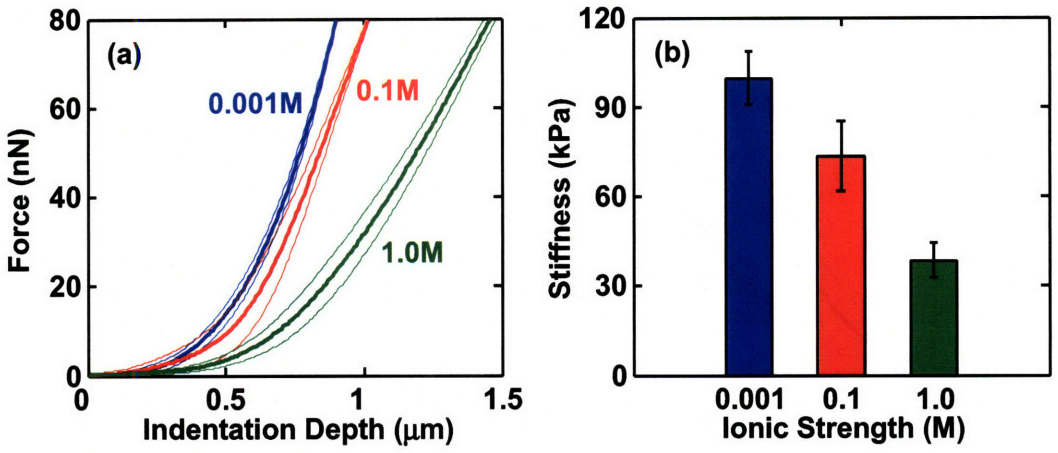

Figure E-1: (a) Force versus indentation depth on untreated cartilage disk in NaCl aqueous solutions at $0.001 - 1.0$ M IS using an OH-SAM functionalized colloidal tip ($R_{tip} \sim 2.5$ μm, $k \sim 0.58$ N/m), mean $\pm$ SEM of mean values at each indentation position, $n \geq 3$ different positions, 10 repeated measurements at each position. (b) Estimated effective stiffness at different IS using Eq.E.1 mean $\pm$ SEM, $n \geq 3$. There is significant effect of IS on E (one-way ANOVA, $p < 0.01$).

be due to the dominance of electrostatic repulsion in this IS range. The GAG spacing is $\sim 2-4$ nm along the aggrecan backbone, and at 1.0 M IS, where Debye length κ^{-1} is approximately 1 nm, hence, the electrostatic component plays an important role in determining cartilage mechanics at 0.1 M and lower (0.001 M, $\kappa^{-1} \sim 10$ nm) IS. At 1.0 M IS, $\kappa^{-1} \sim 0.3$ nm, the GAG-GAG electrostatic repulsion is almost completed shielded by the mobile ions, and hence a more marked drop was observed on the measured effective stiffness.

A significant effect was observed on the PG-depleted cartilage sample, Figure E-2b. There is also a $\sim 50\%$ decrease of the mean value of the effective stiffness from 0.001 to 0.1 M IS. This drop could be due to the change of the type II collagen conformation and structure as changing NaCl concentration, though the net charge of the collagen matrix is approximately zero at the tested pH [99]. Possible collagen degradation could also occur at higher IS in the absence of the PG content. This hypothesis is further supported by the observation of collagen degradation at 1.0 M IS, Figure E-3. Hence, at high salt concentration, the collagen fibrils could undergo

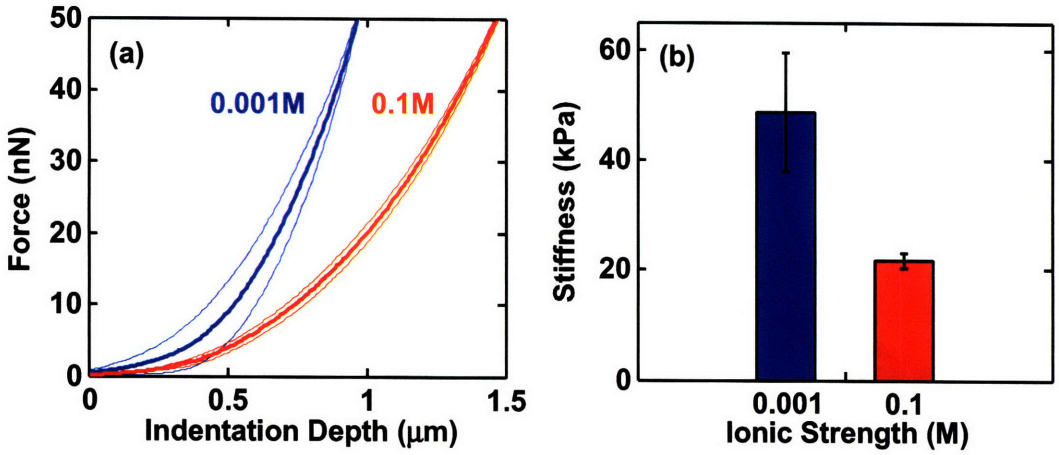

Figure E-2: (a) Force versus indentation depth on PG-depleted cartilage disk in NaCl aqueous solutions at $0.001 - 0.1$ M IS using an OH-SAM functionalized colloidal tip ($R_{tip} \sim 2.5$ μm, $k \sim 0.58$ N/m), mean $\pm$ SEM of mean values at each indentation position, $n \geq 3$ different positions, 10 repeated measurements at each position. (b) Estimated effective stiffness at different IS using Eq.E.1 mean $\pm$ SEM, $n \geq 3$. The stiffness E at 0.001 M IS is significantl higher than that at 0.1 M IS (one-tailed independent student's t-test, $p < 0.05$).

defibrillazation or degradation in the absence of the PG protection, and hence, leads to the deterioration of the mechanical properties.

E.4 Conclusions

In this study, the ionic strength dependence of the nanoindentation behavior of untreated and PG-depleted cartilage was studied. Screening of electrostatics by increasing IS leads to a decrease of the mechanical stiffness, consistent with previous reports [37, 27, 28]. In the absence of PG content, the collagen network could undergo degradation at higher IS, hence the mechanical properties also changes when changing IS. This study further supports that the electrostatic repulsion along the PG motif is an essential feature that affects the cartilage structural integrity as well as its mechanical function.

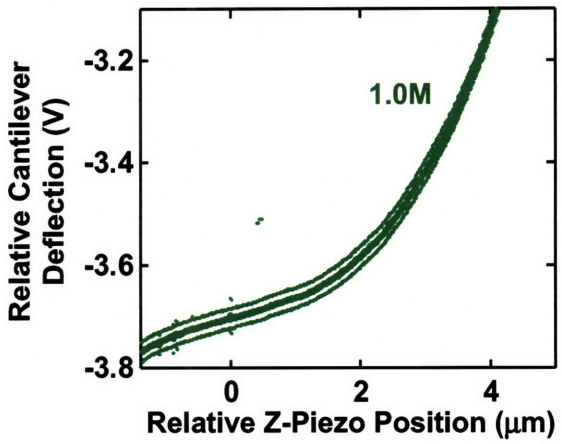

Figure E-3: Relative cantilever deflection (V) versus z-piezo position (μm) taken at one indentation position on PG-depleted cartilage disk in 1.0 M NaCl solution, mean $\pm$ SEM for 10 repeated measurements.

Appendix F

Dynamic Oscillatory Experiment Calibration

During each of the one-minute ramp-and-hold cartilage deformation,(the z-piezo displacement (nm) and cantilever deflection (V) was captured as a function of time in the "script mode" of Version 6.13 of the Nanoscope IV AFM software (Veeco, Santa Barbara, CA). The cantilever deflection signal was then converted to the units of nm by multiplying the deflection sensitivity (nm/V), measured by probing the probe tip on a hard substrate, e.g. mica. In the range of applied frequencies, $f = 1 - 1000$ Hz, the data acquisition frequency f_a was set to be 1 kHz for $f < 100$ Hz, and 10 kHz for $f \geq 100$ Hz. At each position, one ramp-and-hold experiment was performed for each applied frequency and z-piezo displacement amplitude. Upon each sampling, approximately ten cycles of the sinusoidal waves from each of the two time series data were analyzed to quantify the amplitude and phase angle difference between them. The starting point of the ten cycles was randomly picked in the steady-state time range, 35 seconds after loading and more than ten cycles before unloading. To eliminate the error from external noise and random data picking, this sampling procedure was repeated for 50 times for the control experiment on mica at each frequency.

Upon each sampling, both series were offset by their mean values, and least squares nonlinear regression was first applied to the cantilever deflection data to fit the equa-

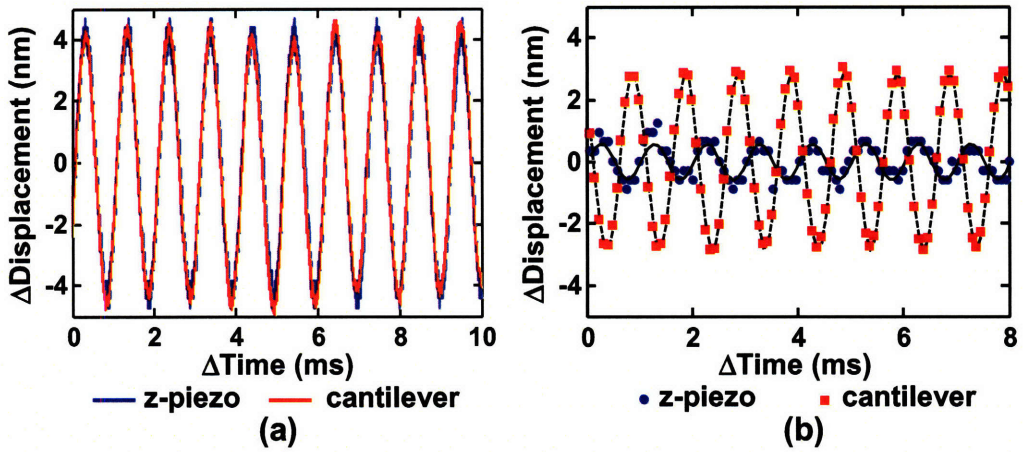

Figure F-1: Illustration of the raw data of z-piezo and cantilever displacement as a function of time upon one sampling along the time series of data at applied deformation frequency (a) $f = 1$ Hz, (b) $f = 1000$ Hz.

tion,

$$C_0 = C_{a0} \sin(2\pi f t + \psi_0) \tag{F.1}$$

where C_0 and t are the experimental data of cantilever deflection (nm) and time (sec), frequency f, amplitude C_{a0} and initial phase angle ψ_0 are fitting parameters (the subscript "0" indicates the fitting obtained from the control sample). The initial values of fitting parameters, C_{a0} was set to be the maximum value of deflection, f the frequency preset on the sinusoidal wave generator, and ψ_0 the arcsin value of the first deflection data point. The purpose of fitting frequency f, instead of using the preset value, is because the actual data acquisition frequency is less than the nominal value ($\sim 0.8 - 0.9\times$ nominal value). Hence, by setting the time data as $1/f_a$ does not represent the true time interval between each pair of adjacent data points along the time series. It should be noted that the fitted value $\hat{f}$ does not represent the actual deformation frequency, which should equal the preset value. After achieving the fitted values $\hat{f}$, $\hat{C}_0$ and $\hat{\psi}$, nonlinear regression was applied to the z-piezo displacement data,

$$Z_0 = Z_{a0} \sin(2\pi \hat{f} t + \phi_0) \tag{F.2}$$

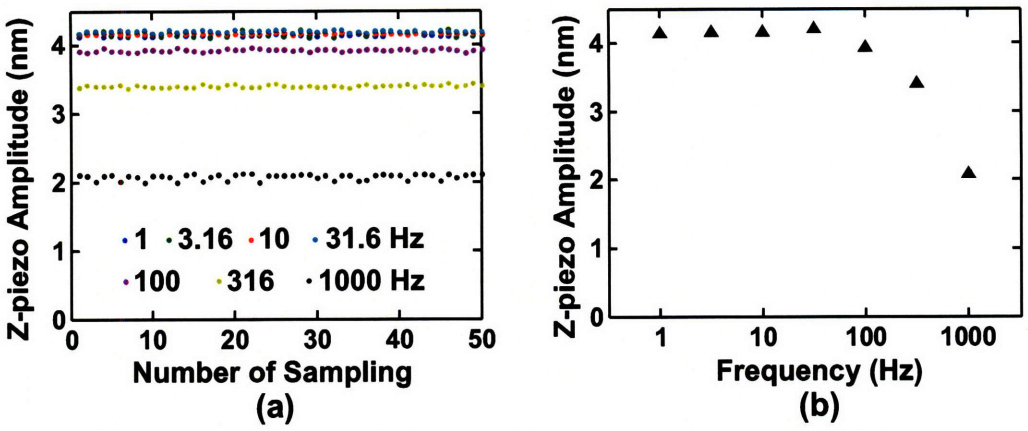

Figure F-2: (a) Sampling of z-piezo displacement amplitude at different applied frequencies at one position taken by an OH-SAM functionalized colloidal probe ($R \sim 2.5$ μm, $k \sim 0.58$ N/m) on mica substrate, where the z-piezo displacement amplitude was estimated via the displacement amplitude of the cantilever. Each data point represents one sampling at a random position of the time series 35 seconds after loading. (b) The mean values of z-piezo displacement amplitude ($\sim 2-4$ nm) in panel (a) as a function of applied frequency, where the SEM of mean is smaller than the size of data.

where Z_0 and t are the experimental data of z-piezo displacement (nm) and time (sec), the initial values of fitting parameters, amplitude Z_{a0} was the maximum value of z-piezo displacement, and ϕ_0 the arcsin value of the first z-piezo data point, and the frequency was fixed at $\hat{f}$ from previous fitting of the deflection data. The reason to fix the frequency at $\hat{f}$ is because the frequency of z-piezo and cantilever displacement equal each other, Figure F-1a, and the z-piezo data is more noisy, especially at higher frequencies, Figure F-1b. Introducing more fitting parameters could lead to non-convergence of the fitting procedure, especially at higher frequencies. As this procedure always result in reasonably good fit for data at frequencies up to 316 Hz ($R^2 > 0.9$ for both cantilever deflection and z-piezo displacement), only the sampling and consequent fits with $R^2 > 0.9$ for the cantilever deflection and $R^2 > 0.5$ for the z-piezo displacement data was retained and counted in order to exclude the sampling without a good fit due to large noises at 1000 Hz.

On the mica control sample, the amplitudes of z-piezo and cantilever equal each

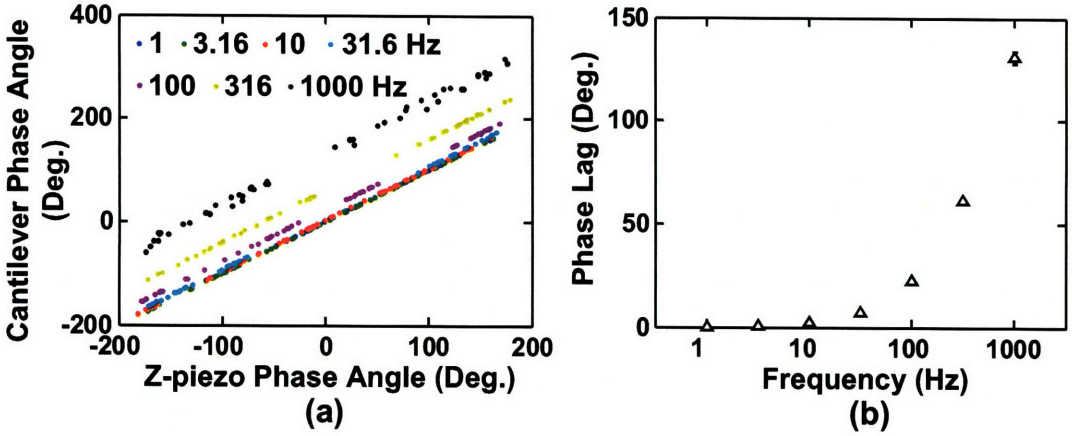

Figure F-3: (a) Sampling of the phase angles from z-piezo and cantilever displacement at different applied frequencies at one position taken by an OH-SAM functionalized colloidal probe tip ($R \sim 2.5$ μm, $k \sim 0.58$ N/m) on mica substrate. Each data point represents one sampling at a random position of the time series 35 seconds after loading. (b) The estimated values of phase difference in panel (a) as a function of applied frequency via least squares linear regression (LSLR), mean $\pm$95% confidence interval of mean.

other at lower frequencies ($<$ 100 Hz), as the mica is elastic and can be regarded as infinitely stiff compared to cartilage or the applied AFM cantilevers. At higher frequencies ($\geq$ 100 Hz), there are significant noises appearing on the z-piezo displacement data, and smaller amplitudes were observed compared to the cantilever deflection data, Figure F-1b. This error is introduced by the data acquisition process of the z-piezo movement at high frequencies. In addition, there is significant phase difference between the z-piezo and cantilever deflection measured on the mica sample, possibly due to the data acquisition of cantilever and z-piezo movement. Hence, the actual amplitudes of z-piezo displacement were calibrated as the amplitude of cantilever deflection $\hat{C}_0$, Figure F-2. The phase angle difference at each frequency was calculated as the maximum likelihood estimator via least squares linear regression along the 50 pairs of initial phase angles, $\hat{\psi}$ and $\hat{\phi}$, Figure F-3. The small standard error of mean values in Figure F-2b and F-3b suggested this repetition procedure of sampling has eliminated the random errors by sampling at different time spots. As the phase differences measured on the control sample, due to the data acquisition

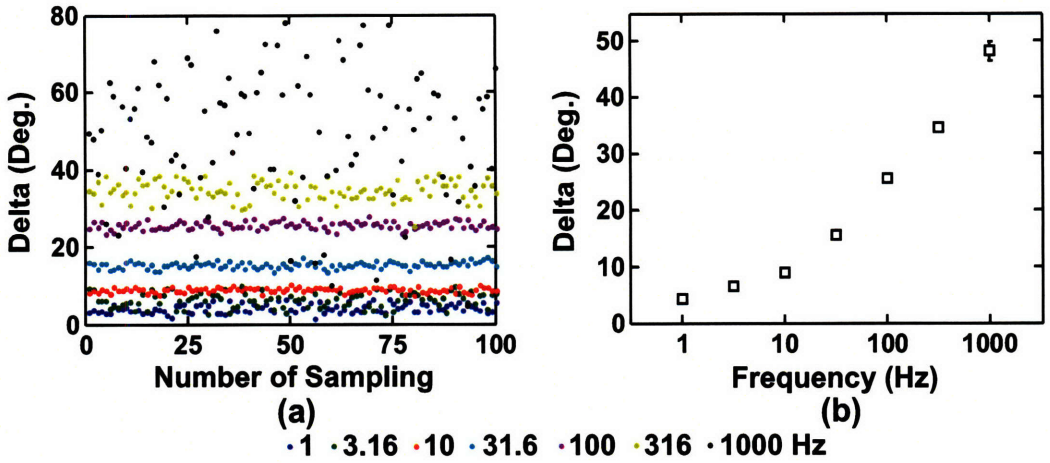

Figure F-4: (a) Sampling of phase lag of deformation to the applied force of untreated cartilage sample (thickness ~ 0.5 mm) at one position taken by an OH-SAM functionalized colloidal probe ($R \sim 2.5$ μm, $k \sim 0.58$ N/m) at $\sim 2-4$ nm z-piezo displacement amplitude. Each data point represents one sampling at a random position of the time series 35 seconds after loanding. (b) The mean values of phase lag of untreated cartilage in panel (a) as a function of applied frequency, mean $\pm$ SEM of mean.

process and possibly hydrodynamic effects instead of the material properties of mica, were corrected when analyzing the data on cartilage.

The same data analysis procedure was performed on the data obtained on cartilage samples, except that the sampling procedure was repeated for 100 times for each ramp-and-hold experiment. Upon each sampling, the same fitting procedure was also performed,

$$C = C_a \sin(2\pi f t + \psi) \tag{F.3}$$

$$Z = Z_a \sin(2\pi \hat{f} t + \phi) \tag{F.4}$$

and two complex numbers could be formed based on the fitting after correction obtained from the control experiment: the z-piezo amplitude was used as what obtained in Eq. F.1 instead of Z_a, and the phase angle difference on control sample was cor-

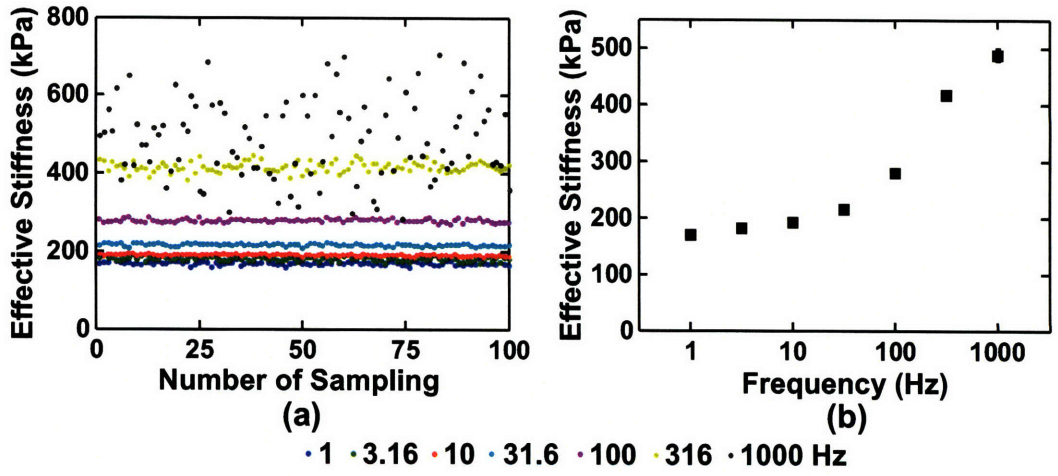

Figure F-5: (a) Sampling of effective stiffness of untreated cartilage sample (thickness ~ 0.5 mm) at one position taken by an OH-SAM functionalized colloidal probe ($R \sim 2.5$ μm, $k \sim 0.58$ N/m) at $\sim 2-4$ nm z-piezo displacement amplitude via Hertz model. Each data point represents one sampling at a random position of the time series 35 seconds after loading. (b) The mean values of effective stiffness of untreated cartilage in panel (a) as a function of applied frequency, mean $\pm$ SEM of mean.

rected,

$$C_c = \hat{C}_a(\cos\psi + i\sin\psi) \tag{F.5}$$

$$Z_c = \hat{Z}_a[\cos(\hat{\phi} + \hat{\psi}_0 - \hat{\phi}_0) + i\sin(\hat{\phi} + \hat{\psi}_0 - \hat{\phi}_0)] \tag{F.6}$$

The corresponding complex numbers for cartilage sample deformation D_c and force F_c were calculated as,

$$D_c = Z_c - C_c \tag{F.7}$$

$$F_c = C_c \times k \tag{F.8}$$

where k is the cantilever spring constant (nN/nm), hence, the phase lag was calculated as the angle difference between these two complex numbers (Figure F-4), and the modes of these two numbers were taken the magnitude of deformation and force, respectively. Hertz model for oscillatory infinitesimal deformation was used to

estimate the corresponding effective stiffness (Figure F-5).

Appendix G

Nanomechanics of Cartilage on Intact Murine Knee Joints

G.1 Introduction

Cartilage is the load bearing avascular connective tissue covering the bony ends of the joints, and sustains a complex combination of tensile, compressive and shear loads during joint motion [55]. Unfortunately, the repair capability of cartilage is poor, and osteoarthritis (OA), the most common joint disease, causes irreversible degradation of cartilage mechanical properties and tissue function [106]. The intrinsic biomechanical properties of cartilage, and the effects of age, disease, diet and genetics have been investigated using a variety of animal models [106, 153]. The mouse model has received increased attention during the past decade because of the ability to modify specific tissue development and functional properties using gene knock-out and related gene-altering technologies [77]. Murine cartilage has been studied at the macroscopic tissue level to quantify the effects of certain gene knockouts on biomechanical properties (e.g., via osmotic swelling behavior) [80, 166]. To our knowledge, there are no published reports on measurement and quantification of micro- and nanoscale biomechanical properties of murine joint cartilage, which may provide important molecular level insights concerning the consequences of specific disease processes. The main challenge has been the relatively small cartilage tissue dimensions ($\sim$ 1 mm wide,

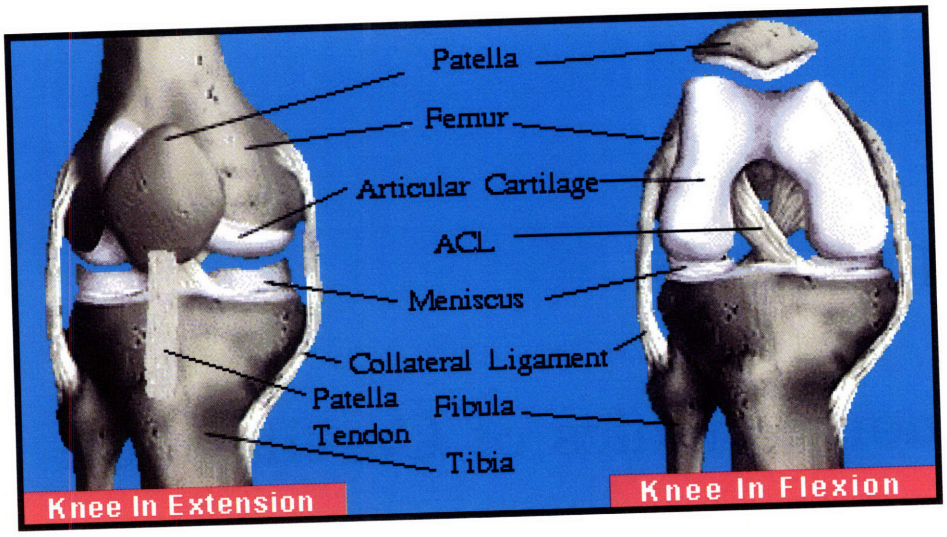

Figure G-1: Illustration of mouse knee joint in tension and flexion (Courtesy of Dr. A. Plaas).

$\sim$ 100 μm thick). Hence, in this study, the nanomechanical properties of mouse cartilage and its mechanical function change upon tissue remodeling were quantified using atomic force microscope (AFM)-based nanoindentation techniques.

G.2 Methods

C57Bl/8 male 9-week old mice were divided into control and treatment groups. The treatment group ($n = 5$) received injections of 250 ng TGF-β in 6 μL BSA into right knees on alternate days for a total of two injections. The controls ($n = 3$) received no injections. Seven days after the injections, the mice were euthanatized and hind limbs were harvested. The mouse knee joints were then dissected to separate other joint tissues (tendon, ACL, etc.) from tibia and condyle articular cartilage in the presence of protease inhibitors. The dissection protocol is to cut (1) the patella tendon near the tibia tubercle, (2) collateral ligaments, (3) ACL and PCL, and (4) plantar flexor muscles from the femur and semimembranosus (Figure G-1). Then we pull the femur superiorly away from the tibia and cut other tissues that are attached.

Constant displacement rate-nanoindentation was performed on the both normal

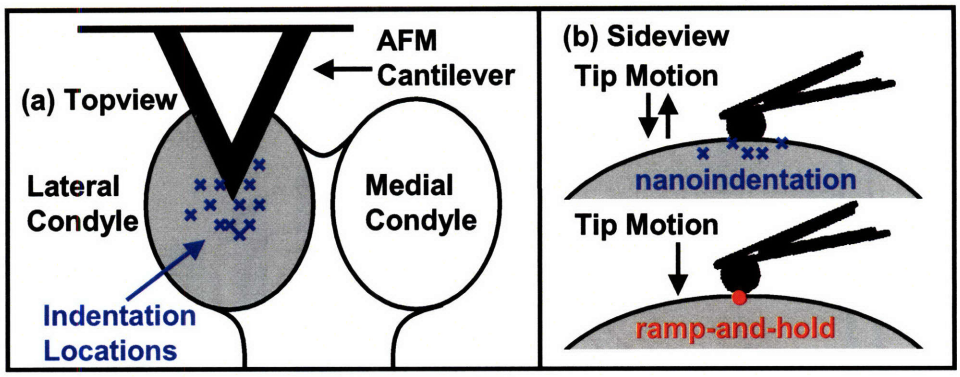

Figure G-2: Schematic of AFM-nanoindentation and ramp-and-hold stress relaxation measurement on mouse lateral condyle knee cartilage using an OH-SAM functionalized colloidal probe tip (end-radius $R_{tip} \sim 2.5$ μm, nominal spring constant $k \sim 0.58$ N/m).

and TGF-β treated mouse lateral condyle cartilage samples via a colloidal probe tip (end-radius $R_{tip} \sim 2.5$ μm, nominal spring constant $k \sim 0.58$ N/m, displacement rate ~ 1 μm/s) functionalized with a neutral hydroxyl self-assembled monolayer (OH-SAM, 11-mecaptoundecanol, $HS(CH_2)_{11}OH$, Aldrich, St Louis, MO), Figure G-2. Tests were done in the fully wet state (0.15 M phosphate buffered saline in the presence of protease inhibitors to prevent enzymatic degradation of cartilage matrix macromolecules). At least 10 different indentation locations were tested on each joint. The Hertz model [84] was applied to calculate the effective indentation stiffness by taking into account the geometrical factors in the indentation force range $\sim 40 - 50$ nN.

$$F = \frac{4}{3}\frac{E}{(1-\nu^2)}R^{1/2}D^{3/2}. \tag{G.1}$$

The time-dependent behavior of the mouse cartilage was assessed by applying a ramp-and-hold displacement to ~ 0.2 μm deformation and subsequent measurement of force relaxation as a function of time. Nanoscale dynamic oscillatory experiments were performed by applying a sinusoidal strain to the tissue (via a function generator connected to the AFM z-piezo), using an offset deformation $\sim$ 200 nm and an infinitesimal displacement amplitude ($\sim$ 4 nm) applied over a frequency range $\sim 1-100$ Hz. All the nanomechanical experiments were performed using a Nanoscope IV AFM

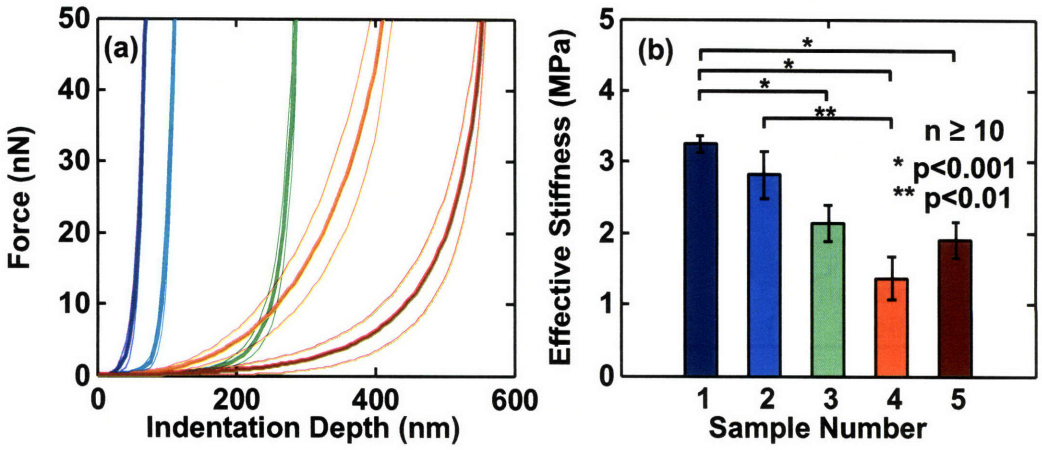

Figure G-3: (a) Force-indentation depth profile on 5 normal murine cartilage samples from 9 weeks old male mouse right knees (C1 – C5) using an OH-SAM functionalized colloidal probe tip ($R_{tip} \sim 2.5$ μm, $k \sim 0.58$ N/m), $n \geq 10$ different locations on each joint was tested (mean $\pm$ SEM), indentation was repeated for 10 times at each location. (b) Estimated indentation stiffness using Hertz model [84] to taken into account the geometrical factors in the indentation force range $\sim 40 - 50$ nN (mean $\pm$ SEM) and two-sample statistical t-test results.

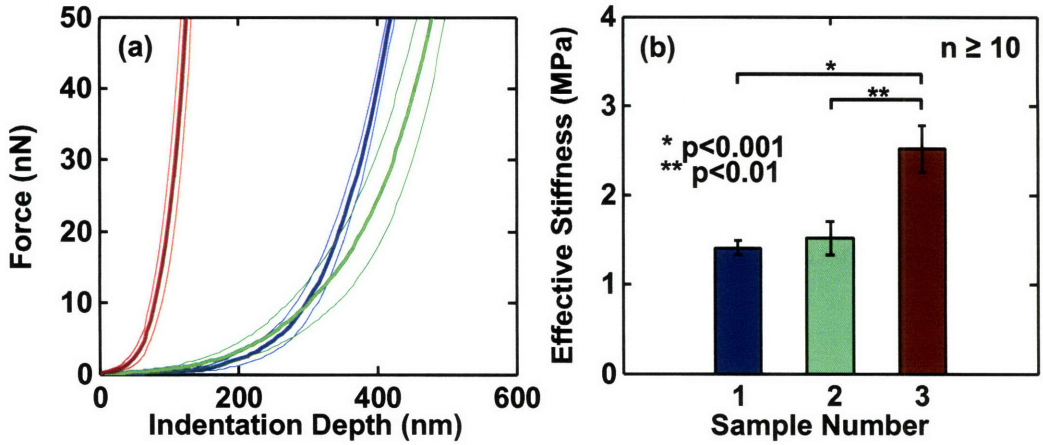

Figure G-4: (a) Force-indentation depth profile on 3 TGF-β treated murine cartilage samples from 9 weeks old male mouse right knees (B1 – B3) using an OH-SAM functionalized colloidal probe tip ($R_{tip} \sim 2.5$ μm, $k \sim 0.58$ N/m), $n \geq 10$ different locations on each joint was tested (mean $\pm$ SEM) indentation was repeated for 10 times at each location. (b) Estimated indentation stiffness using Hertz model [84] to taken into account the geometrical factors in the indentation force range $\sim 40 - 50$ nN (mean $\pm$ SEM) and two-sample statistical t-test results.

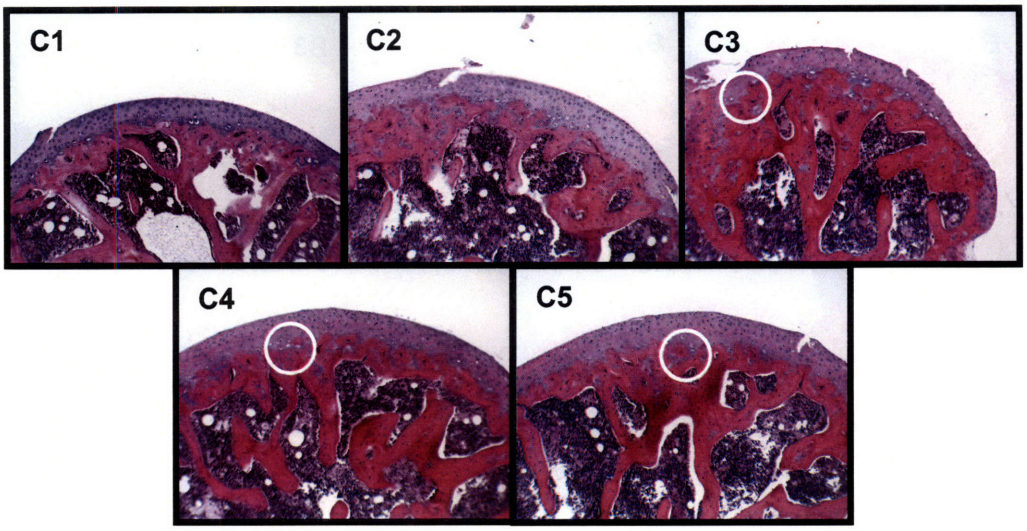

Figure G-5: Histology of right lateral condyles from 5 normal mice samples (Hematoxylin and Eosin stain), a more distinct interface between cartilage and subchondral bone was apparent compared to C3, C4, C5, which showed bone to slightly invaginate into the cartilage layers (highlighted by the white circles).

with a closed z-loop PicoForce scanner (Veeco, Santa Barbara, CA). The 3-element stress-relaxation model was applied to assess the long-time relaxation behavior of the mouse cartilage sample (> 1 second after loading), and the Hertz model for infinitesimal dynamic deformation was applied to calculate the effective dynamic stiffness (for detailed data analysis on oscillatory dynamic loading experiment, see Appendix F). The ramp-and-hold stress relaxation and nanoscale oscillatory dynamic loading experiments were performed on one indentation position of the normal mouse cartilage sample C3, since the deflection signal was always interfered by noise that are larger than the signal itself at other tested positions.

After AFM experiment, the samples were fixed in 10% buffered formalin overnight at room temperature, dehydrated via a series of graded alcohols, then treated with xylene, and infiltrated by paraffin. For histology, 5 mm cut sections were rehydrated, then stained with Hematoxylin and Eosin.

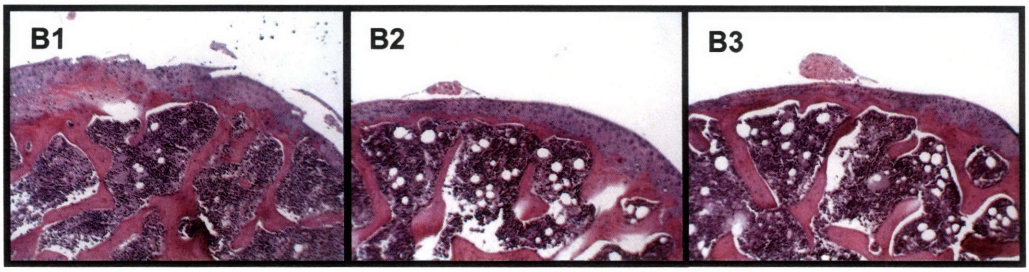

Figure G-6: Histological sections (Hematoxylin and Eosin stain) from lateral condyle of 3 TGF-β treated knee joints. Both cartilage and bone show markedly different appearance compared to normal joints (Figure G-5), with cartilage degradation and significant subchondral bone remodeling in treated samples.

G.3 Results and Discussion

Similar to nanomechanical properties of cartilage reported from other species [32, 143, 86], nonlinear indentation behavior was observed for murine cartilage here as well (Figures G-3a, G-4a). Different nanoindentation responses and stiffness were observed on different indented locations of one sample (Figure G-3b), and on different samples (Figures G-3b, G-4b). Variations in the effective stiffness E measured at different indentation locations could be attributed to the heterogeneity of the murine cartilage, including thickness, proteoglycan content, as well as surface geometry. Within the five tested normal cartilage samples, C1 and C2 showed higher stiffness than C3 – C5 (Figure G-3). Correspondingly, interdigitation of cartilage and its underlying bone was observed for joints C3 – C5 via histology, but not for C1 and C2, Figure G-5. The histology result suggests that cartilage samples C1 and C2 has developed markedly more mature articular cartilage, corresponding to higher stiffness, while C3 – C5 were less developed, Figure G-3b. The mean stiffness of the three TGF-β treated samples, $E_{\text{TGF}-\beta} = 1.8 \pm 0.3$ MPa, was significantly lower than the mean stiffness of the 5 normal samples $E_{\text{normal}} = 2.3 \pm 0.3$ MPa (mean $\pm$ SEM (standard error of means), two-sample t-test $p < 0.03$). As the presence of TGF-β induces cartilage tissue remodeling and reduces the cartilage tissue stiffness, different histology results were observed for the normal and TGF-β treated cartilage samples, Figures G-5,G-6.

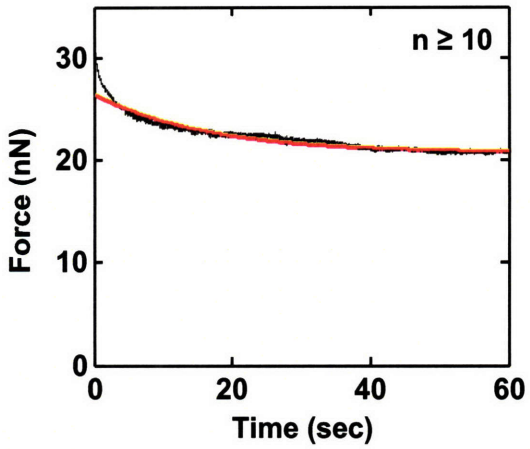

Figure G-7: Stress-relaxation force versus time upon stress relaxation on one indentation position of C3 mouse knee joint cartilage using an OH-SAM functionalized colloidal probe tip ($R_{tip} \sim 2.5$ μm, $k \sim 0.58$ N/m) and the fit using 3-element model with one relaxation time constant by least squares nonlinear regression in the time range > 1 second, where the stress relaxation time constant $\tau = 14.6 \pm 2.3$ s, and equilibrium modulus is 0.75 ± 0.09 MPa.

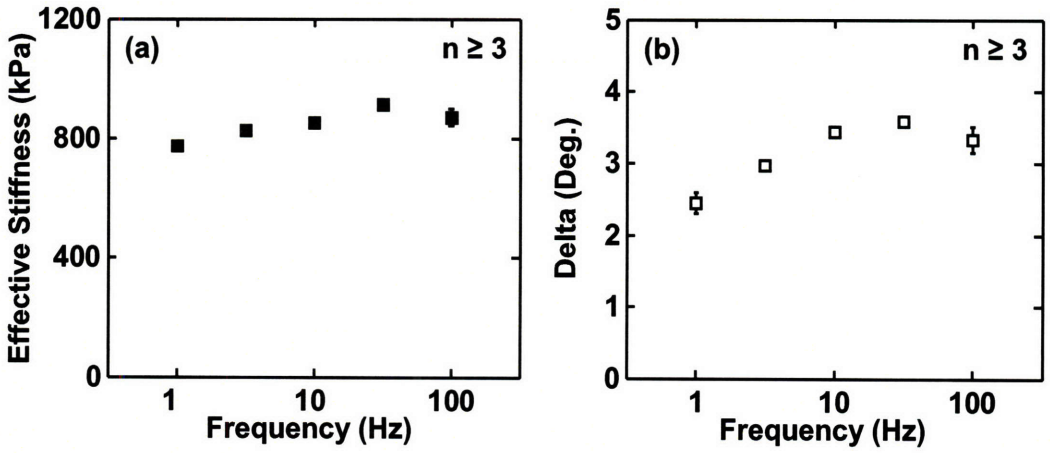

Figure G-8: Estimated (a) dynamic stiffness E and (b) phase lag of deformation to the applied force, on one indentation position of C3 mouse knee joint cartilage measured via OH-SAM functionalized colloidal probe tip ($R_{tip} \sim 2.5$ μm, $k \sim 0.58$ N/m) as a function of frequency ($1 - 100$ Hz) at ~ 1 nm deformation amplitude, estimated via Hertz model [84], mean $\pm$ SEM for 3 repeated measurements.

Force-relaxation tests showed an average characteristic relaxation time constant $\tau = 14.6 \pm 2.3$ s for $n \geq 10$ measurements on the same joint C3, and an equilibrium modulus of 0.75 ± 0.09 MPa, Figure G-7. Dynamic nanomechanical data showed that the dynamic stiffness estimated under the infinitesimal deformation (± 1 nm) using the Hertz model was $\sim$ 0.8 MPa in the tested frequency range of $1 - 100$ Hz, for the same mouse joint (C3), Figure G-8. The deformation frequency has significant effect on both the dynamic stiffness (Figure G-8a) and phase lag (Figure G-8b) between applied displacement and measured force, as tested by one-way analysis of variance (ANOVA). The time-dependence could be due to combined effects of poro- and viscoelasticity: local pressure gradients and the fluid flow through the collagen-proteoglycan ECM under the tip can lead to poroelastic deformation [108], while intrinsic viscoelasticity of the solid matrix may also be important [97]. The frequency dependent behavior observed during nanoscale oscillatory experiments suggests the existence of time-dependent poro/viscoelastic behavior even under the infinitesimal deformation conditions, as manifested by the increase in phase angle.

A significantly quicker stress-relaxation time constant was observed for the murine cartilage, comparing to the calf knee joint cartilage measured ($\tau = 22.1 \pm 0.9$ s, Chapter 6). The measured dynamic stiffness is markedly higher than that of the bovine cartilage, with smaller phase lag, under the same experimental conditions (Chapter 6). In addition, the frequency dependences of E and phase lag are both less significant than that of the bovine cartilage, suggesting the elastic component is more dominant for the murine cartilage deformation mechanism. These species difference may be due to the different stress that the knee joint sustains in murine and bovine cartilage.

G.4 Conclusions

The methodology presented in this study suggests a suitable way to quantify and compare the nanomechanical properties of normal and diseased or biologically (e.g., genetically) modified mouse cartilage. Ongoing studies are to compare normal murine

cartilage to that from TGF-β-stimulated remodeling and inflammation, as well as matrix-specific knock-outs to explore specific molecular pathways associated with osteoarthritis-like disease.

Appendix H

Experimental Protocols

H.1 Thiol-functionalization of Aggrecan

1. Dissolve ~ 6 mg of dithiobis(sulfosuccinimidyl propionate) (DTSSP) in 0.5 mL deionized (DI) water, and ~ 3 mg of dithiothreitol (DTT) in 1 mL DI water.

2. Add ~ 100 μL of DTSSP solution into 1 mL of 2 mg/mL aggrecan aqueous solution, and incubate for 1 hour, allowing the $> 100\times$ excess DTSSP to react with aggrecan and form disulfide bonds at the N-terminal of aggrecan core protein.

3. Add $\sim 150 - 200$ μL of DTT solution, and incubate for 1 hour, allowing the $> 100\times$ excess DTT to reduce the disulfide bonds to thiol bonds.

4. Suspend the solution in a molecular filter with 10,000 molecular weight cut, and dilute the total volume to ~ 2 mL using DI water, and spin at $3,500 - 4,000$ rpm for $5 - 6$ hours to separate the aggrecan from other reactants.

5. Flip the filter and spin at the same speed for 30 minutes, hence allow aggrecan to aggregate at the bottom of the vile.

6. Dilute the aggrecan concentration to 1 mg/mL, store the solution in $-80°$C freezer.

H.2 Preparation of Micropatterned Aggrecan End-attached Substrate

1. Prepare a poly(dimethylsiloxane) (PDMS) stamp with $\sim$ 10 μm sized patterns, for example, hexagonal holes with 10 μm side length.

2. Immerse the stamp in 3 mM 11-mecaptoundecanol ($HS(CH_2)_{11}OH$, OH-SAM) ethanol solution for at least 30 minutes, with the patterned side facing up.

3. Clean 1 cm $\times$ 1 cm gold-coated silicon substrate with fresh Piranha solution (volume ratio 3:1 mixture of 98% H_2SO_4 and 30% H_2O_2, prepared by slowly adding 6 mL 98% H_2SO_4 to 2 mL 30% H_2O_2) for $15 - 20$ minutes.

4. Taken the stamp out of the OH-SAM solution, and dried it on a filter paper in air for $\sim$ 1 minute, with the patterned side facing up.

5. Thoroughly rinse the cleaned gold-coated substrate with DI water, and blow it dry with the nitrogen gun.

6. Bring the patterned side of PDMS stamp in contact with the cleaned substrate for $0.5 - 2$ minutes, allowing the formation of thiol-gold bonds between gold and the OH-SAM in the region outside the hexagonal patterns.

7. Thoroughly rinse the substrate with ethanol, and dried with the nitrogen gun. Can also check the formation of the SAM layer via DI water to see the change of surface hydrophobicity.

8. Drop 50 μL 1 mg/mL thiol-functionalized aggrecan aqueous solution on the substrate, allowing the interaction for $\sim$ 48 hours in a half-airtight chamber.

9. Thoroughly rinse the substrate with DI water to remove unreacted aggrecan, the region inside the hexagonal patterns should be filled with end-attached aggrecan macromolecules.

H.3 Aggrecan Nanomechanics Experiment – Compression, Shear and Self-Adhesion

1. Setup the Nanoscope IV AFM with the PicoForce piezo, mount the probe tip on the glass fluid tip holder, drop ~ 30 μL solution (for example, 0.001 M NaCl) on island mounted with the tip.

2. Drop ~ 100 μL solution on the aggrecan substrate, bring the probe tip close to the substrate.

3. Wait for the system to equilibrate, usually $5 - 10$ min in air and $15 - 20$ min in fluid.

4. Maximize the sum signal ($\sim 6 - 7$ V), adjust the vertical deflection to ~ -3 V, horizontal deflection ~ 0 V.

5. In the "Other" panel, set "microscope mode" to "contact". In the "Scan" panel, set the "scan angle" to 90°,

6. In the "Scan" panel, set "scan size" to 30 μm, "samples/line" to 256 or 512, "lines" to the same value, "aspect ratio" to 1.00, "slow-scan axis" to "enabled", "deflection setpoint" to $0.5 - 1$ V higher than the vertical baseline, and engage the system to obtain height/lateral force images. In addition, set "integral gain" and "proportional gain" to ~ 0.3,

7. In the "Channel" panels, set the three imaging channels to be height, friction (trace) and friction (retrace), respectively. Importantly, make sure the option "offline planefit" is set to "none".

8. Find a position with a full hexagon in the middle of the scanning region, and capture the images.

9. Readjust the vertical deflection to ~ -3 V and horizontal deflection to ~ 0 V in case of significant drift of these signals, set "samples/line" to 256, "lines" to 8,

and aspect ratio to 32.0, and "deflection setpoint" to be ~ 0.3 V less than the vertical deflection (there is a ~ 0.5 V difference between the actual and preset deflection setpoint). Record the exact value of vertical deflection and engage the system.

10. Adjust the setpoint value so the probe tip just barely engaged with the substrate, and increase the gains to allow more precise measurement of the height profile. Capture the image.

11. Increase the setpoint values at a constant increment (e.g., 0.5 V), decrease the gains as increasing the setpoint, capture the images at each of the setpoint values.

12. Stop imaging upon full compression/interpenetration of the aggrecan layer (height ~ 0) for the nanosized probe tip, or at $\sim 7-8$ V of the setpoint values for the colloidal probe tip, record the exact value of the vertical baseline values immediately after disengaging the system.

13. Switch to "PicoForce" Mode for the force versus separation distance measurement.

14. In the "Force" panel, set the "ramp size" to 2 μm, "trigger threshold" to ~ 400 nm, "trigger mode" to "relative" and "scan rate" to the frequency corresponding to 1 μm/s tip velocity (0.25 Hz for 2 μm ramp), "surface delay" to 0 sec, and "number of samples" to 512. The three channels are set to Z sensor versus Time, Deflection versus Time and Deflection versus Z. Click "single" to proceed a single indentation, capture the force versus distance curve.

15. Set the "scan rate" to other values (e.g., 2.5 Hz for 10 μm/s, 0.025 Hz for 100 nm/s) to capture the curves at different displacement rates.

16. To measure the self-adhesion, set "surface delay" to $1-30$ sec, and capture the force versus distance curves.

17. Repeat the experiment at more then 3 different positions.

18. Thoroughly rinse the substrate and tip holder with the new solution to switch solution, and repeat the procedure.

19. Calibrate the deflection sensitivity by probing the tip on a hard surface, and calculating the slope in the constant compliance region. Then determine the normal spring constant by switching to "Thermal Tune" mode and using the thermal vibration method available for Nanoscope IV MultiMode AFM or Molecular Force Probe (MFP).

20. Normal force versus height, lateral force signal versus height curves can be extracted from the series of captured height/lateral signal images via MatLab.

H.4 Measurement of Aggrecan Packing Density

1. Boil the aggrecan-functionalized substrate in 2 mL DI water for $\sim$ 20 minutes, until there is $\sim$ 200 μL of solution left.

2. Freeze the residual solution in $-80°$C freezer and then lyophilize it.

3. Resuspend the residues after lyophilization with $\sim$ 50 μL DI water, and then use dimethylmethylene blue (DMMB) dye assay to measure the amount of GAG (hence aggrecan).

H.5 Lateral Force Calibration

1. Load the calibration sample and AFM tip into the system, adjust the laser position on the cantilever to reach the maximum sum ($\sim 6 - 7$ V), and zero both vertical and horizontal deflections.

2. Wait for the system to equilibrate, usually $5 - 10$ min in air and $15 - 20$ min in fluid.

3. In the "Other" panel, set "microscope mode" to "contact". In the "Scan" panel, set the "scan angle" to 90°,

4. In the "Scan" panel, set "scan size" to 30 μm, "samples/line" to 256 or 512, "lines" to the same value, "aspect ratio" to 1.00, "slow-scan axis" to "enabled", "deflection setpoint" to $0.5 - 1$ V higher than the vertical baseline, and engage the system to obtain height/lateral force images. In addition, set "integral gain" and "proportional gain" to ~ 0.3,

5. Engage the tip and switch to force mode to do a normal force curve measurement. Determine the deflection sensitivity from the constant compliance slope and determine the normal spring constant by Thermal Tune (Nanoscope IV and MFP, you cannot determine the normal spring constant on Nanoscope IIIA).

6. Back to the image mode, and set the image offset to the edge of the flat region and sloped region. Change number of lines to 8 or 16.

7. Disengage and re-zero deflection signals, engage again and slowly decrease the setpoint to disengage, slowly increase setpoint to engage again, the normal setpoint is the point of $\sim$ zero normal force, or initial baseline. Capture the image.

8. Increase the setpoint by a given amount (0.5 V or 1 V) and capture one image each time.

9. After capture 10 images, disengage and record the vertical deflection baseline signal as the final baseline.

10. Repeat the procedure for 2 or 3 times at different locations.

11. For the colloidal probe tip, first let the probe tip scan on a flat mica sample at a series of normal force, and then switch to a tilted mica sample ($\alpha \sim 20°$), and scan at the top of the tilted region (to avoid the contact of the base of the cantilever to the mica during scanning) at the same normal forces, record the lateral signals in both cases.

12. Calculate the lateral deflection sensitivity a flowing the mathematical procedure, as described in Appendix B.

H.6 Cartilage Proteoglycan Digestion

1. Incubate the Cartilage disk (0.9 mm in diameter, $\sim$ 0.5 mm thick) cartilage disk incubated in trypsin (1 mg/mL) in 0.15 M NaCl, 0.05 M Na phosphate (sterile), pH = 7.2 for 24 hrs.

2. Thoroughly rinse the sample with 0.15 M NaCl and 0.05 M Tris-HCl solution, pH = 8.0 (sterile), and incubate in 0.1 U/mL chondroitinase-ABC in 0.15 M NaCl, 0.05 M Tris-HCl, pH = 8.0 for 24 hours.

3. More than 95% of proteoglycan should be digested via these two enzymes, as confirmed by dimethylmethylene blue dye assay.

H.7 Aggrecan Nanomechanics upon Enzymatic Digestion (m-Calpain)

1. Setup the Nanoscope IV AFM with the PicoForce piezo using a nanosized pyramidal tip, mount the probe tip on the glass fluid tip holder, drop $\sim$ 30 μL 0.001 M NaCl solution on island mounted with the tip.

2. Add $\sim$ 100 μL solution on the aggrecan substrate, bring the probe tip close to the substrate.

3. Wait for the system to equilibrate, usually $5 - 10$ min in air and $15 - 20$ min in fluid.

4. Maximize the sum signal ($\sim 6 - 7$ V), adjust the vertical deflection to ~ -3 V, horizontal deflection ~ 0 V.

5. In the "Other" panel, set "microscope mode" to "contact".

6. In the "Scan" panel, set "scan size" to 30 μm, "samples/line" to 256 or 512, "lines" to the same value, "aspect ratio" to 1.00, "slow-scan axis" to "enabled", "deflection setpoint" to $0.5 - 1$ V higher than the vertical baseline, and engage

the system to obtain height/lateral force images. In addition, set "integral gain" and "proportional gain" to ~ 0.3,

7. In the "Channel" panels, set at least one image channel to "height".

8. Find a position with a full hexagon in the middle of the scanning region, and capture the images.

9. Readjust the vertical deflection to ~ -3 V and horizontal deflection to ~ 0 V in case of significant drift of these signals, set "samples/line" to 256, "lines" to 8, and aspect ratio to 32.0, and "deflection setpoint" to be ~ 0.3 V less than the vertical deflection (there is a ~ 0.5 V difference between the actual and preset deflection setpoint). Record the exact value of vertical deflection and engage the system.

10. Adjust the setpoint value so the probe tip just barely engaged with the substrate, and increase the gains to allow more precise measurement of the height profile. Capture the image.

11. Increase the setpoint values at a constant increment (e.g., 0.5 V), decrease the gains as increasing the setpoint, capture the images at each of the setpoint values.

12. Stop imaging upon full compression/interpenetration of the aggrecan layer (height ~ 0), record the exact value of the vertical baseline values.

13. Switch to PicoForce Mode for the force versus separation distance measurement.

14. In the "Force" panel, set the "ramp size" to 2 μm, "trigger threshold" to ~ 400 nm, "trigger mode" to "relative" and "scan rate" to the frequency corresponding to 1 μm/s tip velocity (0.25 Hz for 2 μm ramp), "surface delay" to 0 sec, and "number of samples" to 512. The three channels are set to Z sensor versus Time, Deflection versus Time and Deflection versus Z. Click "single" to proceed a single indentation, capture the force versus distance curve.

15. Switch the solution to the mixed buffer solution without m-calpain without moving the substrate by using filtering paper to absorb the old solution, and fill with the new solution for 3 times. Repeat the experiments for height versus normal force and force verus separation distance measurements. Leave the system in the force mode without disengaging the system.

16. Switch to the mixed buffer solution with 0.4 nM m-calpain, and record the change of force versus separation distance profile from $1 - 60$ minutes after the addition of m-calpain.

17. After 60 minutes of digestion by m-calpain, repeat the height versus applied normal force measurements.

18. Switch back to 0.001 M NaCl solution, repeat the height versus normal force and force versus separation distance measurements.

19. The deflection sensitivity was calibrated by probing the tip on a hard surface, and calculating the slope in the constant compliance region. The spring constant was then calibrated using the thermal vibration method, known the deflection sensitivity.

20. Height versus normal force and force versus separation distance data can be extracted and analyzed via MatLab.

H.8 Cartilage Time-Dependent Nanomechanics

1. Mount the cartilage disk on the magnetic sample holder using crazy glue, drop ~ 100 μL solution (for example, PBS) on the sample.

2. Setup the Nanoscope IV AFM with the PicoForce piezo, mount the probe tip on the glass fluid tip holder, drop ~ 30 μL PBS on the island mounted with the tip.

3. Wait $15 - 20$ min for the system to equilibrate.

4. In the "Other" panel, set "microscope mode" to "contact".

5. In the "Scan" panel, set "scan size" to 5 μm, "samples/line" to 256 or 512, "lines" to the same value, "aspect ratio" to 1.00, "slow-scan axis" to "enabled", "deflection setpoint" to $0.5 - 1$ V higher than the vertical baseline, and engage the system to obtain height/lateral force images. In addition, set "integral gain" and "proportional gain" to ~ 0.3,

6. Find a relative flat position, where the height variation is less than 1 μm over the 5 μm scan, and switch to "PicoForce" Mode.

7. In the "Force" panel, set the "ramp size" to 2 μm (2.5 μm for the PG-depleted cartilage using a microsized probe tip), "trigger threshold" to 150 nm, "trigger mode" to "relative" and "scan rate" to the frequency corresponding to 1 μm/s tip velocity (0.25 Hz for 2 μm ramp), "surface delay" to 0 sec, and "number of samples" to 512. The three channels are set to Z sensor versus Time, Deflection versus Time and Deflection versus Z. Click "single" to proceed a single indentation, capture the indentation curve.

8. Repeat the procedure for 10 times at the same indentation location, and change the "scan rate" to perform the indentation at 10 μm/s and 100 nm/s.

9. Switch to "Script" panel, set two consecutive ramp segments, 1. delta = 0, delay = 3 sec; 2. delta = 2 μm, delay = 60 sec, ramp velocity = 1 μm/s. In the "Mode" list under "Force Mode" panel, set "strip chart rate" to 1,000 Hz and "strip chart size" to 100 s.

10. For ramp-and-hold stress relaxation experiment, perform one indentation (without capture) at 2 μm ramp size and immediately click "run" in the script mode after the indentation, capture the curve after the 60 seconds ramp delay.

11. For the dynamic loading, connect the external sinusoidal electronic wave generator to the "user input/output" plug-in on the PicoForce controller, and switch to user input.

12. To obtain the data at a given frequency and amplitude (for example, 1 Hz and $\sim$ 4 nm z-piezo displacement amplitude), set the attenuation to $40-20-10$ and frequency to 1Hz, and turn on the wave generator after $10-15$ seconds upon loading of the probe tip on the substrate. The data $30-35$ seconds after loading ($\sim$ 20 seconds after the turn-on of dynamic deformation) could be analyzed as the steady-state deformation.

13. Repeat the procedure for different frequency and amplitudes, the attenuation is set to (1) 4 nm displacement amplitude: $40-20-10$ for $1-100$ Hz, $40-10-8$ for 316 Hz, 40 for 1,000 Hz; (2) 20 nm amplitude: $40-10-4-1$ for $1-100$ Hz, $20-8$ for 1000 Hz; (3) 40 for $1-100$ Hz. The "strip chart rate" is set to 10,000 Hz for the dynamic deformation frequency $>$ 100 Hz.

14. The captured data was analyzed in MatLab, make sure to multiply 8 for the exported cantilever deformation data and 2 for the z-piezo displacement data if using the Nanoscope software version 6.13 or older.

15. The control experiment can be performed on mica sample following the same procedure, except that the ramp size is set to 1 μm. Then follow the procedure described in Appendix F to complete the calibration.

H.9 Nanoindentation on Mouse Cartilage

1. Dissect the mouse knee joint in the presence of protease inhibitors.

2. Mount the mouse knee joint on the magnetic disc using crazy glue, with the lateral and medial condyles facing up, and medial condyle closer to the person who is operating the system. Drop $\sim$ 100 μL of the PBS in the presence of protease inhibitors.

3. Setup the Nanoscope IV AFM with the PicoForce piezo, mount the probe tip on the glass fluid tip holder, drop $\sim$ 30 μL PBS on the island mounted with the tip.

4. Wait $15 - 20$ min for the system to equilibrate.

5. Maximize the sum signal ($\sim 6 - 7$ V), adjust the vertical deflection to ~ -3 V, horizontal deflection ~ 0 V.

6. In the "Other" panel, set "microscope mode" to "contact".

7. In the "Scan" panel, set "scan size" to 5 μm, "samples/line" to 256 or 512, "lines" to the same value, "aspect ratio" to 1.00, "slow-scan axis" to "enabled", "deflection setpoint" to $0.5 - 1$ V higher than the vertical baseline, and engage the system to obtain height/lateral force images. In addition, set "integral gain" and "proportional gain" to ~ 0.3,

8. Find the top of the lateral condyle, where the geometry is relatively flat, and switch to "PicoForce" mode.

9. In the "Force" panel, set the "ramp size" to 2 μm (2.5 μm for the PG-depleted cartilage using a microsized probe tip), "trigger threshold" to 150 nm, "trigger mode" to "relative" and "scan rate" to the frequency corresponding to 1 μm/s tip velocity (0.25 Hz for 2 μm ramp), "surface delay" to 0 sec, and "number of samples" to 512. The three channels are set to Z sensor versus Time, Deflection versus Time and Deflection versus Z. Click "single" to proceed a single indentation, capture the indentation curve.

10. Repeat the procedure for 10 times at the same indentation location, and change the "scan rate" to perform the indentation at 10 μm/s and 100 nm/s.

11. Repeat the measurement for at least 10 different indentation locations on the mouse knee lateral condyle.

Bibliography

[1] R. M. Aspden, T. Larsson, R. Svensson, and D. K. Heinegard. Computer-controlled mechanical testing machine for small samples of biological viscoelastic materials. *Journal of Biomedical Engineering-Transactions of the ASME*, 13:521–525, 1991.

[2] G. A. Ateshian and V. C. Mow. Friction, lubrication, and wear of articular cartilage and diathrodial joints. In V. C. Mow and R. Huskes, editors, *Basic Orthopaedic Biomechanics and Mechanobiology*, pages 447–494. Lippincott, Williams & Wilkins, Philadephia, 2005.

[3] T. Auletta, M. R. de Jong, A. Mulder, F. van Veggel, J. Huskens, D. N. Reinhoudt, S. Zou, S. Zapotoczny, H. Schonherr, G. J. Vancso, and L. Kuipers. Beta-cyclodextrin host-guest complexes probed under thermodynamic equilibrium: thermodynamics and AFM force spectroscopy. *Journal of the American Chemical Society*, 126(5):1577–1584, 2004.

[4] M. Bathe, G. C. Rutledge, A. Grodzinsky, and B. Tidor. Osmotic pressure of aqueous chondroitin sulfate solution: a molecular modeling investigation. *Biophysical Journal*, 89:2357–2371, 2005.

[5] E. Beniash, W. Traub, A. Veis, and S. Weiner. A transmission electron microscopy study using vitrified ice sections of predentin: structural changes in the dentin collagenous matrix prior to mineralization. *Journal of Structural Biology*, 132:212–225, 2000.

[6] M. Benz, N. H. Chen, and J. Israelachvili. Lubrication and wear properties of grafted polyelectrolytes, hyaluronan and hylan, measured in the surface forces apparatus. *Journal of Biomedical Materials Research Part A*, 71A(1):6–15, 2004.

[7] C. Berthet-Colominas, A. Miller, D. Herbage, M.-C. Ronziere, and D. Tocchetti. Structural studies of collagen fibres from intervertebral disc. *Biochimica et Biophysica Acta*, 706:50–64, 1982.

[8] S. Bhattacharjee and M. Elimelech. Surface element integration: a novel technique for evaluation of DLVO interaction between a particle and a flat plate. *Journal of Colloid and Interface Science*, 193:273–285, 1997.

[9] G. Bogdanovic, A. Meurk, and M. W. Rutland. Tip friction - torsional spring constant determination. *Colloids and Surfaces B-Biointerfaces*, 19(4):397–405, 2000.

[10] J. Bordas, J. Woodhead-Galloway, and D. W. L. Hukins. Energy dispersive X-ray diffraction by collagen fibrils in costal cartilage using synchrotron radiation. *Biochemical and Biophysical Research Communications*, 84(3):627–630, 1978.

[11] J. Buckwalter and L. Rosenberg. Electron microscopic studies of cartilage proteoglycans. *Electron Microscopy Review*, 1:87–112, 1988.

[12] J. A. Buckwalter, H. J. Mankin, and A. J. Grodzinsky. Articular cartilage and osteoarthritis. *Instructional Course Lectures*, 54:465–480, 2005.

[13] P. Bursac, C. V. McGrath, S. R. Eisenberg, and D. Stamenovic. A microstructural model of elastostatic properties of articular cartilage in confined compression. *Journal of Biomechanical Engineering-Transactions of the ASME*, 122(4):347–353, 2000.

[14] M. D. Buschmann and A. J. Grodzinsky. A molecular-model of proteoglycan-associated electrostatic forces in cartilage mechanics. *Journal of Biomechanical Engineering-Transactions of the ASME*, 117(2):179–192, 1995.

[15] R. G. Cain, S. Biggs, and N. W. Page. Force calibration in lateral force microscopy. *Journal of Colloid and Interface Science*, 227(1):55–65, 2000.

[16] R. G. Cain, M. G. Reitsma, S. Biggs, and N. W. Page. Quantitative comparison of three calibration techniques for the lateral force microscope. *Review of Scientific Instruments*, 72(8):3304–3312, 2001.

[17] R. W. Carpick and M. Salmeron. Scratching the surface: fundamental investigations of tribology with atomic force microscopy. *Chemical Reviews*, 97(4):1163–1194, 1997.

[18] G. T. Charras, J. C. Yarrow, M. A. Horton, L. Mahadevan, and T. J. Mitchison. Non-equilibration of hydrostatic pressure in blebbing cells. *Nature*, 435(7040):365–369, 2005.

[19] C.-H. Chen, M.-L. Yeh, M. Geyer, G.-J. Wang, M.-H. Huang, M. H. Heggeness, M. Hook, and Z.-P. Luo. Interactions between collagen IX and biglycan measured by atomic force microscopy. *Biochemical and Biophysical Research Communications*, 339:204–208, 2006.

[20] L. E. Chun, T. J. Koob, and D. R. Eyre. Sequentical enzymatic dissection of the proteoglycan complex from articular cartilage. In *32nd Annual Meeting of Orthopaedic Research Society*, New Orleans, Louisiana, 1986.

[21] R. L. Cleland, J. L. Wang, and D. M. Detweiler. Polyelectrolyte properties of sodium hyaluronate. II. Potentiometric titration of hyaluronic acid. *Macromolecules*, 15:386–395, 1982.

[22] E. M. Darling, S. Zauscher, and F. Guilak. Viscoelastic properties of zonal articular chondrocytes measured by atomic force microscopy. *Osteoarthritis and Cartilage*, 14:571–579, 2006.

[23] M. O. de la Cruz, L. Belloni, M. Delsanti, J. P. Dalbiez, O. Spalla, and M. Drifford. Precipitation of highly-charged polyelectrolyte solutions in the presence of multivalent salts. *Journal of Chemical Physics*, 103(13):5781–5791, 1995.

[24] J. M. de la Fuente, P. Eaton, A. G. Barrientos, M. Menendez, and S. Penades. Thermodynamic evidence for Ca^{2+}-mediated self-aggregation of Lewis X gold glyconanoparticles. a model for cell adhesion via carbohydrate-carbohydrate interaction. *Journal of the American Chemical Society*, 127(17):6192–6197, 2005.

[25] J. M. de la Fuente and S. Penades. Glyconanoparticles: types, synthesis and applications in glycoscience, biomedicine and material science. *Biochimica et Biophysica Acta*, 1760:636–651, 2006.

[26] D. Dean, J. Seog, C. Ortiz, and A. J. Grodzinsky. Molecular-level theoretical model for electrostatic interactions within polyelectrolyte brushes: applications to charged glycosaminoglycans. *Langmuir*, 19(13):5526–5539, 2003.

[27] D. Dean, L. Han, C. Ortiz, and A. J. Grodzinsky. Nanoscale conformation and compressibility of cartilage aggrecan using microcontact printing and atomic force microscopy. *Macromolecules*, 38(10):4047–4049, 2005.

[28] D. Dean, L. Han, A. J. Grodzinsky, and C. Ortiz. Compressive nanomechanics of opposing aggrecan macromolecules. *Journal of Biomechanics*, 39(14):2555–2565, 2006.

[29] R. D. Domike, C. Ortiz, and C. L. Cooney. Direct measurement of nanoscale interactions between pharmaceutical particles via high-resolution force spectroscopy. In *Abstracts of Papers of the Amercan Chemical Society*, volume 224, pages U416–U417, 2002.

[30] J. Dudhia. Aggrecan, aging and assembly in articular cartilage. *Cellular and Molecular Life Sciences*, 62:2241–2256, 2005.

[31] W. L. Dunbar, K. Un, P. S. Donzelli, and R. L. Spilker. An evaluation of three-dimensional diarthrodial joint contact using penetration data and the finite element method. *Journal of Biomechanical Engineering-Transactions of the ASME*, 123(4):333–340, 2001.

[32] D. M. Ebenstein, A. Kuo, J. J. Rodrigo, A. H. Reddi, M. Ries, and L. Pruitt. A nanoindentation technique for functional evaluation of cartilage repair tissue. *Journal of Materials Research*, 19(1):273–281, 2004.

[33] A. W. Eberhardt, L. M. Keer, J. L. Lewis, and V. Vithoontien. An analytical model of joint contact. *Journal of Biomechanical Engineering-Transactions of the ASME*, 112(4):407–413, 1990.

[34] S. Ecke, R. Raiteri, E. Bonaccurso, C. Reiner, H. J. Deiseroth, and H. J. Butt. Measuring normal and friction forces acting on individual fine particles. *Review of Scientific Instruments*, 72(11):4164–4170, 2001.

[35] S. Ehrlich, N. Wolff, R. Schneiderman, A. Maroudas, K. H. Parker, and C. P. Winlove. The osmotic pressure of chondroitin sulphate solutions: experimental measurements and theoretical analysis. *Biorheology*, 35(6):383–97., 1998.

[36] E. F. Eikenberry, B. Childs, S. B. Sheren, D. A. D. Parry, A. S. Craig, and B. Brodsky. Crystalline fibril structure of type-II collagen in lamprey notochord sheath. *Journal of Molecular Biology*, 176(2):261–277, 1984.

[37] S. R. Eisenberg and A. J. Grodzinsky. Swelling of articular cartilage and other connective tissues: electromechanochemical forces. *Journal of Orthopaedic Research*, 3(2):148–59, 1985.

[38] S. R. Eisenberg and A. J. Grodzinsky. Electrokinetic micromodel of extracellular matrix and other polyelectrolytes networks. *PhysicoChemical Hydrodynamics*, 10(4):517–539, 1988.

[39] C. Esquenet and E. Buhler. Aggregation behavior in semidilute rigid and semirigid polysaccharide solutions. *Macromolecules*, 35:3708–3716, 2002.

[40] E. Evans. Probing the relation between force - lifetime - and chemistry in single molecular bonds. *Annual Review of Biophysics and Biomolecular Structure*, 30:105–128, 2001.

[41] D. Eyre. Collagen of articular cartilage. *Arthritis Research*, 4(1):30–35, 2002.

[42] D. R. Eyre, M. A. Weis, and J.-J. Wu. Articular cartilage collagen: an irreplaceable framework? *European Cells and Materials*, 12:57–63, 2006.

[43] G. E. Fantner, J. Adams, P. Turner, P. J. Thurner, L. W. Fisher, and P. K. Hansma. Nanoscale ion mediated networks in bone: osteopontin can repeatedly dissipate large amounts of energy. *Nano Letters*, 7(8):2491–2498, 2007.

[44] G. E. Fantner, T. Hassenkam, J. H. Kindt, J. C. Weaver, H. Birkedal, L. Pechenik, J. A. Cutroni, G. A. G. Cidade, G. D. Stucky, D. E. Morse, and P. K. Hansma. Sacrificial bonds and hidden length dissipate energy as mineralized fibrils separate during bone fracture. *Nature Materials*, 4(8):612–616, 2005.

[45] R. W. Farndale, D. J. Buttle, and A. J. Barrett. Improved quantitation and discrimination of sulphated glycosaminoglycans by use of dimethylmethylene blue. *Biochimica et Biophysica Acta*, 883(2):173–177, 1986.

[46] A. Feiler, P. Attard, and I. Larson. Calibration of the torsional spring constant and the lateral photodiode response of frictional force microscopes. *Review of Scientific Instruments*, 71(7):2746–2750, 2000.

[47] A. Feiler, M. A. Plunkett, and M. W. Rutland. Atomic force microscopy measurements of adsorbed polyelectrolyte layers. 1. Dynamics of forces and friction. *Langmuir*, 19(10):4173–4179, 2003.

[48] C. Flannery. Personal communication, 2006.

[49] E. Fouissac, M. Milas, M. Rinaudo, and R. Borsali. Influence of the ionic strength on the dimensions of sodium hyaluronate. *Macromolecules*, 25:5613–5617, 1992.

[50] E. H. Frank and A. J. Grodzinsky. Cartilage electromechanics. II. A continuum model of cartilage electrokinetics and correlation with experiments. *Journal of Biomechanics*, 20(6):629–639, 1987.

[51] T. Fujii, Y. L. Sun, K. N. An, and Z. P. Luo. Mechanical properties of single hyaluronan molecules. *Journal of Biomechanics*, 35(4):527–531, 2002.

[52] T. Fujimoto, H. Kawashima, T. Tanaka, M. Hirose, N. Toyama-Sorimachi, Y. Matsuzawa, and M. Miyasaka. CD44 binds a chondroitin sulfate proteoglycan, aggrecan. *International Immunology*, 13(3):359–366, 2001.

[53] J. P. Gao, W. D. Luedtke, and U. Landman. Friction control in thin-film lubrication. *Journal of Physical Chemistry B*, 102:5033–5037, 1998.

[54] C. P. Green, H. Lioe, J. P. Cleveland, R. Proksch, P. Mulvaney, and J. E. Sader. Normal and torsional spring constants of atomic force microscope cantilevers. *Review of Scientific Instruments*, 75(6):1988–1996, 2004.

[55] A. J. Grodzinsky, M. E. Levenston, M. Jin, and E. H. Frank. Cartilage tissue remodeling in response to mechanical forces. *Annual Review of Biomedical Engineering*, 2:691–713, 2000.

[56] A. J. Grodzinsky and J. R. Melcher. Electromechanical transduction with charged polyelectrolyte membranes. *IEEE Transactions on Biomedical Engineering*, 23(6):421–433, 1976.

[57] A. J. Grodzinsky, V. Roth, E. Myers, W. D. Grossman, and V. C. Mow. The significance of electromechanical and osmotic forces in the nonequilibrium swelling behavior of articular cartilage in tension. *Journal of Biomechanical Engineering-Transactions of the ASME*, 103(4):221–231, 1981.

[58] M. D. Grynpas, D. R. Eyre, and D. A. Kirschner. Collagen type-II differs from type-I in native molecular packing. *Biochimica et Biophysica Acta*, 626(2):346–355, 1980.

[59] B. M. Gumbiner. Cell adhesion: the molecular basis of tissue architecture and morphogenesis. *Cell*, 84:345–357, 1996.

[60] S.-i. Hakomori. Carbohydrate-carbohydrate interaction as an initial step of cell recognition. *Pure and Applied Chemistry*, 63(4):473–482, 1991.

[61] L. Han, D. Dean, L. A. Daher, A. J. Grodzinsky, and C. Ortiz. Biomolecular adhesion between opposing cartilage aggrecan macromolecules. In *52nd Annual Meeting of the Orthopaedic Research Society*, page 361, Chicago, IL, 2006.

[62] L. Han, D. Dean, C. Ortiz, and A. J. Grodzinsky. Lateral nanomechanics of cartilage aggrecan macromolecules. *Biophysical Journal*, 92(4):1384–1398, 2007.

[63] L. Han, D. Dean, P. Mao, C. Ortiz, and A. J. Grodzinsky. Nanoscale shear deformation mechanisms of opposing cartilage aggrecan macromolecules. *Biophysical Journal*, 93(5):L23–L25, 2007.

[64] J. Happel. Viscous flow relative to arrays of cylinders. *AIChE Journal*, 5(2):174–177, 1959.

[65] T. E. Hardingham and A. J. Fosang. Proteoglycans: many forms and many functions. *FASEB Journal*, 6:861–870, 1992.

[66] T. E. Hardingham and H. Muir. The specific interaction of hyaluronic acid with cartilage proteoglycans. *Biochimica et Biophysica Acta*, 279:401–405, 1972.

[67] T. E. Hardingham, H. Muir, M. K. Kwan, W. M. Lai, and V. C. Mow. Viscoelastic properties of proteoglycan solutions with varying proportions present as aggregates. *Journal of Orthopaedic Research*, 5(1):36–46, 1987.

[68] V. C. Hascall, D. K. Heinegard, and T. N. Wight. Proteoglycans metabolism and pathology. In E. D. Hay, editor, *Cell Biology of Extracellular Matrix*, pages 149–176. Plenum Press, New York, 1991.

[69] S. R. Haseley, H. J. Vermeer, J. P. Kamerling, and J. F. G. Vliegenthart. Carbohydrate self-recognition mediates marine sponge cellular adhesion. *Proceedings of the National Academy of Sciences of the United States of America*, 98(16):9419–9424, 2001.

[70] R. G. Haverkamp, M. A. Williams, and J. E. Scott. Stretching single molecules of connective tissue glycans to characterize their shape-maintaining elasticity. *Biomacromolecules*, 6:1816–1818, 2005.

[71] K. Hayashi, K. Tsutsumi, F. Nakajima, T. Norisuye, and A. Teramoto. Chain stiffness and excluded volume effects in solutions of sodium hyaluronate at high ionic strength. *Macromolecules*, 28:3824–3830, 1995.

[72] L. G. Hector and S. R. Schmid. Simulation of asperity plowing in an atomic force microscope part I: experimental and theoretical methods. *Wear*, 215(1-2):247–256, 1998.

[73] H. Hedlund, E. Hedbom, D. Heinegard, S. Mengarelli-Widholm, F. P. Reinholt, and O. Svensson. Association of the aggrecan keratan sulfate-rich region with collagen in bovine articular cartilage. *Journal of Biological Chemistry*, 274(9):5777–5781, 1999.

[74] D. Heinegard and V. C. Hascall. Aggregation of cartilage proteoglycans. 3. Characteristics of proteins isolated from trypsin digests of aggregates. *Journal of Biological Chemistry*, 249(13):4250–4256, 1974.

[75] D. Heinegard and A. Oldberg. Structure and biology of cartilage and bone matrix noncollagenous macromolecules. *FASEB Journal*, 3:2042–2051, 1989.

[76] D. K. Heinegard and Y. Sommarin. Proteoglycans: an overview. *Methods in Enzymology*, 144:305–319, 1987.

[77] H. J. Helminen, A.-M. Saamanen, H. Salminen, and M. M. Hyttinen. Transgenic mouse models for studying the role of cartilage macromolecules in osteoarthritis. *Rheumatology*, 41:848–856, 2002.

[78] G. K. Hunter, K. S. Wong, and J. J. Kim. Binding of calcium to glycosaminoglycans: an equilibrium dialysis study. *Archives of Biochemistry and Biophysics*, 260(1):161–167, 1988.

[79] J. L. Hutter and J. Bechhoefer. Calibration of atomic-force microscope tips. *Review of Scientific Instruments*, 64(7):1868–1873, 1993.

[80] J. Hyttinen, M. M. T., T. Lapvetelainen, J. Lindblom, D. J. Prockop, S.-W. Li, M. Arita, J. S. Jurvelin, and H. J. Helminen. Inactivation of one allele of the type II collagen gene alters the collagen network in murine articular cartilage and makes cartilage softer. *Annals of the Rhematic Diseases*, 60:262–268, 2001.

[81] J. N. Israelachvili. *Intermolecular and Surface Forces.* Academic Press, London, 1992.

[82] K. Iwabuchi, S. Yamamura, A. Prinetti, K. Handa, and S.-i. Hakomori. GM3-enriched microdomain involved in cell adhesion and signal transduction through carbohydrate-carbohydrate interaction in mouse melanoma B16 cells. *Journal of Biological Chemistry*, 273(15):9130–9138, 1998.

[83] M. S. Jin and A. J. Grodzinsky. Effect of electrostatic interactions between glycosaminoglycans on the shear stiffness of cartilage: a molecular model and experiments. *Macromolecules*, 34(23):8330–8339, 2001.

[84] K. L. Johnson and J. A. Greenwood. An adhesion map for the contact of elastic spheres. *Journal of Colloid and Interface Science*, 192(2):326–333, 1997.

[85] M. Kapple and H.-J. Butt. The colloidal probe technique and its application to adhesion force measurements. *Particle & Particle System Characterization*, 19:129–143, 2002.

[86] R. Kilger, R. Gottardi, L. Aeschimann, V. Cardinali, R. Imer, U. Konig, R. Raiteri, U. Staufer, M. Stolz, U. Aebi, and N. Friederich. Towards early detection of osteoarthritis: assessing human articular cartilage by scanning force microscopy. In *52nd Annual Meeting of the Orthopaedic Research Society*, page 1507, Chicago, IL, 2006.

[87] A. J. Kinloch. The science of adhesion: I. Surface and interfacial aspects. *Journal of Materials Science*, 15(99):2141–2166, 1980.

[88] M. M. Kohonen, M. E. Karaman, and R. M. Pashley. Debye length in multivalent electrolyte solutions. *Langmuir*, 16:5749–5753, 2000.

[89] R. Krishnan, M. Caligaris, R. L. Mauck, C. T. Hung, K. D. Costa, and G. A. Ateshian. Removal of the superficial zone of bovine articular cartilage does not increase its friction coefficient. *Osteoarthritis and Cartilage*, 12:947–955, 2004.

[90] G. J. Leggett. Friction force microscopy of self-assembled monolayers: probing molecular organisation at the nanometre scale. *Analytica Chimica Acta*, 479(1):17–38, 2003.

[91] C. M. Lieber. Functional-group imaging by chemical force microscopy. In *Abstracts of Papers of the American Chemical Society*, volume 209, pages 359–PHYS, 1995.

[92] U. Lindahl and M. Hook. Glycosaminoglycans and their binding to biological macromolecules. *Annual Review of Biochemistry*, 47:385–417, 1978.

[93] E. Liu, B. Blanpain, and J. P. Celis. Calibration procedures for frictional measurements with a lateral force microscope. *Wear*, 192(1-2):141–150, 1996.

[94] X. Liu, J. Q. Sun, M. H. Heggeness, M.-L. Yeh, and Z.-P. Luo. Direct quantification of the rupture force of single hyaluronan/hyaluronan binding protein bonds. *FEBS Letters*, 563:23–27, 2004.

[95] E. A. MacGregor and J. M. Bowness. Interaction of proteoglycans and chondroitin sulfates with calcium or phosphate ions. *Canadian Journal of Biochemistry*, 49:417–425, 1971.

[96] R. E. Mahaffy, S. Park, E. Gerde, J. Kas, and C. K. Shih. Quantitative analysis of the viscoelastic properties of thin regions of fibroblasts using atomic force microscopy. *Biophysical Journal*, 86:1777–1793, 2004.

[97] A. F. Mak. The apparent viscoelastic behavior of articular-cartilage - the contributions from the intrinsic matrix viscoelasticity and interstitial fluid-flows. *Journal of Biomechanical Engineering-Transactions of the ASME*, 108(2):123–130, 1986.

[98] A. Maroudas. Balance between swelling pressure and collagen tension in normal and degenerate cartilage. *Nature*, 260:808–809, 1976.

[99] A. Maroudas. Physicochemical properties of articular cartilage. In M. A. R. Freeman, editor, *Adult Articular Cartilage*, pages 215–290. Pitman, England, 1979.

[100] A. Maroudas. Physical chemistry of articular cartilage and the intervertebral disk in joints and synovial fluid. In *The Joints and Synovial Fluid.*, volume II, pages 239–291. Academic Press, London, 1980.

[101] J. I. Martin and Z. G. Wang. Polymer brushes - scaling, compression forces, interbrush penetration, and solvent size effects. *Journal of Physical Chemistry*, 99(9):2833–2844, 1995.

[102] R. Merkel, P. Nassoy, A. Leung, K. Ritchie, and E. Evans. Energy landscapes of receptor-ligand bonds explored with dynamic force spectroscopy. *Nature*, 397:50–53, 1999.

[103] E. Meyer, R. M. Overney, K. Dransfeld, and T. Gyalog. *Nanoscience: Friction and Rheology on the Nanometer Scale.* World Scientific, River Edge, NJ, 1999.

[104] A. Miller. Molecular packing in collagen fibrils. In G. N. Ramachandran and A. H. Reddi, editors, *Biochemistry of Collagen*, pages 85–136. Plenum Press, New York and London, 1976.

[105] M. Morgelin, D. Heinegard, J. Engel, and M. Paulsson. The cartilage proteoglycan aggregate : assembly through combined protein-carbohydrate and protein-protein interactions. *Biophysical Chemistry*, 50:113–128, 1994.

[106] R. W. Moskowitz. Experimental models of osteoarthritis. In *Osteoarthritis: Diagnosis and Medical/Surgical Management.* 1992.

[107] V. C. Mow, W. Y. Gu, and F. H. Chen. Structure and function of articular cartilage and meniscus. In V. C. Mow and R. Huskes, editors, *Basic Orthopaedic Biomechanics and Mechanobiology*, pages 181–258. Lippincott, Williams & Wilkins, Philadephia, 2003.

[108] V. C. Mow, S. C. Kuei, W. M. Lai, and C. G. Armstrong. Biphasic creep and stress-relaxation of articular-cartilage in compression - theory and experiments. *Journal of Biomechanical Engineering-Transactions of the ASME*, 102(1):73–84, 1980.

[109] I. H. M. Muir. Biochemistry. In M. A. R. Freeman, editor, *Adult Articular Cartilage*, pages 145–214. Pitman Medical, Kent, 1979.

[110] L. Ng, A. J. Grodzinsky, P. Patwari, J. Sandy, A. Plaas, and C. Ortiz. Individual cartilage aggrecan macromolecules and their constituent glycosaminoglycans visualized via atomic force microscopy. *Journal of Structural Biology*, 143(3):242–257, 2003.

[111] L. Ng, H.-H. Hung, A. Sprunt, S. Chubinskaya, C. Ortiz, and A. J. Grodzinsky. Nanomechanical properties of individual chondrocytes and their developing growth factor-stimulated pericellular matrix. *Journal of Biomechanics*, 40(5):1011–1023, 2007.

[112] A. Noy, D. V. Vezenov, and C. M. Lieber. Chemical force microscopy. *Annual Review of Materials Science*, 27:381–421, 1997.

[113] D. F. Ogletree, R. W. Carpick, and M. Salmeron. Calibration of frictional forces in atomic force microscopy. *Review of Scientific Instruments*, 67(9):3298–3306, 1996.

[114] A. G. Ogston. *Chemistry and Molecular Biology of the Intercellular Matrix.* Academic, New York, 1970.

[115] A. I. Olin, M. Morgelin, T. Sasaki, R. Timpl, D. Heinegard, and A. Aspberg. The proteoglycans aggrecan and versican form networks with fibulin-2 through their lectin domain binding. *Journal of Biological Chemistry*, 276(2):1253–1261, 2001.

[116] W. C. Oliver and G. M. Pharr. An improved technique for determining hardness and elastic-modulus using load and displacement sensing indentation experiments. *Journal of Materials Research*, 7(6):1564–1583, 1992.

[117] S. T. Olson, H. R. Halvorson, and I. Bjork. Quantitative characterization of the thrombin-heparin interaction - discrimination between specific and nonspecific binding models. *Journal of Biological Chemistry*, 226(10):6342–6352, 1991.

[118] F. Ortolani, M. Giordano, and M. Marchini. A model for type II collagen fibrils: distinctive D-band patterns in native and reconstituted fibrils compared with sequence data for helix and telopeptide domains. *Biopolymers*, 54(6):448–463, 2000.

[119] H. Oshita, J. D. Sandy, K. Suzuki, A. Akaike, Y. Bai, T. Sasaki, and K. Shimizu. Mature bovine articular cartilage contains abundant aggrecan that is c-teminally truncated at Ala719-Ala720, a site which is readily cleaved by m-caplain. *Biochemical Journal*, 382:253–259, 2004.

[120] S. Park, K. D. Costa, and G. A. Ateshian. Microscale frictional response of bovine articular cartilage from atomic force microscopy. *Journal of Biomechanics*, 37(11):1679–1687, 2004.

[121] K. H. Parker, C. P. Winlove, and A. Maroudas. The theoretical distributions and diffusivities of small ions in chondroitin sulphate and hyaluronate. *Biophysical Chemistry*, 32:271–282, 1988.

[122] A. H. K. Plaas, S. Wong-Palms, P. J. Roughley, R. J. Midura, and V. C. Hascall. Chemical and immunological assay of the nonreducing terminal residues

of chondroitin sulfate from human aggrecan. *Journal of Biological Chemistry*, 272(33):20603–20610, 1997.

[123] O. Popescu, I. Checiu, P. Gherghel, Z. Simon, and G. N. Misevic. Quantitative and qualitative approach of glycan-glycan interactions in marine sponges. *Biochimie*, 85(1-2):181–188, 2003.

[124] O. Popescu and G. N. Misevic. Self-recognition by proteoglycans. *Nature*, 386:231–232, 1997.

[125] M. A. Pratta, W. Yao, C. Decicco, M. D. Tortorella, R.-Q. Liu, R. A. Copeland, R. Magolda, R. C. Newton, J. M. Trzaskos, and E. C. Arner. Aggrecan protects cartilage collagen from proteolytic cleavage. *Journal of Biological Chemistry*, 278(46):45539–45545, 2003.

[126] U. Raviv, S. Giasson, N. Kampf, J. F. Gohy, R. Jerome, and J. Klein. Lubrication by charged polymers. *Nature*, 425(6954):163–165, 2003.

[127] J. Rojo, J. C. Morales, and S. Penades. Carbohydrate-carbohydrate interactions in biological and model systems. *Topics in Current Chemistry*, 218:45–92, 2002.

[128] M. Ruths. Boundary friction of aromatic self-assembled monolayers: comparison of systems with one or both sliding surfaces covered with a thiol monolayer. *Langmuir*, 19(17):6788–6795, 2003.

[129] M. Ruths, N. Alcantar, and J. Israelachvili. Friction of aromatic monolayers: comparison between measurements with AFM and SFA. *Abstracts of Papers of the American Chemical Society*, 225:U616–U616, 2003.

[130] M. Ruths, N. A. Alcantar, and J. N. Israelachvili. Boundary friction of aromatic silane self-assembled monolayers measured with the surface forces apparatus and friction force microscopy. *Journal of Physical Chemistry B*, 107(40):11149–11157, 2003.

[131] S. Saleque, N. Ruiz, and K. Drickamer. Expression and characterization of a carbohydrate-binding fragment of rat aggrecan. *Glycobiology*, 3(2):185–190, 1993.

[132] J. D. Sandy and C. Verscharen. Analysis of aggrecan in human knee cartilage and synovial fluid indicates that aggrecanase (ADAMTS) activity is responsible for the catabolic turnover and loss of whole aggrecan whereas other protease activity is required for C-terminal processing in vivo. *Biochemical Journal*, 358(3):615–626, 2001.

[133] F. O. Schmitt, J. Gross, and J. H. Highberger. Tropocollagen and the properties of fibrous collagen. *Experimental Cell Research (Supplymentary)*, 3:326–334, 1955.

[134] H. Schonherr, M. W. J. Beulen, J. Bugler, J. Huskens, F. van Veggel, D. N. Reinhoudt, and G. J. Vancso. Individual supramolecular host-guest interactions studied by dynamic single molecule force spectroscopy. *Journal of the American Chemical Society*, 122(20):4963–4967, 2000.

[135] J. E. Scott. Supramolecular organization of extracellular matrix glycosaminoglycans, in vitro and in the tissues. *FASEB Journal*, 6:2639–2645, 1992.

[136] J. Seog, D. Dean, A. H. K. Plaas, S. Wong-Palms, A. J. Grodzinsky, and C. Ortiz. Direct measurement of glycosaminoglycan intermolecular interactions via high-resolution force spectroscopy. *Macromolecules*, 35(14):5601–5615, 2002.

[137] J. Seog, D. Dean, B. Rolauffs, T. Wu, J. Genzer, A. H. K. Plaas, A. J. Grodzinsky, and C. Ortiz. Nanomechanics of opposing glycosaminoglycan macromolecules. *Journal of Biomechanics*, 38(9):1789–1797, 2005.

[138] L. A. Setton, W. B. Zhu, and V. C. Mow. The biphasic poroviscoelastic behavior of articular cartilage: role of the surface zone in governing the compressive behavior. *Journal of Biomechanics*, 26(4-5):581–592, 1993.

[139] D. E. T. Shepherd and B. B. Seedhom. A technique for measuring the compressive modulus of articular cartilage under physiological loading rates with preliminary results. *Proceedings of the Institution of Mechanical Engineers*, 211:155–165, 1997.

[140] D. Spillmann and M. M. Burger. In B. Ernst, G. W. Hart, and P. Sinay, editors, *Carbohydrates in Chemistry and Biology*, volume 2, Chap 38, pages 1061–1091. Wiley-VCH, Weinheim, 2000.

[141] J. Stiernstedt, M. W. Rutland, and P. Attard. A novel technique for the in situ calibration and measurement of friction with the atomic force microscope. *Review of Scientific Instruments*, 76(8):083710, 2005.

[142] J. Stiernstedt, M. W. Rutland, and P. Attard. Erratum: A novel technique for the in situ calibration and measurement of friction with the atomic force microscope (vol 76, pg 083710, 2005). *Review of Scientific Instruments*, 77(1):019901, 2006.

[143] M. Stolz, R. Raiteri, A. U. Daniels, M. R. VanLandingham, W. Baschong, and U. Aebi. Dynamic elastic modulus of porcine articular cartilage determined at two different levels of tissue organization by indentation-type atomic force microscopy. *Biophysical Journal*, 86(5):3269–3283, 2004.

[144] S. Sundararajan and B. Bhushan. Topography-induced contributions to friction forces measured using an atomic force/friction force microscope. *Journal of Applied Physics*, 88(8):4825–4831, 2000.

[145] M. W. Swanepoel, J. E. Smeathers, and L. M. Adams. The stiffness of human apophyseal articular cartilage as an indicator of joint loading. *Proceedings of the Institution of Mechanical Engineers Part H-Journal of Engineering in Medicine*, 208:33–43, 1994.

[146] M. B. E. Sweet, E. J.-M. A. Thonar, and J. Marsh. Age-related changes in proteoglycan structure. *Archives of Biochemistry and Biophysics*, 198(2):439–448, 1979.

[147] R. Tadmor, N. H. Chen, and J. Israelachvili. Normal and shear forces between mica and model membrane surfaces with adsorbed hyaluronan. *Macromolecules*, 36(25):9519–9526, 2003.

[148] H. Takano, J. R. Kenseth, S. S. Wong, J. C. O'Brien, and M. D. Porter. Chemical and biochemical analysis using scanning force microscopy. *Chemical Reviews*, 99(10):2845–2890, 1999.

[149] G. A. Tomlinson. The molecular theory of friction. *Philosophical Magazine*, 7:905–916, 1929.

[150] V. V. Tsukruk and V. N. Bliznyuk. Adhesive and friction forces between chemically modified silicon and silicon nitride surfaces. *Langmuir*, 14(2):446–455, 1998.

[151] V. V. Tsukruk, V. N. Bliznyuk, J. Hazel, D. Visser, and M. P. Everson. Organic molecular films under shear forces: fluid and solid langmuir monolayers. *Langmuir*, 12(20):4840–4849, 1996.

[152] J. P. G. Urban, A. Maroudas, M. T. Bayliss, and D. J. Swelling pressures of proteoglycans at the concentrations found in cartilaginous tissues. *Biorheology*, 16:447–464, 1979.

[153] W. B. van den Berg. Lessons from animal models of osteoarthritis. *Current Opinion in Rheumatology*, 13:452–456, 2001.

[154] E. W. van der Vegte and G. Hadziioannou. Acid-base properties and the chemical imaging of surface-bound functional groups studied with scanning force microscopy. *Journal of Physical Chemistry B*, 101(46):9563–9569, 1997.

[155] E. W. van der Vegte and G. Hadziioannou. Scanning force microscopy with chemical specificity: an extensive study of chemically specific tip-surface interactions and the chemical imaging of surface functional groups. *Langmuir*, 13(16):4357–4368, 1997.

[156] E. W. van der Vegte. *Chemical and Physical Surface Properties Studied with Scanning Force Microscopy.* Ph.D. thesis, University of Groningen, The Netherlands, 1997.

[157] M. Varenberg, I. Etsion, and G. Halperin. An improved wedge calibration method for lateral force in atomic force microscopy. *Review of Scientific Instruments*, 74(7):3362–3367, 2003.

[158] M. Venturoni, T. Gutsmann, G. E. Fantner, J. H. Kindt, and P. K. Hansma. Investigations into the polymorphism of rat tail tendon fibrils using atomic force microscopy. *Biochemical and Biophysical Research Communications*, 303(2):508–513, 2003.

[159] D. V. Vezenov, A. Noy, L. F. Rozsnyai, and C. M. Lieber. Force titrations and ionization state sensitive imaging of functional groups in aqueous solutions by chemical force microscopy. *Journal of the American Chemical Society*, 119(8):2006–2015, 1997.

[160] S. S. Voyutskii. *Autoadhesion and Adhesion of High Polymers.* Wiley Interscience, New York, 1963.

[161] F. Wassermann. The intercellular components of connective tissue: origin, structure and interrelationship of fibers and ground substance. *Ergebnisse der Anatomie und Entwicklungsgeschichte*, 35. Band:241–333, 1956.

[162] T. N. Wight, D. K. Heinegard, and V. C. Hascall. Proteoglycans: structure and function. In E. D. Hey, editor, *Cell biology of the extracellular matrix.*, pages 45–78. Plenum Press, New York, 1991.

[163] J. L. Wilbur, A. Kumar, E. Kim, and G. M. Whitesides. Microfabrication by microcontact printing of self-assembled monolayers. *Advanced Materials*, 6(7-8):600–604, 1994.

[164] O. H. Willemsen, M. M. E. Snel, A. Cambi, J. Greve, B. G. D. Grooth, and C. G. Figdor. Biomolecular interactions measured by atomic force microscopy. *Biophysical Journal*, 79:3267–3281, 2000.

[165] A. Williamson, A. Chen, and R. Sah. Compressive properties and function-composition relationships of developing bovine articular cartilage. *Journal of Orthopaedic Research*, 19:1113–1121., 2001.

[166] L. Xu, C. M. Flahiff, B. A. Waldman, D. Wu, B. R. Olsen, L. A. Setton, and Y. Li. Osteoarthritis-like changes and decreased mechanical function of articular cartilage in the joints of mice with the chondrodysplasia gene (cho). *Arthritis and Rheumatism*, 48(9):2509–2518, 2003.

[167] M.-L. Yeh, X. Liu, and Z.-P. Luo. Quantification of the binding strength of type I collagen and decorin using optical tweezers. In *51st Annual Meeting of the Orthopaedic Research Society*, page 922, Washington, DC, 2005.

[168] S. Zapotoczny, T. Auletta, M. R. de Jong, H. Schonherr, J. Huskens, F. van Veggel, D. N. Reinhoudt, and G. J. Vancso. Chain length and concentration

dependence of beta-cyclodextrin ferrocene host guest complex rupture forces probed by dynamic force spectroscopy. *Langmuir*, 18(18):6988–6994, 2002.

[169] W. B. Zhu, V. C. Mow, T. J. Koob, and D. R. Eyre. Viscoelastic shear properties of articular cartilage and the effects of glycosidase treatments. *Journal of Orthopaedic Research*, 11(6):771–781, 1993.

[170] Y. X. Zhu and S. Granick. Biolubrication: hyaluronic acid and the influence on its interfacial viscosity of an antiinflammatory drug. *Macromolecules*, 36(4):973–976, 2003.

[171] S. Zou, H. Schonherr, and G. J. Vancso. Force spectroscopy of quadruple H-bonded dimers by AFM: dynamic bond rupture and molecular time-temperature superposition. *Journal of the American Chemical Society*, 127(32):11230–11231, 2005.